UNIVERSITY OF CALIFORNIA
SANTA CRUZ

COSMOLOGICAL STUDIES THROUGH LARGE-SCALE DISTRIBUTED ANALYSIS OF CHANDRA OBSERVATIONS

A dissertation submitted in partial satisfaction of the
requirements for the degree of

DOCTOR OF PHILOSOPHY

in

PHYSICS

by

Devon Hollowood

December 2018

The Dissertation of Devon Hollowood
is approved:

Tesla Jeltema, Chair

Constance Rockosi

Anthony Aguirre

Lori Kletzer
Vice Provost and Dean of Graduate Studies

Table of Contents

List of Figures

List of Tables

Abstract

Cosmological Studies Through Large-Scale Distributed Analysis of Chandra Observations

by

Devon Hollowood

The formation history of galaxy clusters is a powerful probe of cosmology. In particular, one may place strong constraints on the dark energy equation of state by examining the evolution across redshift of the number density of galaxy clusters as a function of mass. In this thesis, I describe my contributions to cluster cosmology, in particular to the development of the richness optical observable mass proxy.

I introduce *redMaPPer*, an optical cluster finder which represents an important upstream input for my thesis work. I next introduce the **M**ass **A**nalysis **T**ool for **Cha**ndra (***MATCha***), a pipeline which uses a parallelized algorithm to analyze archival Chandra data. *MATCha* simultaneously calculates X-ray temperatures and luminosities and performs centering measurements for hundreds of potential galaxy clusters using archival X-ray exposures. I run *MATCha* on the *redMaPPer* SDSS DR8 cluster catalog and use *MATCha*'s output X-ray temperatures and luminosities to analyze the galaxy cluster temperature-richness, luminosity-richness, luminosity-temperature, and temperature-luminosity scaling relations. I investigate the distribution of offsets between the X-ray center and *redMaPPer* center within $0.1 < z < 0.35$ and explore some of the causes of *redMaPPer* miscentering. I collaborate with members of the Dark Energy Survey in order to repeat this analysis on Dark Energy Survey Year 1 data. I outline the various ways in which *MATCha* constitutes an important upstream work for a variety of astrophysical

applications. These include the calibrations of two separate mass proxies, the study of the AGN fraction of galaxy clusters, and cosmology from cluster number densities and stacked weak lensing masses. Finally, I outline future upgrades and applications for *MATCha* throughout the lifespan of the Dark Energy Survey and the Large Synoptic Survey Telescope.

This dissertation is dedicated to my parents Lawrence and Dena Hollowood, to my brother Derek Hollowood, to my girlfriend Melanie Guevara, and to everyone who still feels amazed every time they look at the stars.

Acknowledgments

I would like to begin by thanking my wonderful advisor, Professor Tesla Jeltema, for her guidance and support throughout my graduate work at the University of California, Santa Cruz. She has managed to keep me on track for six years, she has always helped me to relax when I have becomes overwhelmed, and she has given me wonderful opportunities to present my research and go observing in fun places. I will always appreciate her fierce loyalty to her students, her extensive expertise in astronomy, and her excellent taste in music, fantasy literature, and Batman films.

Next I would like to thank my committee members Constance Rockosi and Anthony Aguirre for their comments on this work and for the many interesting conversations I have had with them about astronomy and general relativity.

I would like to thank my friends and family, and in particular my parents Lawrence and Dena Hollowood, my brother Derek Hollowood, and my girlfriend Melanie Guevara. They have been so, so supportive and were it not for their love and I would never have completed graduate school.

Finally, I would like to thank Verve Coffee Roasters ("the coffee office") for giving me a space to work and the fuel necessary to complete this thesis.

This dissertation incorporates work from Hollowood et al. (2018), particularly in chapter 3 and chapter 4. The co-authors listed in this publication participated in, directed, and supervised the research which forms the basis for these chapters. Hollowood et al. (2018) has been submitted for publication in the Astrophysical Journal Supplement Series.

Chapter 1

Introduction

1.1 Galaxy Cluster Cosmology

The current cosmological standard model suggests that the universe formed "from the bottom-up": first the stars, then the galaxies, and then most recently clusters of galaxies. Galaxy clusters, as the most recent objects to become gravitationally bound, are quite sensitive to the forces shaping the evolution of the universe. The observable properties of clusters are thus naturally a powerful tool in the cosmologist's toolbox. Clusters are independent from other cosmological probes such as type 1A supernovae, **B**aryon **A**coustic **O**scillation (**BAO**), and the **C**osmic **M**icrowave **B**ackground (**CMB**), and thus work in concert with these observables to eliminate degeneracies and give a more precise understanding of cosmology (see Figure 1.1). Upcoming and in-progress optical imaging surveys, such as the Dark Energy Survey (DES) (The Dark Energy Survey Collaboration, 2005), the Hyper Suprime Cam (HSC) (Miyazaki et al., 2012), Euclid (Laureijs et al., 2011), and the Large Synoptic Survey Telescope (LSST) (LSST Dark Energy Science Collaboration, 2012), are expected to observe of tens of thousands of galaxy clusters, dramatically expanding our ability to use clusters for cosmol-

ogy (Cunha et al., 2009; Sánchez and DES Collaboration, 2010; Oguri and Takada, 2011; Weinberg et al., 2013; Sartoris et al., 2016).

Galaxy clusters have been used as cosmological probes since the discovery of dark matter in Zwicky (1937). Since then they have been used to study the universe's matter density distribution (e.g. Bahcall and Soneira, 1983; Allen et al., 2003) and dark energy (Komatsu et al., 2011). A more in-depth history of cluster cosmology may be found in Voit (2005) and Allen et al. (2011).

One particularly interesting application of clusters is in studying the accelerating expansion of the universe. The acceleration of this expansion was first discovered in 1998 by Riess et al. (1998) and Perlmutter et al. (1999), and represented "one of the most important developments in modern cosmology" (Frieman et al., 2008). The cause of this acceleration is not well understood. One possibility is that it may be due to a breakdown of our understanding of gravity at large scales. The class of theories covering this possibility is known as "modified gravity" (Clifton et al., 2012). Alternatively, instead of modifying our theories of gravity, one may instead modify the energy content of the universe by adding a component dubbed "dark energy" which resembles a cosmological constant (Huterer and Shafer, 2018). For an overview of the continuum of modified gravity and dark energy theories, see Joyce et al. (2016).

For any given cosmological component, the ratio of the pressure p to the density ρ is called the equation of state (traditionally written as w). The evolution of the component is governed by the equation

$$\rho\left(z\right) = \rho_0 \exp\left(3\int_0^z \frac{1+w\left(z'\right)}{1+z'}\mathrm{d}z\right) \tag{1.1}$$

where z is the redshift of a certain point in the universe's history and ρ_0 is the present-day density of the component (Huterer and Shafer, 2018). The equation

Figure 1.1: Probes of Dark Energy

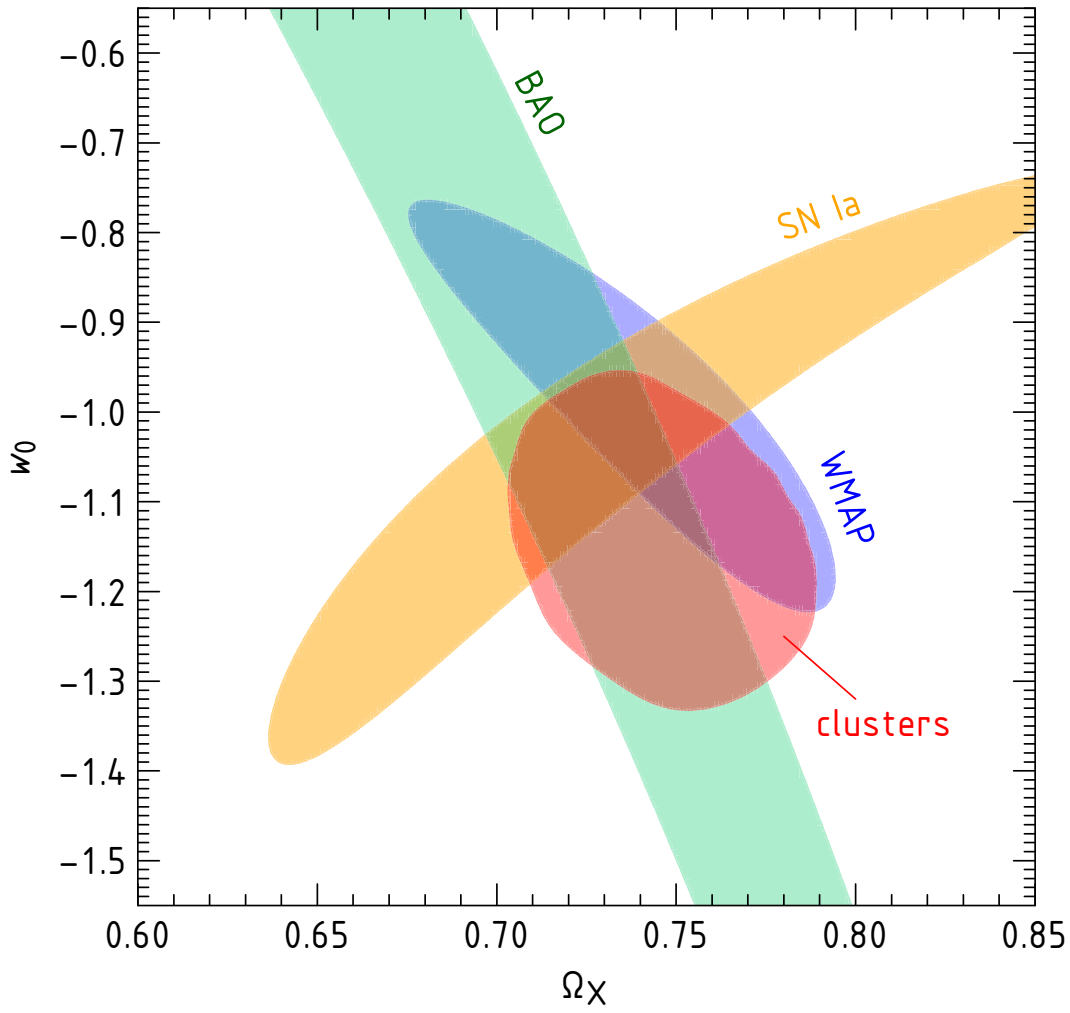

Contributions of various probes to constraining the present-day dark energy equation of state and energy density. Type 1A supernovae (SN 1A, yellow-orange): these provide "standardizable" candles which allow for the simultaneous measurement of redshift and luminosity distance. Baryon acoustic oscillation (BAO, mint green): these measurements constrain dark energy by looking for shifts in the power spectrum of matter density fluctuations. Cosmic Microwave Background (WMAP, lavender blue): the physical scale of peaks in the CMB spectrum is almost entirely unaffected by dark energy, however the angular scale is partially set by the distance to the surface of last scattering and thus by dark energy. The angular scale of CMB peaks is known to great precision, thus giving a strong angular-diameter distance constraint on dark energy. Clusters (pale red): The time it takes clusters to gravitationally collapse allow for constraints on dark energy density, with higher dark energy densities being associated with longer cluster formation timescales. The set of independent cosmological probes complement each other, and help to break each other's degeneracies. Plot taken from Vikhlinin et al. (2009).

Figure 1.2: Planck 2015 Constraints on Dark Energy

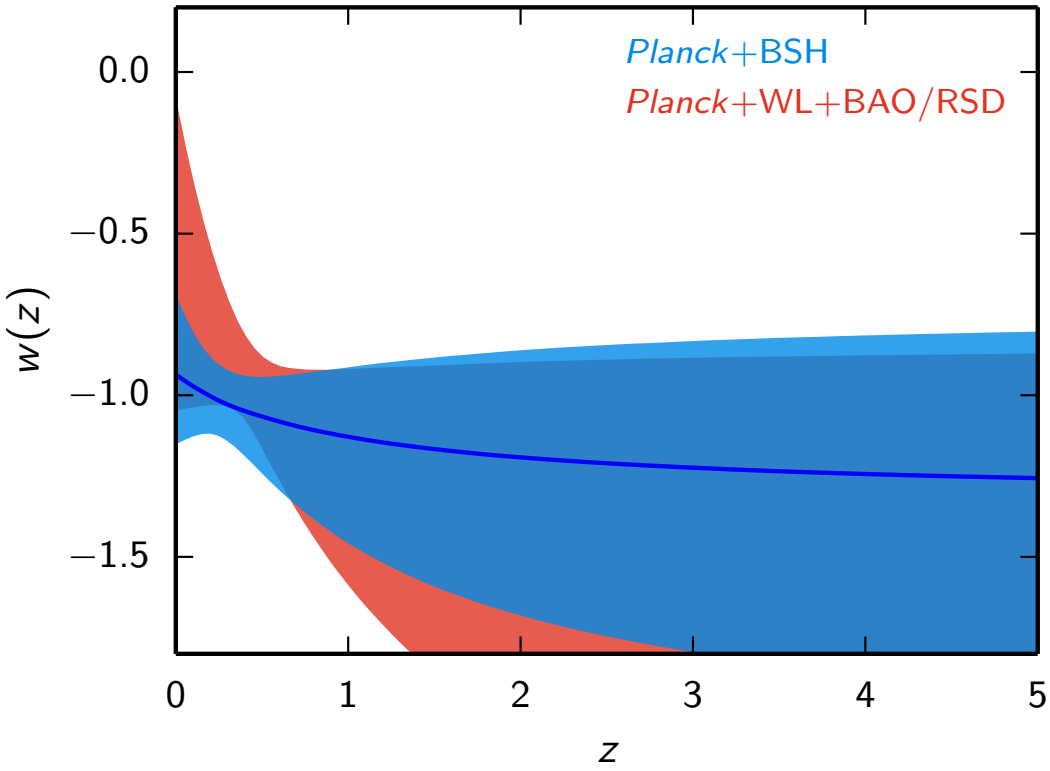

Current constraints on the dark energy equation of state, given by the Plank 2015 analysis (Planck Collaboration et al., 2016). $w\,(z)$ is consistent with a constant $w = -1$. Plot taken from Huterer and Shafer (2018).

of state is constant in time for radiation ($w = \frac{1}{3}$) and matter ($w = 0$), but in general it may evolve with time. In the case of dark energy, this evolution is often linearized as $w\,(a) = w_0 + w_a\,(1 - a)$, where w_0 is the present dark energy equation of state, and w_a is a parameter modeling the evolution of this density with the universe's scale factor $a \equiv \frac{1}{1+z}$ (Huterer and Shafer, 2018). Were dark energy a true cosmological constant, w_0 would be -1 and w_a would be zero. Our current best measurement of w_0 and w_a, from Planck Collaboration et al. (2018), are -0.961 ± 0.077 and $0.28^{+0.31}_{-0.27}$ respectively. A plot of the constraints on $w(z)$ from the Planck 2015 analysis may be seen in Figure 1.2.

Galaxy cluster formation gives strong constraints on $w(z)$. For example, a higher dark energy density in the past would cause the space between galaxies to expand more rapidly, making it more difficult for galaxy clusters to form. In an environment in which cluster formation is more difficult, galaxy clusters must start forming sooner in order to reach their present density. This leads to a key testable prediction of any given cosmology theory: the number density distribution of galaxy cluster masses as a function of redshift. In order to measure this distribution, one must measure galaxy cluster mass, and thus of prime interest are cluster observables which correlate with mass. Any given cluster observable-mass relation will have some intrinsic scatter distribution driven by recent dynamical activity as well as the full assembly history of each specific halo. Thus, in order to turn a measured distribution of observables into a distribution of masses, one must understand both the mean observable-mass relation and the intrinsic scatter distribution of this relation. Below, we discuss a number of cluster mass observables in both optical and X-ray and their intrinsic scatter distributions with mass.

1.2 Optical Cluster Observables

The primary emission from galaxy clusters in optical wavelengths comes from the stars in the constituent galaxies of the cluster (Bahcall, 1977). This allows one to see the individual galaxies in the cluster, and leads directly to a handful of simple mass proxies.

With sufficient spectroscopic information on member galaxies, one may measure the mass of a cluster through galaxy dynamics, either through virial relations (Smith, 1936) or caustic techniques (i.e. measuring the cluster escape velocity) (Diaferio and Geller, 1997).

In the absence of spectroscopic information, cluster masses may still be estimated, in particular if multi-band photometry is available. Cluster galaxies primarily lie on the red sequence (Bell et al., 2004). This sequence contains galaxies which are "red and dead", meaning that they have largely ceased star formation and consist primarily of ancient stars. It is possible to take advantage of this fact in order to estimate cluster redshift from color information alone (Rykoff et al., 2014).

One class of red-sequence-based optical mass observables is called *richness*. A cluster's richness is an estimate of the number of red-sequence galaxies in the cluster. Examples of richness measures include Koester et al. (2007)'s N_{200} (the number of red-sequence galaxies within r_{200}[1]) and Rozo et al. (2009)'s λ (a count of red-sequence galaxies which is weighted by cluster membership probability; see chapter 2).

A similar proxy is μ_*, an estimate of the stellar mass of the galaxy cluster (Palmese et al., in prep.). μ_* is discussed at length in section 6.2, along with my contributions to its development. Both richness and μ_* have higher intrinsic scatter with mass than X-ray temperature (see section 1.3). Other optical mass proxies include the total luminosity of all cluster galaxies and the luminosity of the central galaxy (Hansen et al., 2009; Zhang et al., 2016).

Finally, there is another, clever way of measuring the mass of a galaxy cluster using optical data. Instead of looking at the galaxy cluster itself, one may look at the distortion of galaxies behind the galaxy cluster due to weak gravitational lensing. Unlike the other methods listed here for measuring cluster masses, lensing alone allows one to directly probe the mass of the galaxy cluster without any need for a proxy observable. In wide-field cosmology surveys, it is impractical to obtain the depth of lensing data needed to directly measure the masses of individual

[1] r_{200} is the radius within which the halo density is 200 times the critical density.

galaxy clusters. However, by "stacking" observations of similar galaxy clusters it is possible to obtain their average mass (e.g. Leauthaud et al., 2010; von der Linden et al., 2014; Simet et al., 2017; Melchior et al., 2017; McClintock et al., 2018). Note that in stacked weak lensing it is of vital importance to stack upon the centers of galaxy clusters: off-center stacking will cause the mass profile to become "smeared out". Thus the ability to correctly center galaxy clusters is a leading systematic in stacked weak lensing efforts (Johnston et al., 2007; Melchior et al., 2017).

1.3 X-ray Cluster Observables

In X-ray, the primary emission from galaxy clusters comes from the **I**ntra**C**luster **M**edium (**ICM**) (Allen et al., 2011; Böhringer and Werner, 2010). The ICM is a galaxy-cluster-spanning plasma consisting primarily of ionized hydrogen and helium. These particles gain significant kinetic energy as they fall into the galaxy cluster's gravity well, causing them to emit in X-ray as a blackbody with a temperature of 10^7–10^8 K. (These energies are traditionally quoted as roughly 1 to 10 keV, using Boltzmann's constant as a conversion.) When present, **A**ctive **G**alactic **N**uclei (**AGN**) are also visible in X-ray. AGN are regions at the centers of galaxies which emit twin jets of relativistic particles as part of the process of accretion by the central supermassive black hole, however the precise mechanisms involved are not well understood (Romero et al., 2017). The accretion disk emits in X-ray both thermally and through lower-energy photons being scattered into X-ray via inverse Compton scattering in the accretion disk corona (Padovani et al., 2017). When pointed towards Earth, AGN jets are visible in X-ray as well. Unlike optical telescopes, current-generation X-ray telescopes typically cannot resolve individual cluster galaxies except at the lowest redshifts unless these galaxies have AGN

present.

The ICM provides many convenient X-ray mass proxies. The simplest is its luminosity, which primarily comes from bremsstrahlung, recombination, and chemical line emission (Allen et al., 2011). The total luminosity goes as the square of the electron density, and thus roughly as the square of the ICM mass density. This is particularly useful because the ICM comprises the majority of the baryonic mass of the cluster. That said, a given total cluster luminosity corresponds to a large spread in total cluster masses. Looking at luminosity as a function of radius and "deprojecting" the results gives a reasonable estimate of the gas mass, which is a lower-scatter mass proxy. Unfortunately, for low-exposure-time observations or high-redshift clusters this detailed spatial study often proves infeasible.

A third mass proxy is is the ICM's temperature, which is proportional to the collision rate of ICM particles (Böhringer and Werner, 2010). This too is somewhat spatially dependent, with large, relaxed clusters often having cool cores. Optimally, one would "crop out" these cool cores, but for automated analyses this often proves untenable due to the difficulty of determining an accurate core region (especially for faint clusters).

Finally, simulations suggest the gold-standard lowest-scatter known X-ray mass proxy is the product of the temperature and the gas mass, called Y_X (Kravtsov et al., 2006). Y_X is proportional to the total thermal energy of the cluster, and in this respect is similar to the Sunyaev-Zeldovich integrated Compton parameter Y_{SZ}. In practice, Y_X has not been found to be lower-scatter than other X-ray observables (Mahdavi et al., 2013).

1.4 The *Chandra* Space Telescope

The Chandra X-Ray Observatory (hereafter ***Chandra***) is the X-ray part of NASA's "great observatories" (along with the Spitzer Space Telescope for infrared, the Hubble Space Telescope for the optical spectrum, and the Compton Gamma-Ray Observatory for gamma-rays). We here give a brief overview of its workings, following the in-depth description given in Weisskopf et al. (2000), and introduce the associated technical terminology.

When X-ray photons enter the *Chandra* detector, they first hit a ten-meter-long series of focusing mirrors called the High-Resolution Mirror Assembly (**HRMA**). These mirrors, coated in iridium for higher reflectivity, are designed so that X-ray photons hit them and are reflected at a shallow angle—too-steep an angle would lead to excess absorption.

After the HRMA focuses the incoming photons, the photons proceed to a pair of insertable gratings: the Low-Energy and High-Energy Transmission Gratings (**LETG** and **HETG** respectively). These dispersion gratings allow for spectroscopic observation of X-ray sources. For every observation in this thesis's input data, neither the LETG nor the HETG are in use, as we are interested in spatial information lost by spectroscopic dispersion. Thus for our purposes the photons just pass by these gratings.

At this point the photons finally arrive at *Chandra*'s primary science instrumentation. This consists of the High Resolution Camera (HRC) and the Advanced CCD Imaging Spectrometer (ACIS). Both the HRC and the ACIS contain imaging and spectroscopic detectors, labeled **I** and **S** respectively (so for example the ACIS imaging detector would be referred to as "ACIS-I"). For the purposes of this dissertation, we use only the ACIS detectors. We use both ACIS-I and ACIS-S—despite its name, the latter may be used for imaging as well as for spectroscopy.

Figure 1.3: *Chandra* ACIS CCD Layout

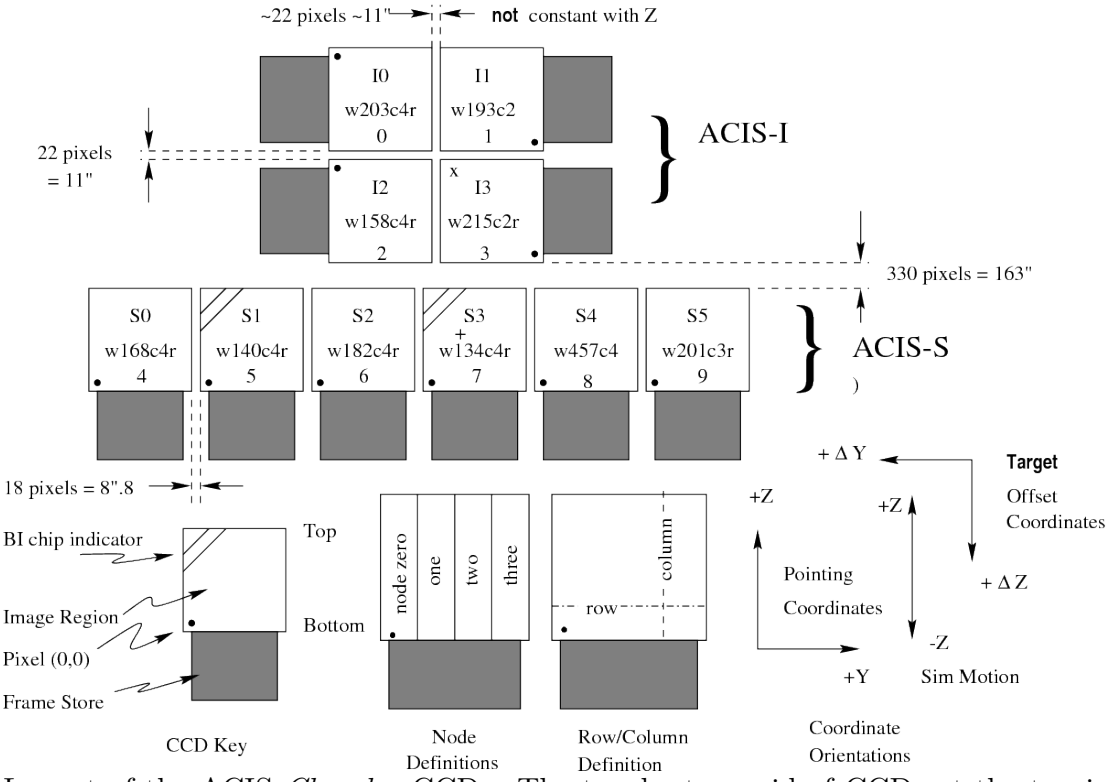

Layout of the ACIS *Chandra* CCDs. The two-by-two grid of CCDs at the top is ACIS-I, the six-by-one grid below is ACIS-S. I3 and S3 are aimpoint CCDs; S1 and S3 are back-illuminated. Image taken from Chandra X-ray Center (2017).

The ACIS-I detector consists of a two-by-two array of CCDs; the ACIS-S detector consists of a six-by-one array; see Figure 1.3 for a diagram of the layout of the ACIS detectors. Each CCD is 1024×1024 pixels, and each pixel has an angular size of $0.492'' \times 0.492''$. ACIS-I3 and ACIS-S3 are aimpoint CCDs and thus the observed object is usually found on these chips. ACIS-S1 and ACIS-S3 are back-illuminated, giving them better energy resolution and higher sensitivity to lower-energy photons than the other, front-illuminated CCDs. The effective areas for the two ACIS detectors and the HRC-I detector are shown in Figure 1.4. The photons activate these CCDs, which in turn output the timestamp, detection location, and channel (approximate energy) for each detected photon.

As with any telescope, there are limits to the spatial resolution of *Chandra* (Chandra X-ray Center, 2017). This is to say that the photons from a single point of emission (such as a star) will not all appear on the same pixel. The area over which photons from a point source are spread is known as the point-spread function (PSF). Near their focal points, the ACIS-I and ACIS-S detectors' limiting factor is the size of their pixels, and in this regime 90% of the energy from a point source will fall within 4 pixels of the center. Away from the these points, focal anomalies (i.e. the fact that the flat CCDs do not form a perfect focal surface) instead dominate the PSF. These anomalies are energy-dependent. The PSF of the four ACIS-I chips are plotted in Figure 1.5.

For spectral work, the energy resolution of *Chandra* CCDs may be important. In general it is quite good, with the front-illuminated detectors approaching their theoretical limits at launch, and the back-side detectors not far behind (Chandra X-ray Center, 2017). Since launch the energy resolution on front-illuminated CCDs has degraded in pixels far from the detector's frame storage; fortunately it is possible to correct for much of this effect. The energy resolution of the aimpoint

Figure 1.4: *Chandra* CCD Effective Areas

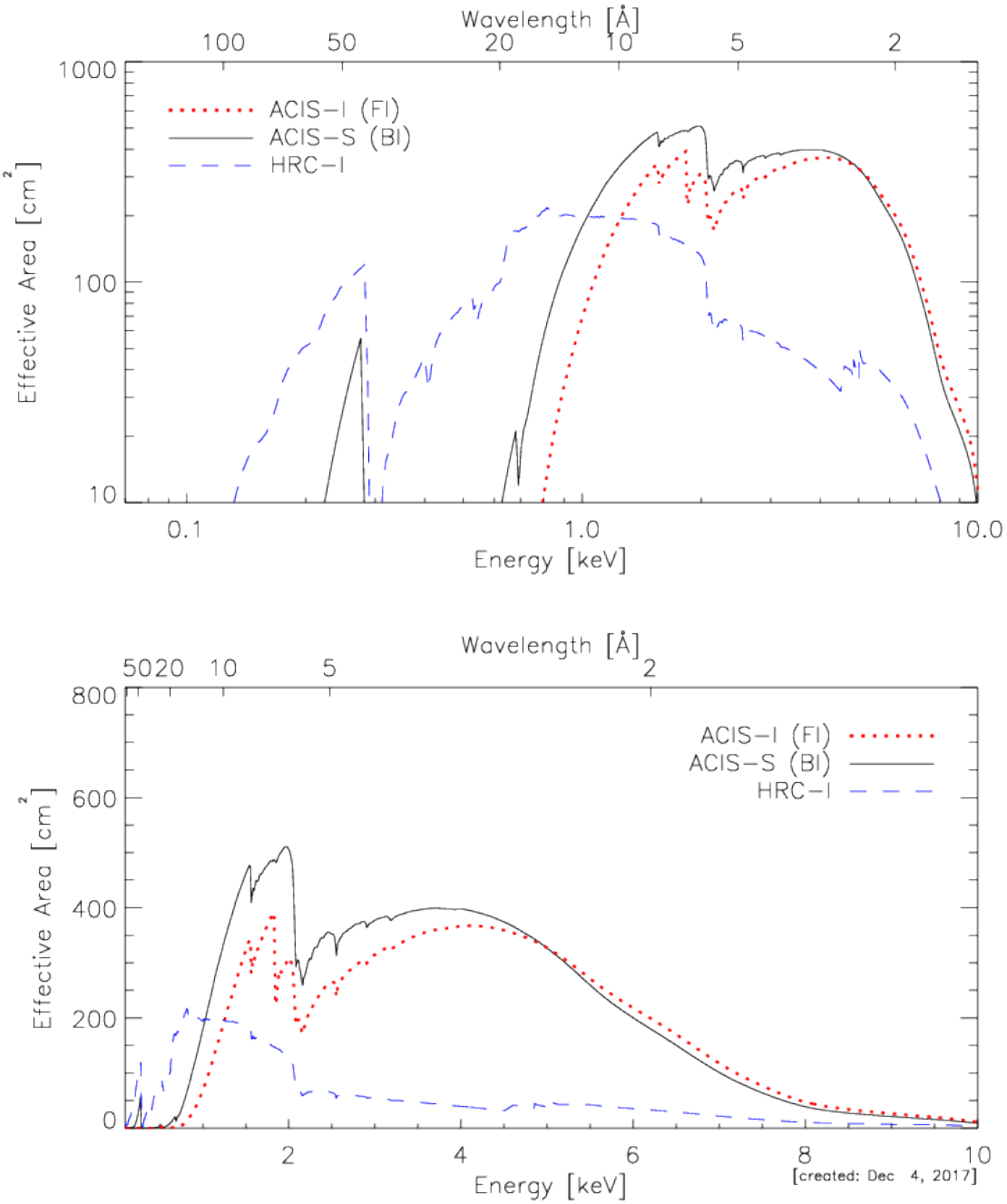

The wavelength-dependence of effective area for the ACIS-I, ACIS-S, and HRC-I *Chandra* detectors. Image taken from Chandra X-ray Center (2017).

Figure 1.5: *Chandra* ACIS-I Point-Spread Function

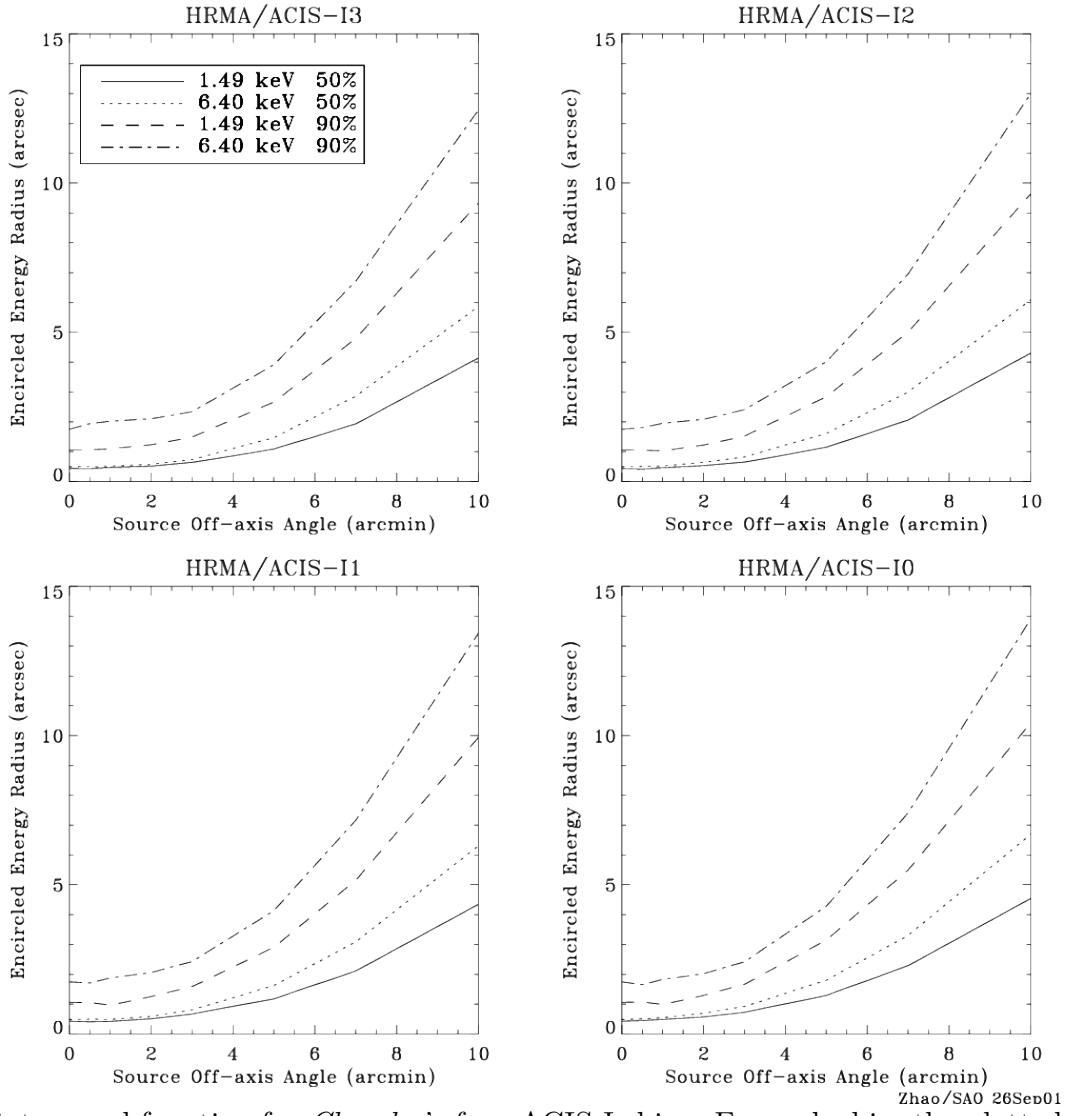

Point-spread function for *Chandra*'s four ACIS-I chips. For each chip, the plotted lines show the radius in which 50% and 90% of the energy is captured from a point source, as a function of offset from the focal point of the chip. Figure taken from Chandra X-ray Center (2017).

Figure 1.6: *Chandra* Aimpoint CCD Energy Resolution

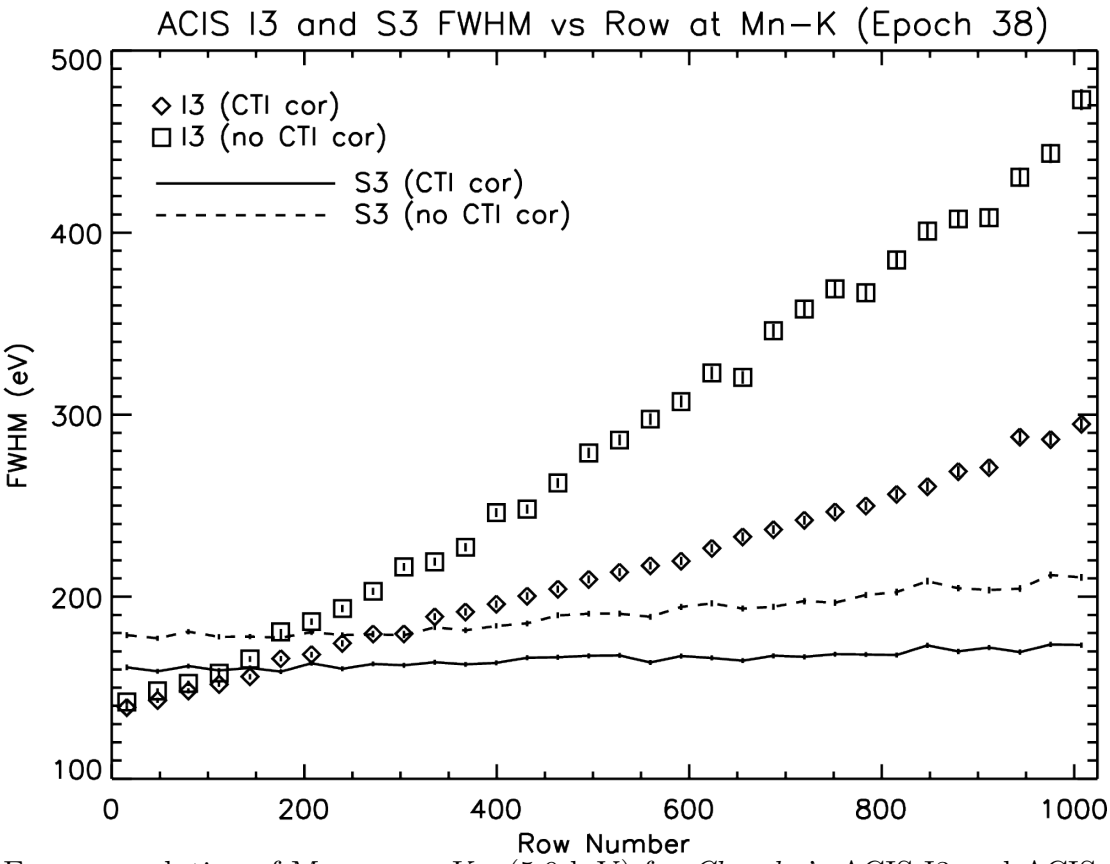

Energy resolution of Manganese Kα (5.9 keV) for *Chandra*'s ACIS-I3 and ACIS-S3 detectors. The spread in energy (vertical axis) is plotted as a function of pixel row number, for both detectors, and in both corrected and uncorrected forms. The correction greatly diminishes the effect of row number on energy resolution. Figure taken from Chandra X-ray Center (2017).

ACIS-I3 and ACIS-S3 detectors are plotted in Figure 1.6.

Every 8 hours, *Chandra* sends its data to the Deep Space Network at the Jet Propulsion Laboratory in Pasadena, California. From there the data are passed to The Chandra X-Ray Center at the Massachusetts Institute of Technology in Cambridge, Massachusetts for processing and archiving. Public observations are then released immediately; private observations are released to the public one year after they are taken.

1.5 Outline of this Dissertation

In this dissertation, I discuss my work in performing X-ray follow-up of optically-selected galaxy clusters in order to better understand richness as an optical mass proxy, thus providing essential calibration for cluster cosmology with surveys like DES and LSST.

In chapter 2, I give a brief overview of the **red**-sequence **Ma**tched-filter **P**robabilistic **Per**colation (***redMaPPer***) cluster finder. This cluster finder has been run on SDSS and DES data sets, and I use its output candidate clusters from these data sets as targets for my X-ray follow-up.

In chapter 3, I describe the **M**ass **A**nalysis **T**ool for **C**handra (***MATCha***) X-Ray analysis pipeline. This is a powerful pipeline which performs automated, parallel analysis of hundreds of galaxy clusters using archival *Chandra* data. To my knowledge it is the only pipeline of its class for use with *Chandra*.

In chapter 4, I use *MATCha* to analyze the Sloan Digital Sky Survey (**SDSS**) Data Release 8 (**DR8**) data set. I analyze the results to obtain a number of scaling relations involving temperature, luminosity, and richness. I additionally develop an understanding of *redMaPPer*'s centering ability and discuss implications for weak lensing efforts using *redMaPPer* data.

In chapter 5, I work with other DES members to repeat much of the section 4 analysis on the Dark Energy Survey (**DES**) Year 1 (**Y1**) data set. The DES data set is currently smaller than the SDSS data set, however it is expected to be much larger by the end of DES's six-year mission.

In chapter 6, I discuss additional applications of *MATCha*'s powerful abilities and its use as an upstream tool for important astrophysical research. These include the calibration *redMaPPer*, the calibration of the μ_* optical mass observable, the study of the AGN fraction in galaxy clusters, and the setting of centering

priors for stacked weak lensing and cluster cosmology.

Finally, chapter 7 provides a summary of the dissertation and a discussion of future upgrades to and use of *MATCha*.

Chapter 2

The *redMaPPer* Galaxy Cluster Finder

For cluster cosmology, optical imaging surveys such as DES, HSC, Euclid, and LSST are reliant on cluster finders to find overdensities of galaxies in their data and identify these overdensities as galaxy clusters. Additionally, cosmology-relevant parameters must be computed for these galaxy clusters. These cluster computations often include identifying a central galaxy, assigning a richness to the cluster, computing member galaxy redshifts, and computing member galaxy luminosities.

The work presented in this thesis is largely based on the validation and calibration of the **red**-sequence **Ma**tched-filter **P**robabilistic **Per**colation (***redMaPPer***) optical cluster finder. *redMaPPer* is introduced in Rykoff et al. (2014); its performance on SDSS data is qualified using X-ray and Sunyaev-Zeldovich effect (SZ) data in Rozo and Rykoff (2014); it is followed up with further SZ data in Rozo et al. (2015a); its ability to assign galaxies as cluster members is studied in depth in Rozo et al. (2015b); its use on DES Science verification data is described in Rykoff et al. (2016) and discussed in section 6.1. *redMaPPer* is an impor-

tant upstream component for the applications of the *MATCha* pipeline presented here; conversely we have used the *MATCha* pipeline to help validate and calibrate *redMaPPer* for use in other cosmological analyses. In this section, I give a brief outline of the algorithm behind *redMaPPer* and discuss its use in the research contained in this thesis.

The *redMaPPer* cluster finder is a two-stage iterative process. In the first stage, *redMaPPer* takes a series of galaxies with known spectroscopic redshifts and uses them as a seeds to find overdensities of galaxies of similar colors. These overdensities are then used to create a model for the colors of red-sequence galaxies as a function of redshift. The second stage applies this empirical red-sequence model to group galaxies into clusters, and assign a photometric redshift to the clusters. These data are then used to re-train the red-sequence. The process is iterated until convergence.

Once the red-sequence model is converged, *redMaPPer* uses this model to calculate the number of nearby red-sequence galaxies centered on every galaxy in the photometric catalog. Galaxies that show an excess of nearby galaxies are ranked according according to the likelihood of the potential cluster centered on that galaxy. The richness of the top-ranked cluster is measured, and the members probabilistically removed from the other candidate clusters. The algorithm then moves on to the next highest ranked candidate central galaxy, and the procedure is iterated. This process is called *percolation*. The *redMaPPer*-assigned richness (λ) is the sum of the membership probabilities of galaxies within a richness-scaling radius $R_\lambda = (1.0h^{-1}\mathrm{Mpc})\left(\frac{\lambda}{100.0}\right)^{0.2}$. This radius scaling is empirically determined to minimize scatter in the mass-richness relation (Rykoff et al., 2012). Richnesses are corrected for missing galaxy data via Monte Carlo sampling; this primarily effects high-redshift clusters ($z > 0.35$).

In the first generation of the catalog, central galaxies are selected as the brightest members. The statistical properties of these candidate centrals are then used to define a set of filters that can be used to recenter clusters in a probabilistic way. This procedure is iterated until convergence is achieved. The end result is a cluster catalog with central galaxies that are not simply the brightest cluster members, but also take into consideration the local galaxy density in the immediate neighborhood of the galaxy. The final catalog contains a list of galaxy clusters and associated data, including positions, redshifts, richnesses, membership probabilities, and top-five most-likely centers (and their centering probabilities). For a visualization of *redMaPPer*'s output for Abell 2219, see Figure 2.1.

redMaPPer is a powerful tool for cluster cosmology. Its richnesses are a observationally-cheap low-scatter optical cluster mass proxy and its cluster centers provide weak-lensing surveys a point on which to stack their observations for combined analysis. X-ray scaling relations with *redMaPPer* λ are discussed in section 4.1 for SDSS and in section 5.2 for DES Year 1. *redMaPPer* centering is discussed in section 4.5 for SDSS and in section 5.1 for DES Year 1. Additionally, *MATCha* is used for *redMaPPer* validation, and has uncovered bugs in the *redMaPPer* algorithm. These bugs include the accidental loss of bright galaxies in the initial *redMaPPer* DES Y1 catalog and the miscalculation of redshifts for bright galaxies caused by an updated photometry calculation algorithm. *MATCha*'s role in the validation of *redMaPPer* DES science verification data is discussed in section 6.1.

Figure 2.1: *redMaPPer* Analysis of Abell 2219

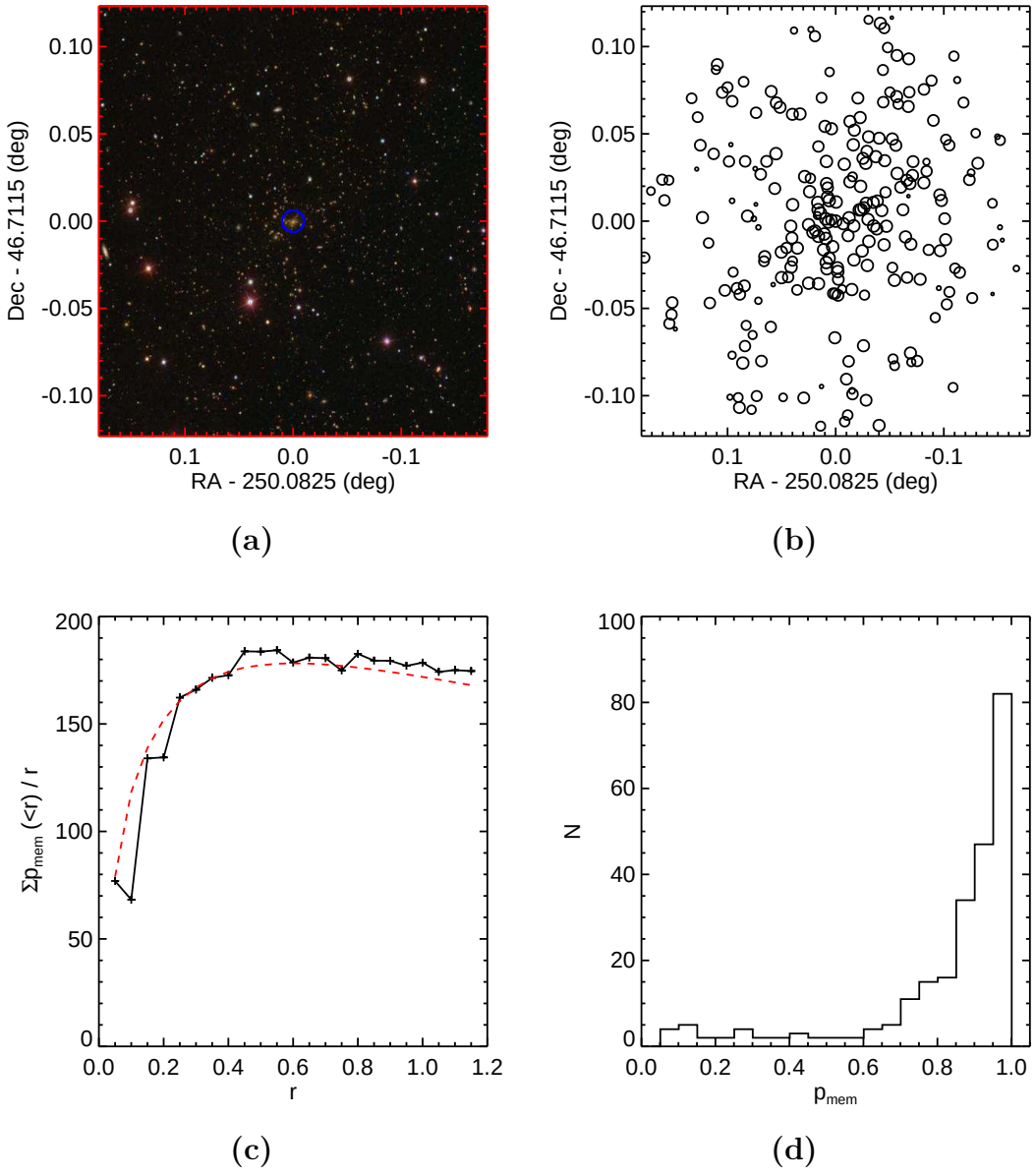

(a) Image of Abell 2219, taken from SDSS, *redMaPPer* central galaxy circled in blue. (b) *redMaPPer* members for Abell 2219, with circle size proportional to membership probability. (c) Membership distribution as a function of radius, with a corresponding Navarro-Frenk-White profile plotted in dashed red. (d) Distribution of membership probabilities for all galaxies assigned to Abell 2219. This combined figure is taken from Rykoff et al. (2014).

Chapter 3

The *MATCha* X-ray Analysis Pipeline

The intrinsic scatter distribution of the richness-mass relation is currently one of the largest sources of uncertainty in using cluster richness to place cosmological constraints (Wu et al., 2010). One may constrain this scatter distribution and improve these constraints by following up a subset of these optically-selected clusters to obtain mass proxies in other wavelengths. To this end, I have developed a pipeline to perform automated, massively parallelized X-ray follow-up on galaxy clusters which fall within archival *Chandra* data. This pipeline is called ***MATCha***: the **M**ass **A**nalysis **T**ool for **Cha**ndra. *MATCha* attempts to measure gas temperatures and X-ray luminosities for these clusters, which can then be compared with their richnesses to help better understand the intrinsic scatter distribution of the richness-mass relation.

MATCha takes a series of (right ascension, declination, redshift) coordinates (hereafter RA, Dec, and z respectively) from a galaxy cluster catalog and returns a list of cluster centroids, peaks, temperatures and luminosities (hereby referred to as T_X and L_X respectively) by running a series of CIAO version 4.7 (CALDB

version 4.6.7) (Fruscione et al., 2006) and HEASOFT version 6.17 tools. All spectral fitting is performed using *XSPEC* version 12.9.0 (Arnaud, 1996). A visual representation of the output for a typical, relaxed cluster may be seen in Figure 3.1. For visual representations of more complex cases, see section 3.8.

Figure 3.1: *MATCha* Analysis of a Relaxed Cluster

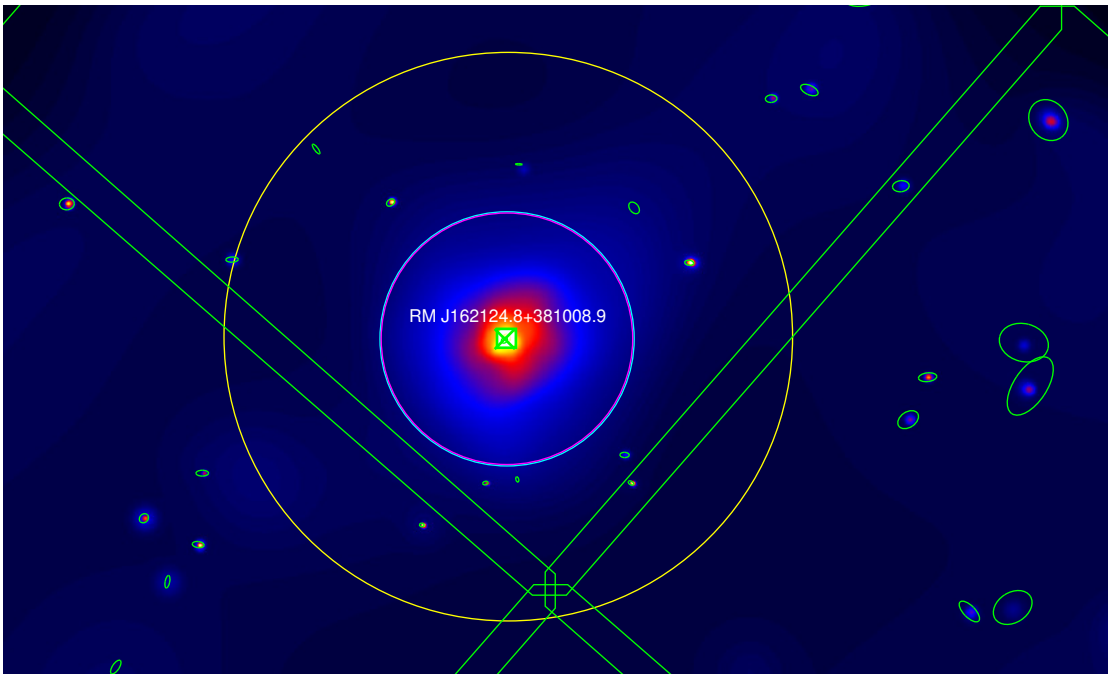

RM J162124.8+381008.9 (mem_match_id 2573, $z = 0.48$), ObsID 10785, ACIS-I detector. This is a typical example of the output of *MATCha* for a relaxed cluster. In each galaxy cluster image in this thesis, small white circles represent *redMaPPer* clusters, with the white text above this circle giving the name of the cluster. The green square marks the center of the *redMaPPer* cluster under consideration by *MATCha* for the analysis presented in the image. (One image may contain multiple *redMaPPer* clusters, but these clusters are analyzed separately and we only present the information for one cluster at a time.) The green X marks the X-ray peak (see section 3.5). The cyan circle marks a 500 kpc aperture centered on the final location of the iterated 500 kpc centroid. The purple circle marks a r_{2500} aperture centered at the cluster's r_{2500} centroid. The yellow circle marks a r_{500} aperture centered at the cluster's r_{500} centroid. Green ellipses mark X-ray point sources. Finally, the large green polygons in each image mark the boundaries of the *Chandra* CCDs. Each image has been smoothed, and has the point sources left in.

3.1 Data Preparation

In the data preparation phase, *MATCha* starts with a list of sky coordinates and redshifts for *redMaPPer* clusters. It then uses the *find_chandra_obsid* CIAO tool to query the *Chandra* archive for the relevant sky coordinates, determining which of these clusters lie within one or more *Chandra* observations. *MATCha* then downloads these relevant observations and re-reduces them using the *chandra_repro* CIAO tool.

MATCha then cleans the observations, as follows. First, *MATCha* cuts the energy range to 0.3–7.9 keV and removes flares from each observation with the *deflare* CIAO tool (set to use the *lc_clean* algorithm, and using a lightcurve time interval of 259.28 seconds). Next, *MATCha* produces images and exposure maps for the observation. *MATCha* then identifies point sources using the *wavdetect* CIAO tool and removes these from the observation. In this process, the ACIS-I chips are cleaned together, separate from the ACIS-S chips. The ACIS-S chips are cleaned individually, separate from the ACIS-I chips and from the other ACIS-S chips. We choose to clean ACIS-S chips individually because of their significantly differing instrumental responses, e.g. the ACIS S1 and S3 CCDs are back-illuminated whereas the other CCDs are front-illuminated.

At this point *MATCha* is ready to start the analysis of individual clusters, determining whether they are are detected in X-ray, attempting to fit a T_X and L_X for detected clusters, and attempting to fit an upper-limit L_X for undetected clusters. A few visual examples of the output of *MATCha* are given in section 3.8.

3.2 Finding T_X and L_X

After the observations are downloaded and cleaned, *MATCha*'s next step is to find X-ray centroids, temperatures, and luminosities within r_{2500}, and r_{500} regions. A key strength of *MATCha* is the parallel nature of this computation, allowing for fully concurrent analysis of galaxy clusters. Care is taken to ensure that cluster may be analyzed soon as all of its observations are cleaned, and that each observation is downloaded and cleaned only once even when multiple clusters lie within it. In this section we enumerate the steps involved in the analysis of a single cluster; this algorithm is additionally presented as a flowchart in Figure 3.2. Note that r_{2500} is defined as the radius around a halo at which the average density is 2500 times the cosmological critical density; r_{500} is the radius at which the average density is 500 times the critical density. *MATCha* uses the temperature-radius relation from Arnaud et al. (2005) to calculate these radii when they are needed[1]. All centroids are calculated using the *dmstat* CIAO tool. *MATCha* additionally determines T_X and L_X values for a core-excised r_{500} aperture, the calculation of which is presented in this section. However due to the noisy nature of these data for faint clusters, we choose not to present scaling relations for the core-excised r_{500} aperture in chapter 4, instead leaving this analysis as a possibility for a later work.

The main steps in the *MATCha* cluster analysis are as follows:

1. *MATCha* iteratively centers a region with a 500 kpc radius, using the *redMaP-*

[1]These calculations are only meant as an approximation to the r_δ radius. Arnaud et al. (2005) uses core-cropped temperatures and uses *XMM* instead of *Chandra*, introducing a systematic bias in the input of this $T_X - r_\delta$ relation of a few keV (Nevalainen et al., 2010; Schellenberger et al., 2015). However, in the Arnaud et al. (2005) relation, moderate changes in input temperature have little effect on the resulting radii. Conversely, when we fit our temperatures we find that moderate changes in source radius do not greatly affect the resulting temperature. Thus we do not expect our choice of $T_X - r_\delta$ relation to be a dominant systematic in our calculated luminosities or temperatures.

Figure 3.2: The *MATCha* Analysis Process

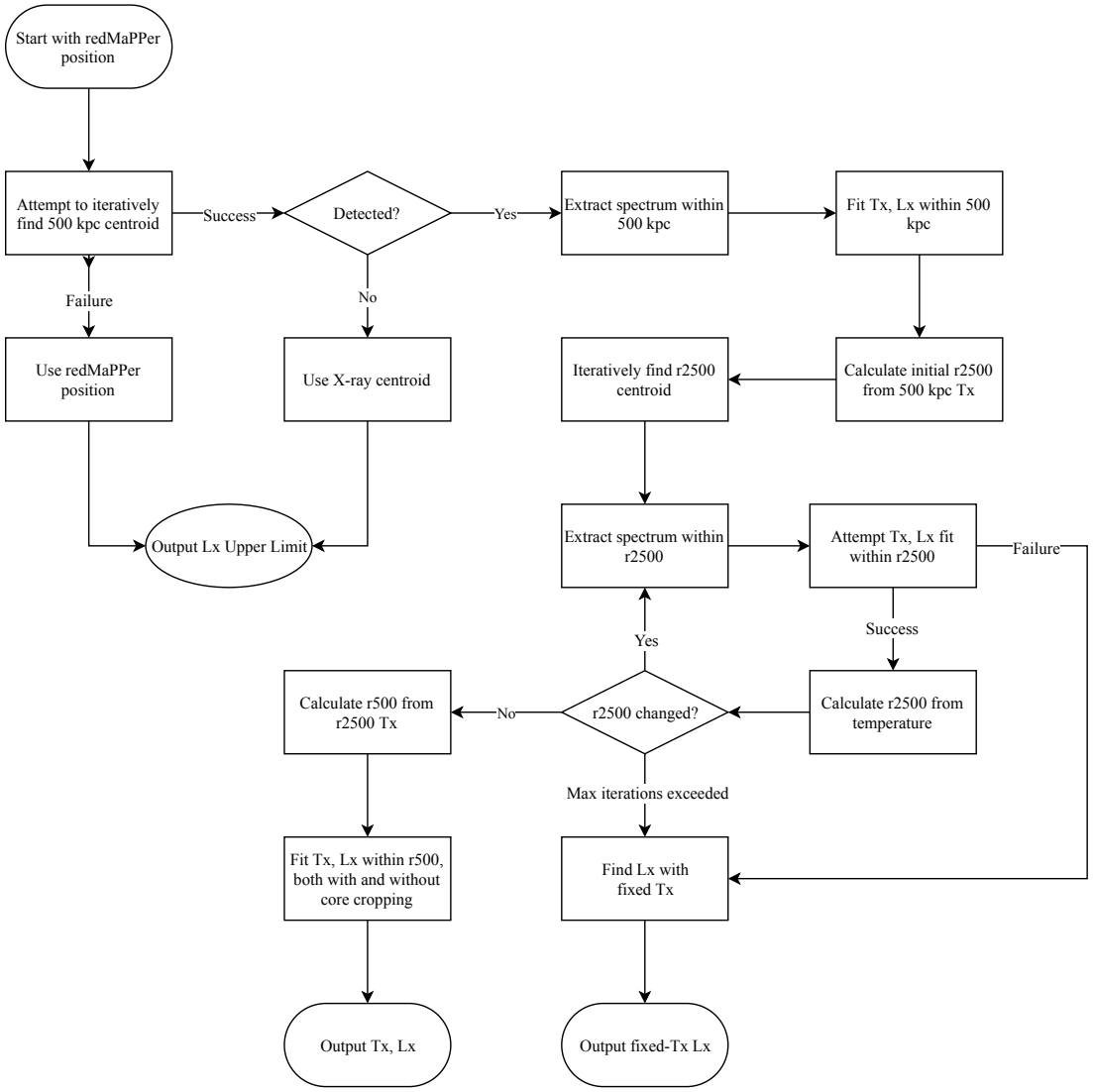

Per position as the initial center. The corresponding angular separation for this 500 kpc radius is calculated by dividing 500 kpc by the angular diameter distance to the cluster (given the *redMaPPer* redshift). In each iteration, the new center is the X-ray centroid within the previous 500 kpc region. Iteration stops when the new center is within 15 kpc of the old center; the new center is chosen. This iterative nature of this process allows us to find centroids which lie more than 500 kpc from the *redMaPPer* cluster position, so long as there is sufficient cluster emission within 500 kpc to point *MATCha* towards the centroid. If no stable center has been found after 20 iterations, *MATCha* aborts the attempt to find a center and marks the cluster as "undetected". *MATCha* then attempts to fit an L_X upper limit to this "undetected" cluster using the position from *redMaPPer* and the calculated 500 kpc radius. See section 3.4.

2. *MATCha* checks to see if the signal-to-noise ratio for the source region over the background region is greater than 5.0. If so, the cluster is considered "detected", and *MATCha* continues the attempt to find T_X and L_X. If not, *MATCha* marks the cluster "undetected", and aborts the attempt to find T_X and L_X. In the latter case, *MATCha* attempts to assign the cluster an L_X upper limit using the converged position from step 1 and the calculated 500 kpc radius. See section 3.4. For this target 500 kpc region, the background is taken as an annulus spanning 700 to 1000 kpc.

3. *MATCha* extracts a background-subtracted spectrum within the target region, centered on the converged centroid.

4. *MATCha* fits a temperature to this spectrum, and calculates the unabsorbed luminosity in the soft-band (0.5–2.0 keV) as well as a bolometric (0.001–

100 keV) luminosity. This fit is performed using *XSPEC*, and assumes a galactic absorption hydrogen column density found using the *nH* HEASOFT tool (this is a weighted average of the hydrogen densities found in Kalberla et al. (2005) and Dickey and Lockman (1990)). The metal abundance is fixed to $0.3Z_{\odot}$, using the model from Anders and Grevesse (1989). We find that the choice to fix the metal abundance is unimportant for clusters with $k_B T_X \gtrsim 3.0$ keV. For clusters with $k_B T_X \lesssim 3.0$ keV, we find that varying the abundance between $0.2Z_{\odot}$ and $0.4Z_{\odot}$ affects the fitted temperatures by $\approx 20\%$, which is usually less than our 1σ statistical uncertainties. The spectral model used is *XSPEC*'s wabs $*$ mekal model. Spectra are weighted by their aperture-correction factors (see section 3.3).

5. *MATCha* repeats step 1, with the initial position being the 500-kpc centroid, and the radius being the calculated r_{2500} radius. The converged position becomes our r_{2500} position. If this new centroid does not converge within 20 iterations, the attempt to fit L_X and T_X is aborted.

6. *MATCha* iteratively repeats steps 3-4 to find the temperature and luminosities for the r_{2500} region, stopping when the new r_{2500} temperature is within 1σ of the previous r_{2500} temperature. For our r_{2500} regions, the background is taken as an annulus spanning $1.5 \cdot r_{2500}$ to $3.37 \cdot r_{2500}$. (The latter number is approximately $1.5 \cdot r_{500}$, which is the outer limit of the r_{500} background discussed in step 7.)

7. *MATCha* repeats steps 1-4, using a region with the final r_{2500} position as the initial center and r_{500}, as estimated via the r_{2500} temperature, as its radius. This gives a centroid, L_X, and T_X for r_{500}. For this r_{500} region, the background is taken as an annulus spanning $1.05 \cdot r_{500}$ to $1.5 \cdot r_{500}$.

8. *MATCha* repeats steps 3-4, using an annular region with the calculated r_{500} as its outer radius, $0.15 \cdot r_{500}$ as its inner radius, and the r_{500} position (from step 7) as its center. This gives L_X and T_X for a "core cropped" r_{500} region. As with the non-core-cropped r_{500} region, the background is taken as an annulus spanning $1.05 \cdot r_{500}$ to $1.5 \cdot r_{500}$.

Note that in this section's description of the *MATCha* algorithm, all regions are taken as a Boolean AND with the *Chandra* field-of-view in order to avoid contaminating data with extraneous "zeros" from area outside the observation. Additional steps are taken to account for this when the area of a region is required for a calculation; these steps are described in full in the next section of this thesis (section 3.3).

For clusters with multiple observations, all fits described above are performed as a single simultaneous fit over all observations.

3.3 Aperture Correction

In many observations, the entirety of the detectable cluster emission does not lie on the chip. Furthermore point sources sometimes account for a significant portion of the cluster area, especially on non-aimpoint *Chandra* chips. It is thus necessary to correct for area "lost" to chip edges and point sources. To this end, we consider a series of equal-width annuli which cover the cluster source area. We aim to use ten annuli, but if this would result in annuli with widths of less than 10 pixels, we instead use the maximum number of annuli that allows each annulus a width of at least 10 pixels. For each annulus, we then take the photon count within the detector area (excluding areas marked as point sources), $N_{\mathrm{annulus,obs}}$, and multiply this count by the ratio of the "full" area of the annulus (i.e. $\pi(r_2^2 - r_1^2)$,

where r_2 is the outer annular radius and r_1 is the inner annular radius) to the exposed annular area A_{annulus}.

$$N_{\text{annulus,adj}} = N_{\text{annulus,obs}} \cdot \frac{\pi\,(r_2^2 - r_1^2)}{A_{\text{annulus}}} \tag{3.1}$$

The result, $N_{\text{annulus,adj}}$ approximates the number of counts that we would have received within the annulus were there no point sources or chip edges, assuming that the flux is relatively constant around the annulus. The sum of these adjusted counts is then compared with the total counts measured in the cluster source area (N_{tot}). This ratio gives an "adjust factor" F_{adj} for the missing area in each observation.

$$F_{\text{adj}} = \frac{\sum\limits_{\text{annuli}} N_{\text{annulus,adj}}}{N_{\text{tot}}} \tag{3.2}$$

We multiply our luminosities and upper limits by this factor. For clusters with multiple observations, we correct individually before calculation of T_X or L_X. We choose to perform this procedure because it maintains reasonable accuracy for faint clusters and because we do not want to make assumptions about the shape of the surface brightness profile.

3.4 L_X Without T_X

If *MATCha* cannot fit an r_{2500} T_X to a detected cluster, *MATCha* will still attempt to calculate the cluster's luminosity with an assumed temperature of 3.0 keV and r_{2500} of 500 kpc. As with the luminosities fitted alongside T_X, these luminosities are aperture-corrected. The main source of uncertainty in this L_X measurement is from the unknown T_X. Using an assumed T_X affects our calculated luminosity: a too-low T_X gives a too-high luminosity and a too-high T_X gives a

too-low luminosity. Additionally, assuming a 500 kpc radius (instead of using an r_{2500} radius given by a T_X-r_{2500} relation) means that we oversample lower-mass clusters and undersample higher-mass clusters. To estimate the contribution of this T_X uncertainty to our L_X uncertainty, we use PIMMS[2] to estimate the change in flux for a fixed count rate and a varying spectrum, and a β-model to estimate the change in flux between a 500 kiloparsec aperture and the temperature-determined r_{2500} aperture. We find that the effects of an uncertain T_X on the assumed flux and on the assumed radius partially cancel each other. At a temperature of 1 keV we underestimate L_X due to the temperature by a factor of ≈ 1.4 and overestimate L_X due to the radius by a factor of 0.4-0.8. At a temperature of 12 keV we overestimate L_X due to the temperature by a factor of ≈ 0.8 and underestimate L_X due to the radius by a factor of 1.0-1.3. The net effect is roughly negligible for high T_X, and for low T_X we slightly overestimate L_X. We believe that this error is significantly less than the statistical uncertainty in our scaling relations' fitted slope and scatter (see chapter 4). However, to compensate for the potential systematic uncertainty from using an assumed T_X and r_{2500}, we manually increase our error bars for these L_X values which come from an assumed T_X. The new error bars are taken to be $(0.5 \cdot L_X)$–$(2.0 \cdot L_X)$ plus the statistical errors. This factor of two was chosen as a conservative error estimate which encompasses the majority of potential L_X changes. We find that this choice has negligible effect on our derived scaling relations. In principle, this method may be improved by using an L_X-T_X relation to generate a new T_X, and then using the above process to generate a new L_X from this T_X, continuing to convergence. However, this is beyond the scope of this thesis, and such an extension is left as potential future work.

For "undetected" clusters, an L_X upper limit may be placed by assuming that

[2]https://heasarc.gsfc.nasa.gov/docs/software/tools/pimms.html

all emission received from the cluster location is background, and then calculating the flux that would be 3σ above this background. Here we consider emission from the area within 500 kpc of the X-ray centroid determined in step 1 of section 3.2. If no such position can be found, we use the *redMaPPer* position. We then predict a model flux by assuming a 3.0 keV temperature and using the same wabs $*$ mekal model as in section 3.2. An upper limit flux $\Phi_{\max,n_\sigma}$ is then given by

$$\Phi_{\max,n_\sigma} = \Phi_{\text{model}} \cdot \frac{n_\sigma \sqrt{N_{\text{obs}}}}{N_{\text{model}}} \tag{3.3}$$

where Φ_{model} is the fitted flux, n_σ is the desired confidence level (in units of standard deviation), N_{obs} is the aperture-corrected observed number of counts, and N_{model} is the product of the exposure time and the model count rate. These counts are not background subtracted, because by definition the source region for an undetected cluster is indistinguishable from background. Here, we multiply the observed flux from the non-detection by the ratio of (the count rate that we would have detected the cluster with confidence $n_\sigma\sigma$) to (the count rate that we observed). Typical values of N_{obs} for undetected clusters are a few hundred photons, with the middle 50% of undetected clusters having between 148 and 642 counts. Through this method, we place a 3σ L_X upper limit (within a 500 kpc aperture) on each "undetected" cluster.

3.5 Peak Finding

In addition to finding the X-ray centroid, which is a useful measure of a cluster's center for spectral fitting, we explore using a cluster's most luminous X-ray region as an alternative centering measure which is better matched to the *redMaPPer* central galaxy (see section 4.5). Simply taking the brightest pixel does not

work as a reliable cluster center; more care must be taken in determining the X-ray peak. This is both because observations can be quite noisy, and because we would like to avoid picking the peak of a small substructure of the galaxy cluster which happens to be X-ray bright over a more significant substructure which happens to be slightly dimmer. Additionally, we may have cut out the X-ray peak when we cut out X-ray point sources, as there is occasionally an active galactic nucleus in the most luminous region of a galaxy cluster. To deal with these problems, we smooth the binned X-ray image (with point sources removed) via convolution with a 2D Gaussian of 50 kpc radius. We then take the X-ray peak to be the brightest pixel of this smoothed image that is within 500 kpc of the X-ray's 500-kpc-aperture centroid (see section 3.2). As before, this 500 kpc radius is proper distance and is calculated using the *redMaPPer* redshift. We then check the results of the peak-finding visually (see section 3.6), looking for cases where the true cluster peak lies outside of our initial 500 kpc search. This occurs a only small handful of times, likely < 10. In these cases we manually re-run the above analysis with a larger peak search radius, chosen to include the actual peak.

3.6 Post-Pipeline Analysis and Cleaning

After running *MATCha* to get T_X and L_X (or L_X upper limits) for each cluster, we further examine the detected clusters to ensure a clean sample. First, we compare the output cluster catalog to the known galaxy clusters in the NASA/IPAC Extragalactic Database (NED)[3], to find any instances where our moving centroid (see section 3.2, step 1) causes the X-ray analysis to choose a bright, nearby X-ray cluster instead of a separate, foreground or background cluster detected by

[3]The NASA/IPAC Extragalactic Database (NED) is operated by the Jet Propulsion Laboratory, California Institute of Technology, under contract with the National Aeronautics and Space Administration

redMaPPer. We then manually examine each used observation, flagging both potential problems and interesting attributes.

"Potential problems" include clusters whose X-ray centroids are not located on a cluster substructure (see e.g. Figure 3.7 (a)), clusters which are too close to an outer chip edge to be considered reliable, clusters whose sole observation is in a non-imaging mode[4], clusters which are "mismatched" (as in our above NED search), and clusters whose background or source spectra are significantly contaminated by a separate nearby cluster. Additionally, for r_{500} regions we find a handful of clusters for which we cannot measure a reliable background because r_{500} is approximately the angular size of the observation(s); we flag these clusters as being too close to a chip edge and treat them as we treat our other clusters affected by proximity to chip edges.

"Interesting attributes" include merging or disturbed clusters, clusters where the *redMaPPer*-assigned center does not lie near an X-ray peak, and "serendipitous" clusters—clusters which are not the aimpoint of the *Chandra* observation and which are thus more free from selection bias (see section 4.4). Our criterion for marking a cluster as serendipitous is that in each of its observations the cluster either lies on a non-aimpoint *Chandra* chip, or shares the observation with a cluster which is clearly the aimpoint cluster. See Figure 3.7 in section 3.8 for examples of these common X-ray phenomena.

Because we only use undetected clusters as upper limits in our L_X-λ scaling relations, we do not examine them in as-great a depth. For these clusters, we only flag proximity to an outer chip edge and non-imaging-mode X-ray observations.

We then use these flags to make cuts to our scaling-relation and centering data sets. When fitting mass-proxy–richness relations and when comparing *redMaPPer* centers to X-ray peaks, we remove clusters for which proximity to the chip edge

[4]A *Chandra* image may be generated even if the observation is in a non-imaging mode.

is deemed an issue, clusters whose sole observation is in a non-imaging mode, and "mismatched" clusters. When comparing *redMaPPer* centers to X-ray centroids (but not peaks), we remove the above cases, and additionally remove clusters for which the X-ray centroid does not lie on a major X-ray substructure. This is because *redMaPPer* is not expected to produce a center that agrees with the X-ray centroid in these cases (see section 4.5 for discussion). Note that for each cluster we separately decide whether chip edge proximity is a problem for centering and whether it is a problem for each radius's L_X and T_X. For example, in RM J135933.6+621900.9 (mem_match_id 972, see Figure 3.3), we have an example of a cluster whose proximity to the chip edge is a problem for centering but not for scaling relations, because the proximity to the chip edge causes the centroid to move significantly yet we could capture enough of the cluster emission to determine T_X and L_X accurately.

Using this system of flagging, we are able to give *redMaPPer* centering feedback directly to the *redMaPPer* team. See section 4.5 for more information on our follow-up on *redMaPPer* centering.

3.7 Mispercolations

Sometimes, when there are two or more separate physical clusters near one another, or when *redMaPPer* has incorrectly split a single massive halo into two-or-more separate clusters in its catalog, *redMaPPer* assigns a large richness to the smaller system and a small richness to the larger system. We call this problem "mispercolation", as it is a failure of *redMaPPer*'s "percolation" step (see chapter 2). In our data, we correct these mispercolations by manually assigning the brightest halo's centroids, radii, T_X, and L_X values to the richest *redMaPPer* halo. We then remove the other *redMaPPer* cluster entirely. Effectively, this is

Figure 3.3: *MATCha* Analysis of Cluster Near CCD Edge

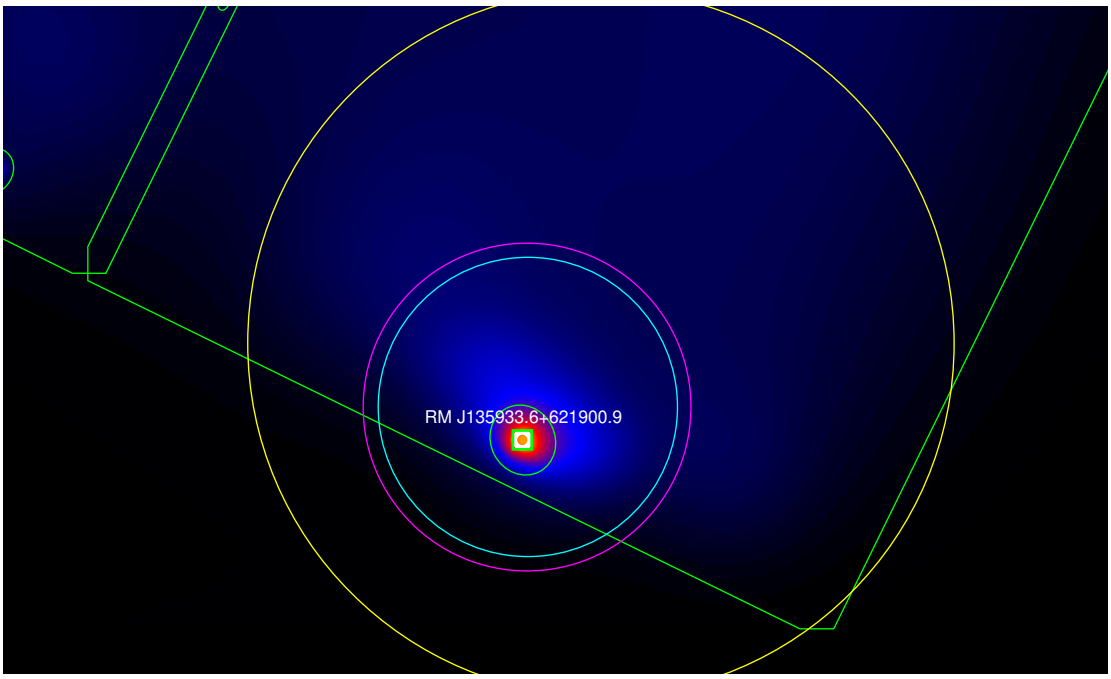

RM J135933.6+621900.9 (mem_match_id 972, $z = 0.34$), ObsID 7714, ACIS-I detector. This cluster is very close to the chip edge, and thus we cannot determine accurate centering information for it. However, we still capture enough cluster emission to get accurate L_X and T_X values. As with every *Chandra* image in this thesis, this image obeys the coloring conventions described in the caption for Figure 3.1.

Table 3.1: Summary of Mispercolation Handling

ID	λ	z	Action Taken
21	38.7	0.31	Remove from data.
23	128.7	0.29	Replace r_{2500} centroid, radius, L_X, and T_X with that of #21. Keep r_{500} data as-is.
34	166.2	0.30	Replace r_{2500} and r_{500} centroid, radius, L_X, and T_X with that of #41.
41	20.0	0.30	Remove from data.
25	73.4	0.17	Keep as-is.
24	26.5	0.17	Remove from data.
236	69.8	0.18	Replace r_{2500} and r_{500} centroid, radius, L_X, and T_X with that of #164.
164	22.7	0.16	Remove from data.

Here the "ID" column gives the mem_match_id from the *redMaPPer* catalog

equivalent to treating the two halos as a single halo with a very large centering error, which makes intuitive sense because mispercolation is a *redMaPPer* centering issue. Additionally, this approach acts as a compromise between removing mispercolated halos altogether, which artificially removes richness scatter and miscentering information, and keeping the halos untouched, which leads to extreme outliers in the scaling relations (because very hot or massive clusters are associated with low-richness entries in the *redMaPPer* catalog). For a full treatment of the effects of *redMaPPer* miscentering on scaling relations, see Zhang et al. (in prep.).

In the *redMaPPer* SDSS DR8 sample (described in chapter 4), we identify four cases of mispercolation. Images of each mispercolated cluster are presented in Figures 3.4–3.5 along with a brief discussion of how we handle each individual case. The cases are summarized in Table 3.1.

Figure 3.4: *MATCha* Analysis of Two Mispercolated Clusters

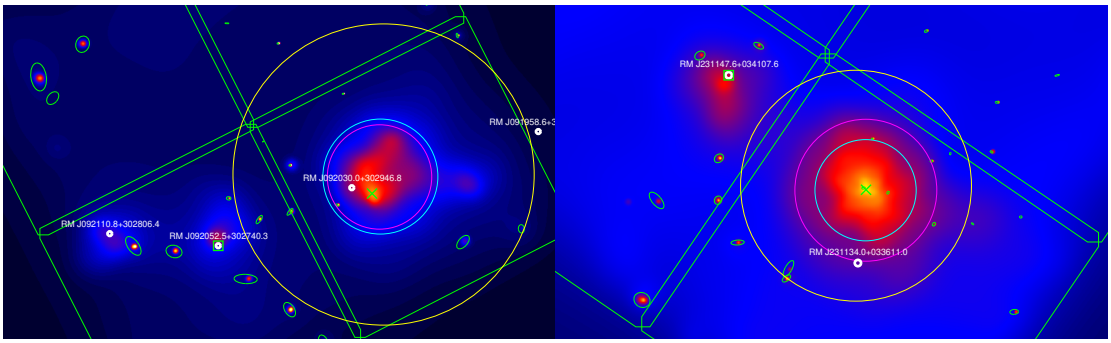

(a) **(b)**

(a) RM J092052.5+302740.3 (mem_match_id 23, $z = 0.29$) and RM J092030.0+302946.8 (mem_match_id 21, $z = 0.31$), ObsID 534, ACIS-I detector. Here, *redMaPPer* splits this merging cluster into two separate clusters. *redMaPPer* then assigns a richness of 129 to the smaller subcluster (left, RM J092052.5+302740.3) and a richness of 39 to the larger subcluster (right, RM J092030.0+302946.8). In our analysis, we discard the latter and take this to be a single cluster: RM J092052.5+302740.3. We then manually assign this cluster the X-ray peak, r_{2500} centroid, r_{2500} radius, r_{2500} T_X, and r_{2500} L_X from RM J092030.0+302946.8. We determine the r_{500} information to be acceptable without modification. This figure shows the final modified regions. (b) RM J231147.6+034107.6 (mem_match_id 34, $z = 0.30$) and RM J231134.0+033611.0 (mem_match_id 41, $z = 0.30$), ObsID 11730, ACIS-I detector. Here, *redMaPPer* splits this merging cluster into two separate clusters. *redMaPPer* assigns a richness of 166 to the smaller subcluster (left, RM J231147.6+034107.6) and a richness of 20 to the larger subcluster (right, RM J231134.0+033611.0). In our analysis, we discard the latter and take this to be a single cluster with the X-ray peak, r_{2500} centroid, r_{2500} radius, r_{2500} T_X, r_{2500} L_X, r_{500} centroid, r_{500} radius, r_{500} T_X, and r_{500} L_X from J231134.0+033611.0 (the less rich halo), but with the richness and *redMaPPer* ID from RM J231147.6+034107.6 (the richer halo). This figure shows the final modified regions. As with every *Chandra* image in this thesis, these images obey the coloring conventions described in the caption for Figure 3.1.

Figure 3.5: *MATCha* Analysis of Two More Mispercolated Clusters

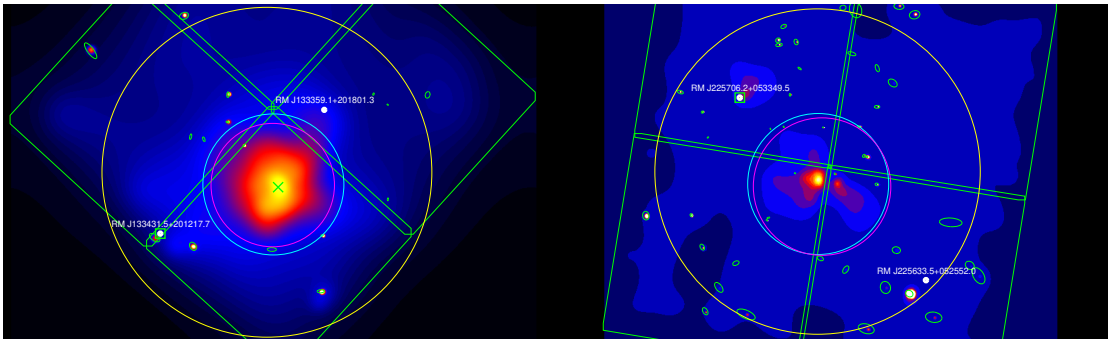

(a) **(b)**

(a) RM J133431.5+201217.7 (mem_match_id 25, $z = 0.17$) and RM J133359.1+201801.3 (mem_match_id 24, $z = 0.17$), ObsID 17159, ACIS-I detector. Here, *redMaPPer* splits this single, relaxed cluster into two separate clusters. *redMaPPer* divides the richness between the two clusters, assigning a richness of 73 to RM J133431.5+201217.7 (left) and a richness of 26 to RM J133359.1+201801.3 (right). In our analysis, we discard the latter and use the former as-is. This figure shows the regions for RM J133431.5+201217.7. (b) RM J225706.2+053349.5 (mem_match_id 236, $z = 0.18$) and RM J225633.5+052552.0 (mem_match_id 164, $z = 0.16$), ObsID 12248, ACIS-I detector. Here, *redMaPPer* splits this merging cluster into two separate clusters. *redMaPPer* assigns a richness of 70 to a fragment of the cluster (left, RM J225706.2+053349.5) and a richness of 23 to a second fragment (right, RM J225633.5+052552.0). Both of these are offset from the X-ray cluster. In our analysis, we discard the latter and take this to be a single cluster: RM J225706.2+053349.5. We then manually assign this cluster the X-ray peak, r_{2500} centroid, r_{2500} radius, r_{2500} T_X,r_{2500} L_X, r_{500} centroid, r_{500} radius, r_{500} T_X, and r_{500} L_X from RM J225633.5+052552.0. This figure shows the final modified regions. As with every *Chandra* image in this thesis, these images obey the coloring conventions described in the caption for Figure 3.1.

3.8 Example Images

Here we present sample images of *Chandra* observations produced by *MATCha* as described in chapter 3. Figure 3.6 demonstrates *MATCha* output for an asymmetric cluster, a cluster with substructure, and a low-redshift cluster. Figure 3.7 demonstrates various cases in which *MATCha* gives a result which is either incorrect or not useful. The correction for and accounting of these errors is discussed in section 3.6.

3.9 Flags and Data Cuts

Here we present the effects on our data of each individual flag which we use in section 3.6. In the interest of reproducibility we present these effects in the $0.1 < z < 0.35$ redshift range unless otherwise noted. This is the range which gives the most accurate *redMaPPer* results (see section 4.1) and is the same redshift range for which we release our data in Hollowood et al. (2018).

In the four subplots of Figure 3.8 we highlight, on an r_{2500} T_X-λ plot, (a) clusters outside the $0.1 < z < 0.35$ range, (b) clusters which are too close to chip edges, (c) mispercolated clusters, and (d) serendipitous clusters. As expected, the redshift restriction does not seem to preferentially bias the data. Additionally, the data show that proximity to an edge leads to under-estimating T_X and mispercolation leads to under-estimating richness. For a discussion of serendipitous clusters, see section 4.4.

Figure 3.6: *MATCha* Analysis of Asymmetric and Low-Redshift Clusters

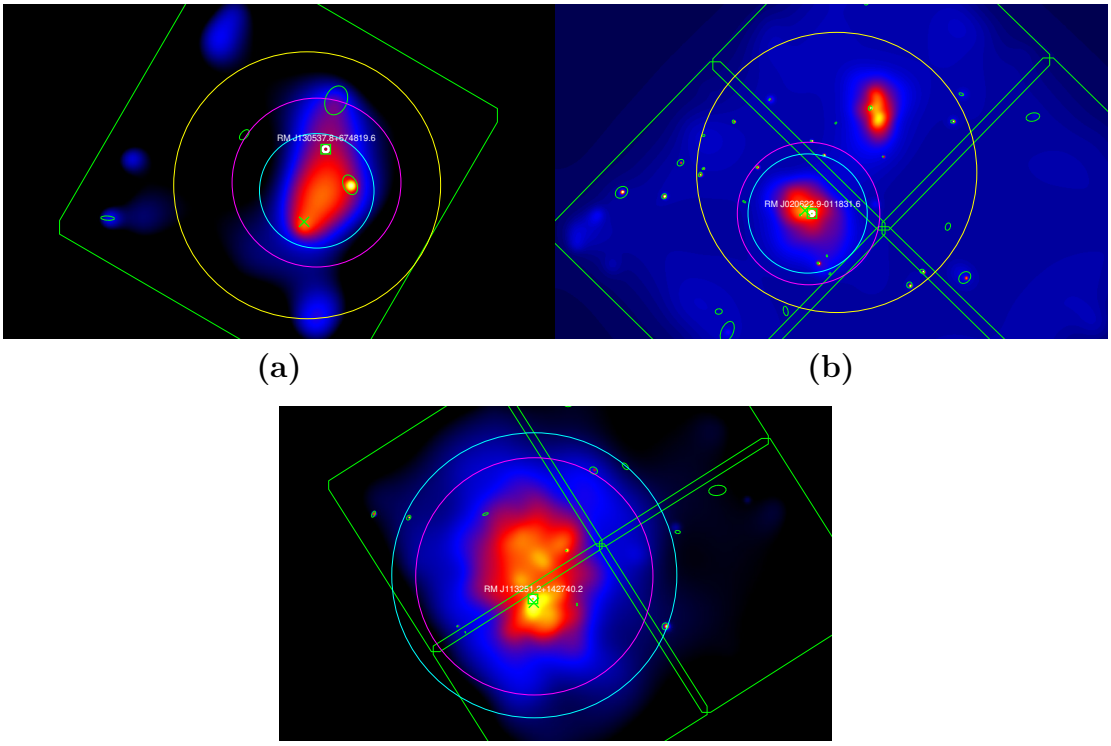

(a) **(b)**

(c)

(a) RM J130537.8+674819.6 (mem_match_id 2598, $z = 0.23$), ObsID 10868, ACIS-S2 chip. This is an example of the output of *MATCha* for an asymmetric, and is also an example of a serendipitous cluster. (b) RM J020622.9−011831.6 (mem_match_id 1382, $z = 0.19$), ObsID 16229, ACIS-I detector. This is an example of a cluster featuring substructure. In this case, *MATCha* analyzes the southern structure only until it reaches the r_{500} analysis, at which point it moves the centroid to a point between the two clusters. (c) RM J113251.2+142740.2 (mem_match_id 384, $z = 0.09$), ObsID 14387, ACIS-I detector. This is an example of a low-redshift cluster, which takes up much of the *Chandra* observation. r_{500} does not fit on the observation, and is thus not analyzed. *MATCha* automatically handles the fact that r_{2500} goes off the observation, see section 3.3. As with every *Chandra* image in this thesis, these images obey the coloring conventions described in the caption for Figure 3.1.

Figure 3.7: *MATCha* Analysis of Edge-Case Clusters

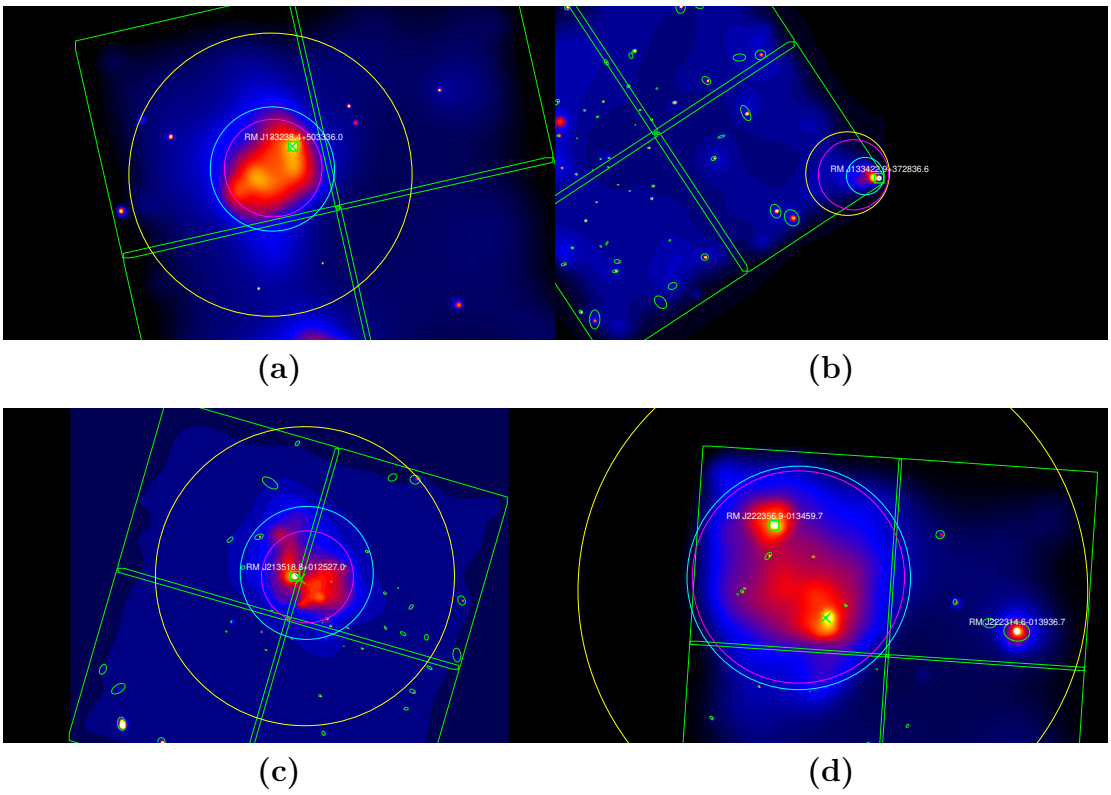

(a) RM J133238.4+503336.0 (mem_match_id 35, $z = 0.29$), ObsID 7710, ACIS-I detector. Because this cluster is disturbed, the X-ray centroid does not agree with the *redMaPPer* BCG, nor should it. For this reason, this cluster's centroid is removed from the centering checks on *redMaPPer* in section 4.5. However the peak is kept, and the cluster's L_X and T_X values are used in the scaling relations in chapter 4. (b) RM J133422.9+372836.6 (mem_match_id 1806, $z = 0.31$), ObsID 12307, ACIS-I detector. Here, *MATCha* successfully determines temperatures and luminosities for both r_{2500} and r_{500}, but these are suspect because the cluster is right in the corner of its only observation. Additionally, the centroid determination is adversely affected by the proximity to the chip edge. Thus, this cluster is removed from the data for both centering and scaling relations. (c) RM J213518.8+012527.0 (mem_match_id 155, $z = 0.23$), ObsID 15097, ACIS-I detector. Here, *MATCha* successfully determines a temperature for both r_{2500} and r_{500}, but unfortunately it has done so for the wrong cluster—this *redMaPPer* cluster at $z = 0.23$ is being masked by ABELL 2355 at $z = 0.12$. This cluster is removed from the data for both centering and scaling relations. (d) RM J222356.9−013459.7 (mem_match_id 48, $z = 0.10$), ObsID 15107, ACIS-I detector. Here, emission from RM J222314.6−013936.7 (mem_match_id 7113, $z = 0.30$, right) contaminates the background spectrum for RM J222356.9−013459.7 (left). For this reasons, RM J222356.9−013459.7 (left) is removed from the data for scaling relations. As with every *Chandra* image in this thesis, these images obey the coloring conventions described in the caption for Figure 3.1.

Figure 3.8: Flags and their Effect on Data

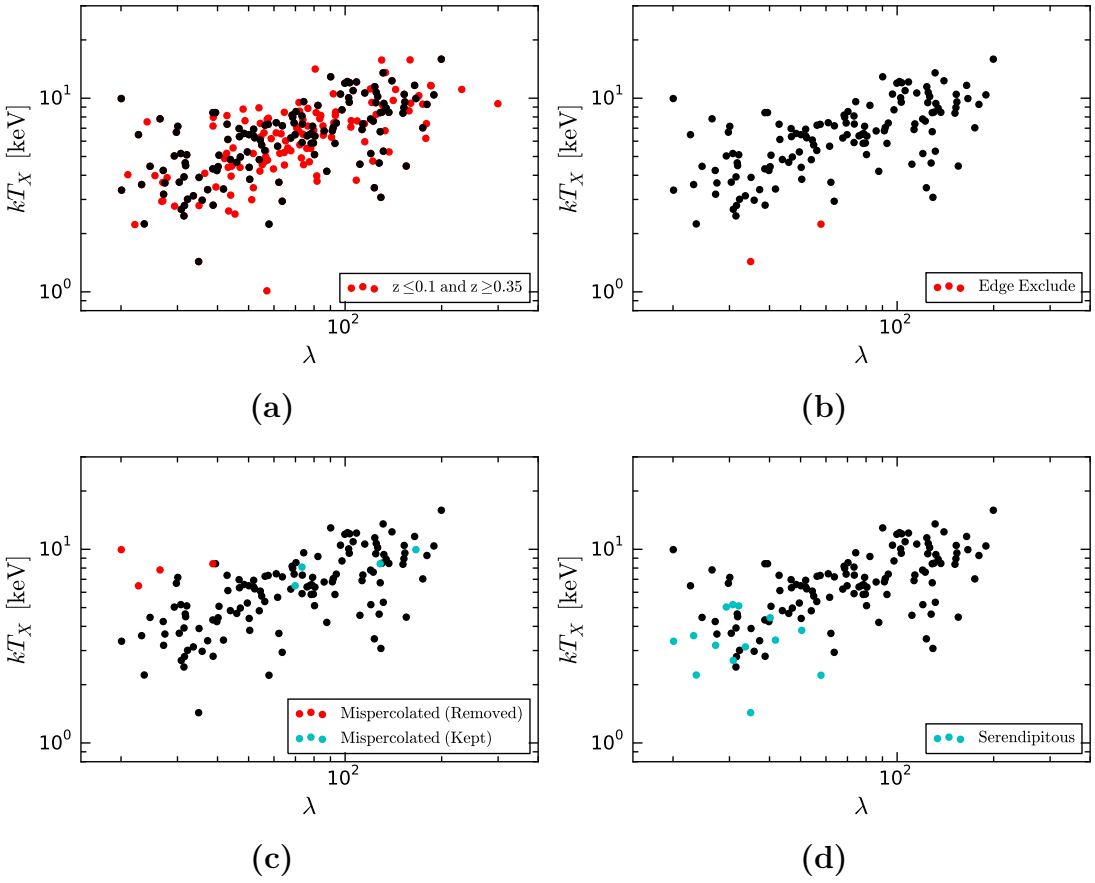

In each image, the red dots mark clusters which we cut from at least one of the relations in section 4.1–section 4.2, cyan dots mark interesting clusters which are not cut, and black dots mark un-flagged data points. (a) Here we see the effects of limiting our data to $0.1 < z < 0.35$. The red dots lie outside this redshift range; the black dots lie inside of it. The choice to limit our data to $0.1 < z < 0.35$ does not seem to preferentially select particular temperatures or richnesses, and indeed in Tables 4.1–4.2 we see no significant effect of this choice upon our fitted slope or scatter. This redshift cut removes a number of T_X-λ outliers. We conjecture that these outliers are caused by issues with *redMaPPer*'s richness assignment outside of $0.1 < z < 0.35$, see Rykoff et al. (2014) for details. (b) Here we see the effects of excluding clusters which are marked as being likely too close to the chip edge to reliably measure their r_{2500} temperature. The two excluded clusters marked in red are clear outliers, likely with under-estimated temperatures. (c) Here we see the effects of excluding mispercolated halos. The four mispercolated halos marked in red are clear outliers with under-estimated richnesses, as expected (see section 3.7). Marked in cyan are the corresponding halos which we keep after manually adjusting their properties (see Table 3.1). (d) Marked in cyan here are our serendipitous clusters (see section 3.6). These clusters primarily inhabit the low-temperature, low-richness regime; this is somewhat intuitive because more massive clusters at these redshifts are more likely to have been specifically studied in X-ray. Unfortunately, there are too few serendipitous clusters to use them to draw meaningful conclusions about the effects of our archival cluster selection, as briefly discussed in section 4.4.

Chapter 4

MATCha Analysis of the Sloan Digital Sky Survey *redMaPPer* Catalog

We use *MATCha* to analyze data from the *redMaPPer* v. 6.3.1 SDSS DR8 catalog containing clusters with $\lambda > 20$. This catalog contains 26,308 potential galaxy clusters, 863 of which fell within a public archival *Chandra* observation as of the time at which we ran the *MATCha* pipeline (see section 3.1). For a full description of the *redMaPPer* v. 6.3.1 SDSS DR8 catalog, see Rykoff et al. (2016). Of these 863 clusters, we successfully clean 850 clusters (as described in section 3.1). Of these 850 clusters, 447 are considered "detected", and 403 are considered "undetected". We then manually review each of these clusters as described in section 3.6, removing 39 of the 447 detected clusters. (Information for clusters removed in review is still available in Hollowood et al. (2018).) After removing these problematic clusters, we find r_{2500} temperatures for 235 clusters of the 408 remaining detected clusters. We find r_{2500} luminosities for each of these

235 clusters via the method described in section 3.2. Out of the 235 clusters for which we find an r_{2500} luminosity and temperature, we additionally find an r_{500} luminosity and temperature for 190 clusters. For 172 of the 173 valid detected clusters with no r_{2500} temperature, we successfully estimate r_{2500} luminosities via the method described in section 3.4[1]. We place 3σ L_X upper limits on all 403 "undetected" clusters. We identify 89 of the 408 detected clusters as serendipitous (see section 3.6), and fit r_{2500} temperatures to 29 of these.

All luminosities quoted in this section are rest-frame, and are soft-band (0.5–2.0 keV) unless otherwise noted. We consider bolometric luminosities (0.001–100 keV) only for the purpose of comparison with scaling relations from the literature.

4.1 X-ray Observable–Richness Scaling Relations

For the regression analysis, we employ the hierarchical Bayesian model proposed in Kelly (2007). This method uses a Gaussian mixture model to estimate the distribution of the independent variable. We choose this method because it provides an unbiased estimation of the scaling parameters for data with correlated and heteroscedastic measurement uncertainties and accounts for the effect of censored data and correlated and heteroscedastic measurement uncertainties. To compute the joint posterior distribution of the model parameters, we run a Gibbs sampler algorithm proposed in Kelly (2007). The marginalized estimate of the model parameters are summarized in Tables 4.1–4.2, and select relations are highlighted below. Our derived relations are of the form $\ln(y) = \alpha \ln(\lambda/70) + \beta$, where λ is the cluster richness.

In the presented relations, we primarily focus on data within the redshift range

[1]The remaining cluster is Abell 1795, which has a massive 88 *Chandra* observations. Analyzing this many simultaneous observations with *XSPEC* triggers *MATCha*'s internal time limits for its subprocesses, and *XSPEC* is terminated before it can produce anything useful.

Table 4.1: r_{2500} X-Ray Observable Scaling with Richness

Relation	β	α	$\sigma_{\rm intr}$	Figure
$T_X - \lambda$ (all redshift)	1.82 ± 0.02	0.54 ± 0.04	0.26 ± 0.02	Figure 4.1 (a)
$T_X - \lambda$ ($0.1 < z < 0.35$)	1.85 ± 0.03	0.52 ± 0.05	0.27 ± 0.02	Figure 4.1 (b)
$L_X - \lambda$ (all redshift, w/o upper limits)	-0.08 ± 0.05	1.37 ± 0.08	0.84 ± 0.03	Figure 4.3 (a)
$L_X - \lambda$ ($0.1 < z < 0.35$, w/o upper limits)	-0.08 ± 0.07	1.31 ± 0.12	0.92 ± 0.05	Figure 4.3 (b)
$L_X - \lambda$ ($0.1 < z < 0.35$, w/o upper limits, fit T_X)	0.02 ± 0.09	1.11 ± 0.16	0.99 ± 0.06	—
$L_X - \lambda$ ($0.1 < z < 0.35$, w/ upper limits)	-0.26 ± 0.08	1.78 ± 0.12	1.04 ± 0.06	Figure 4.3 (c)

Relations are of the form $\ln(y) = \alpha \ln(\lambda/70) + \beta$, where λ is the cluster richness. L_X is normalized by $E(z)$ and has units of 10^{44} ergs/s; T_X has units of keV. $\sigma_{\rm intr}$ is the standard deviation of the intrinsic scatter in this relation. The $L_X - \lambda$ (all redshift without upper limits), $L_X - \lambda$ ($0.1 < z < 0.35$, w/o upper limits, fit T_X), and $T_X - \lambda$ ($0.1 < z < 0.35$) relations have scatter distributions which are slightly asymmetric, with a longer tail in the large-scatter direction. Uncertainties are listed as their 1σ values. The L_X relation labeled "fit T_X" contains only L_X values which were calculated alongside T_X (see section 3.2, c.f. section 3.4).

Table 4.2: r_{500} X-Ray Observable Scaling with Richness

Relation	β	α	$\sigma_{\rm intr}$	Figure
$T_X - \lambda$ (all redshift)	1.83 ± 0.03	0.54 ± 0.05	0.28 ± 0.02	Figure 4.2 (a)
$T_X - \lambda$ ($0.1 < z < 0.35$)	1.86 ± 0.03	0.51 ± 0.05	0.24 ± 0.03	Figure 4.2 (b)
$L_X - \lambda$ (all redshift, fit T_X)	0.46 ± 0.06	1.07 ± 0.11	0.77 ± 0.04	Figure 4.4 (a)
$L_X - \lambda$ ($0.1 < z < 0.35$, fit T_X)	0.44 ± 0.09	1.02 ± 0.15	0.84 ± 0.06	Figure 4.4 (b)

Relations are of the form $\ln(y) = \alpha \ln \lambda/70 + \beta$, where λ is the cluster richness. L_X is normalized by $E(z)$ and has units of 10^{44} ergs/s; T_X has units of keV. $\sigma_{\rm intr}$ is the standard deviation of the intrinsic scatter in this relation. Uncertainties are listed as their 1σ values. The L_X relations contain only L_X values which were calculated alongside T_X (see section 3.2, c.f. section 3.4). The scatter distributions for each of these relations are slightly asymmetric, with longer tails in the large-scatter direction.

$0.1 < z < 0.35$. This redshift range is chosen because it selects the best possible data from *redMaPPer* (Rykoff et al., 2014). At $z < 0.1$, *redMaPPer* centering degrades due to an increased fraction of poorly measured central galaxies and observations flagged for processing issues. At $z > 0.35$, *redMaPPer*'s scatter in both richness and redshift are significantly increased by the 4000 Å break transitioning SDSS bands, and by SDSS's magnitude limit. See Rykoff et al. (2014) for more details on these effects. We choose to limit our manual follow-up of undetected clusters to this $0.1 < z < 0.35$ range due to their sheer number. We thus only present upper-limit luminosities for this redshift range.

For $T_X - \lambda$ in the $0.1 < z < 0.35$ range, r_{2500} aperture, we derive

$$\ln\left(\frac{k_B T_{X,r2500}}{1.0\text{keV}}\right) = (0.52 \pm 0.05)\ln\left(\frac{\lambda_{r2500}}{70}\right) + (1.85 \pm 0.03) \tag{4.1}$$

with standard-deviation-of-intrinsic-scatter $\sigma_{\text{intr}} = 0.27 \pm 0.02$. We thus constrain σ_{intr} within 7%. This does not differ significantly from our derived all-redshift T_X-λ relation in slope, intercept, or σ_{intr}.

We now compare our T_X-λ relation with those presented in two previous *redMaPPer* papers: Rozo and Rykoff (2014) and Rykoff et al. (2016). For the former, we compare to their data from the ACCEPT cluster catalog (Cavagnolo et al., 2009). This is a collection of galaxy clusters with deep *Chandra* data, and which lists X-ray temperatures in radial bins. Rozo and Rykoff (2014) then summarizes each cluster's radial temperature profile into a single temperature within 400 kpc, which is additionally core-excised at 150 kpc if doing so is practical. The total sample used by Rozo and Rykoff (2014) is 56 clusters. Our relation's intercept agrees well with this ACCEPT relation, which (after normalization to our choice of pivots) is listed as 1.852 ± 0.032. However, their derived slope of 0.407 ± 0.066 is shallower than ours by 1.4σ. Additionally, they derive a much

lower $\sigma_{\rm intr}$ of 0.196 ± 0.021. We conjecture these differences are primarily due to the fact that their sample is composed of well-known, bright, rich clusters and pointed observations.

Rykoff et al. (2016) instead combines data for 14 clusters from the *MATCha* pipeline and 14 clusters from a similar *XMM* pipeline (Lloyd-Davies et al., 2011), both using non-core-excised temperatures within r_{2500}. Rykoff et al. (2016) calculates a slope of 0.61 ± 0.09 and an intercept of 1.52 ± 0.07, with $\sigma_{\rm intr} = 0.28^{+0.07}_{-0.05}$. These data have been normalized to our pivots, and we have used the relation quoted in Rykoff et al. (2016) to convert the *XMM* temperatures to equivalent *Chandra* temperatures. Our slopes are in statistical agreement, with their slope differing from ours by 0.9σ in the opposite direction of Rozo and Rykoff (2014). In this case our $\sigma_{\rm intr}$ agrees nicely as well. Their intercept here appears to disagree, however without more information on the uncertainty in their *Chandra*-to-*XMM* conversion it is difficult to determine the degree of disagreement. It is reassuring that our slope and scatter agree with Rykoff et al. (2016), given that they use the *MATCha* pipeline (in conjunction with a similar pipeline for *XMM* data) to supply the X-ray data for their scaling relations.

Due to the low total exposure times of many clusters within our sample and the resulting high uncertainty in our core-excised temperatures, we choose not to present core-excised r_{500} relations here. Plots of our r_{2500} T_X-λ data may be found in Figure 4.1.

We find that our slope, intercept, and $\sigma_{\rm intr}$ do not change significantly when we increase the considered aperture from r_{2500} to r_{500}. Plots of this r_{500} T_X-λ data may be found in Figure 4.2.

Our best-fit to the r_{2500} L_X-richness relation in the $0.1 < z < 0.35$ range,

Figure 4.1: T_X-λ Scaling Relations, r_{2500} Aperture

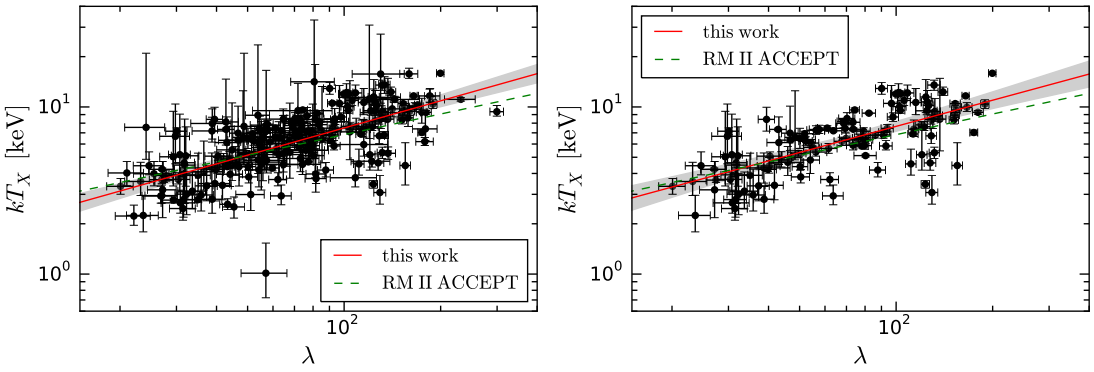

(a) r_{2500} T_X-λ, all redshift. (b) r_{2500} T_X-λ, $0.1 < z < 0.35$. The black dots and associated error bars are the data produced by *MATCha* (see chapter 3). The red lines are the best-fits given in Table 4.1. The surrounding gray areas are the 2σ uncertainties in the fits. The dotted green lines are the ACCEPT T_X-lambda scaling relations from Rozo and Rykoff (2014). For discussion of the outliers in these plots, see section 4.3.

Figure 4.2: T_X-λ Scaling Relations, r_{500} Aperture

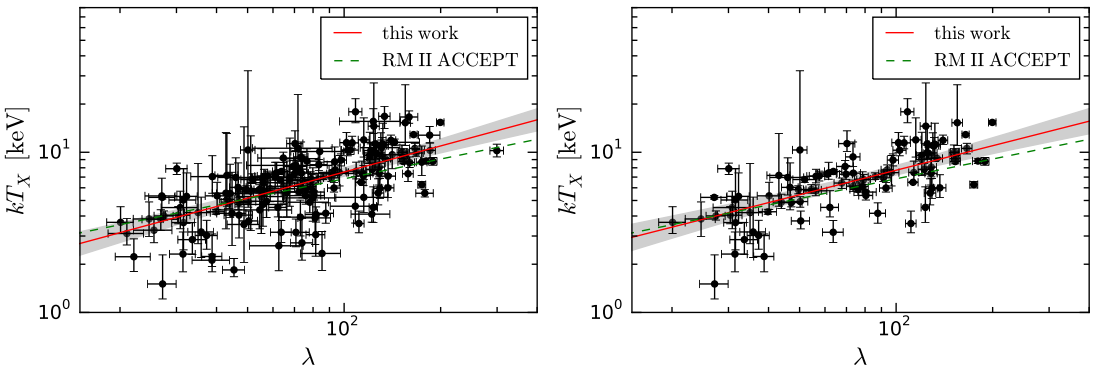

(a) r_{500} T_X-λ, all redshift. (b) r_{500} T_X-λ, $0.1 < z < 0.35$. The black dots and associated error bars are the data produced by *MATCha* (see chapter 3). The red lines are the best-fits given in Table 4.2. The surrounding gray areas are the 2σ uncertainties in the fits. The dotted green lines are the ACCEPT T_X-lambda scaling relations from Rozo and Rykoff (2014).For discussion of the outliers in these plots, see section 4.3.

without taking into account non-detections, is

$$\ln\left(\frac{L_{X,r2500,detected}}{E\left(z\right)\cdot 10^{44}\mathrm{ergs/s}}\right) = (1.31\pm 0.12)\ln\left(\frac{\lambda_{r2500,detected}}{70}\right)+(-0.08\pm 0.07) \quad (4.2)$$

with $\sigma_{\mathrm{intr}} = 0.92 \pm 0.05$. As with T_X-λ, this is not significantly different from the same relation including all redshifts. This suggests that our decision to include L_X upper limits solely in the $0.1 < z < 0.35$ range does not affect our result significantly, however the greater volume of data would help us constrain the L_X-λ σ_{intr} to a greater degree of certainty. When we include luminosity upper limits, we find

$$\ln\left(\frac{L_{X,r2500}}{E\left(z\right)\cdot 10^{44}\mathrm{ergs/s}}\right) = (1.78\pm 0.12)\ln\left(\frac{\lambda_{r2500}}{70}\right)+(-0.26\pm 0.08) \quad (4.3)$$

with $\sigma_{\mathrm{intr}} = 1.04 \pm 0.06$. This is a significant increase in the slope, a significant decrease in the intercept, and a slight increase in σ_{intr}. This steepening of the L_X-λ relation is expected because in the low-λ regime we only detect clusters on the high-L_X side of the scatter. These three L_X-λ relations may be found in Figure 4.3. Additionally, we find that the presence-or-lack of fixed-T_X L_X values (see section 3.4) does not significantly affect σ_{intr}, and has only minor effect on our slope and intercept. For more information on the effects of selection on X-ray scaling relations, see e.g. Mantz et al. (2010) and section 4.4.

We find that our relation has an increased intercept as we widen the considered aperture from r_{2500} to r_{500}. σ_{intr} decreases slightly (from 0.99 ± 0.06 to 0.84 ± 0.06), and the slope does not change significantly. The r_{500} relations may be found in Figure 4.4.

Figure 4.3: L_X-λ Scaling Relations, r_{2500} Aperture

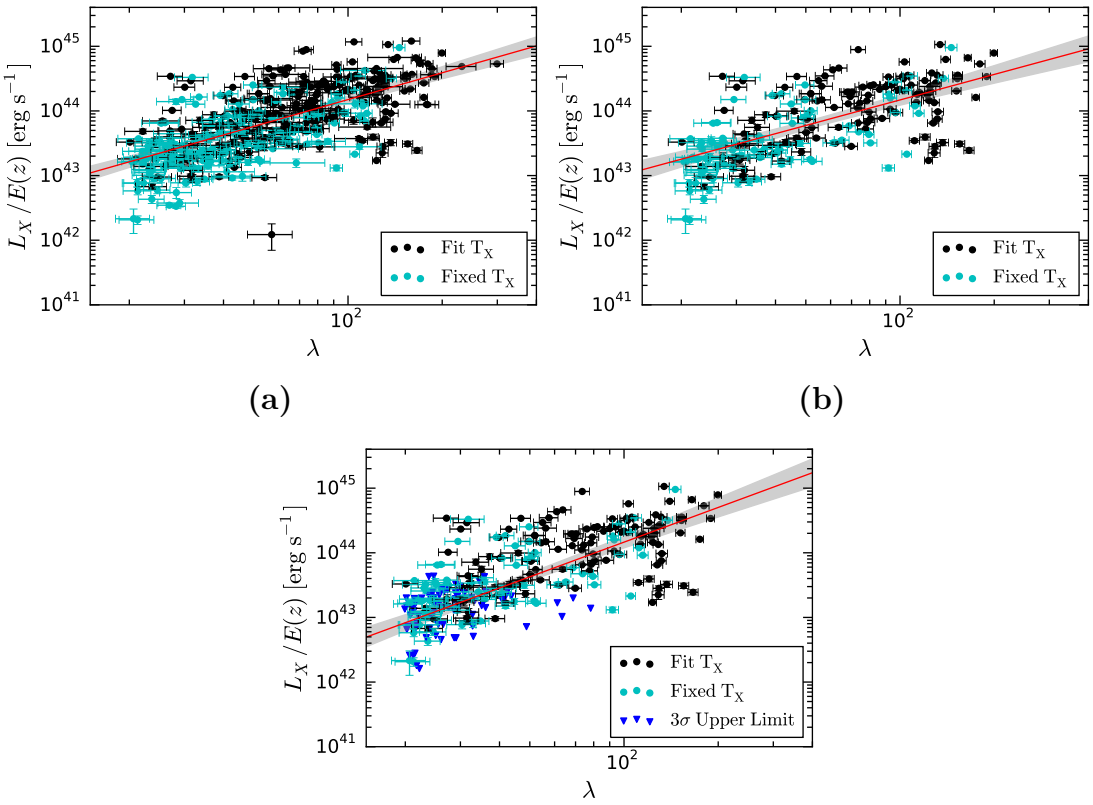

(a) r_{2500} L_X-λ, all redshift, no upper limits. (b) r_{2500} L_X-λ, $0.1 < z < 0.35$, no upper limits. (c) r_{2500} L_X-λ, $0.1 < z < 0.35$, with upper limits. "Fit T_X" (black dots) are clusters which are detected and which have their L_X fit along with their measured T_X, as described in section 3.2. "Fixed T_X" (cyan dots) are detected clusters which have their luminosities fit with an assumed rather than fit T_X, as described in section 3.4. "L_X 3σ upper limit" (blue triangles) are 3σ upper-limit luminosities for undetected clusters, as described in section 3.4. The red lines are the best-fits given in Table 4.1. The surrounding gray areas are the 2σ uncertainties in the fits. The notable outlier in (a) is RM J115807.3+554459.4 (mem_match_id 13419, $z = 0.50$); it is discussed in section 4.3.

Figure 4.4: L_X-λ Scaling Relations, r_{500} Aperture

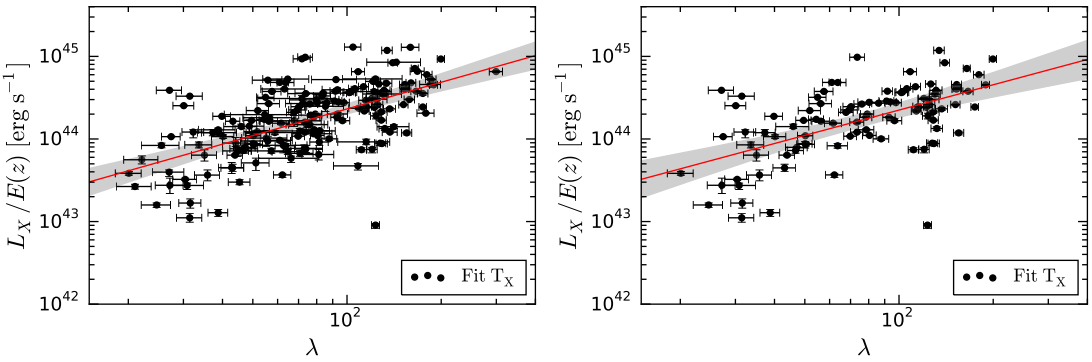

(a) **(b)**

(a) r_{500} L_X-λ, all redshift. (b) r_{500} L_X-λ, $0.1 < z < 0.35$. "Fit T_X" (black dots) are clusters which are detected and which have their L_X fit along with their T_X, as described in section 3.2. The red lines are the best-fits given in Table 4.2. The surrounding gray areas are the 2σ uncertainties in the fits. The striking outlier here is RM J004629.3+202804.8 (mem_match_id 15, $z = 0.10$); see section 4.3 for more information.

4.2 X-Ray–X-Ray Scaling Relations

In addition to our T_X-λ and L_X-λ scaling relations, we derive L_X-T_X and T_X-L_X scaling relations within $0.1 < z < 0.35$. As before, we use the Bayesian fitting method presented in Kelly (2007). Our resulting relations are discussed below in the form $\ln(y) = \alpha \ln(x/\text{pivot}) + \beta$, and are presented in Table 4.3.

For L_X-T_X in r_{2500}, we derive

$$\ln\left(\frac{L_{X,r2500}}{E(z)\cdot 10^{44}\text{ergs/s}}\right) = (2.07 \pm 0.20)\ln\left(\frac{k_B T_{X,r2500}}{2.0\text{keV}}\right) + (-0.05 \pm 0.08) \quad (4.4)$$

with $\sigma_{\text{intr}} = 0.81 \pm 0.06$. Here, there are not many particularly comparable relations from the literature: most papers either choose to excise cluster cores, measure their luminosities in a different band, or use differing instruments (which are known to have an offset when compared with *Chandra*). After a literature

Table 4.3: X-Ray–X-Ray Scaling Relations

Relation	β	α	$\sigma_{\rm intr}$	Figure
r_{2500} $L_X - T_X$ $(0.1 < z < 0.35)$	-0.05 ± 0.08	2.07 ± 0.20	0.81 ± 0.06	Figure 4.5 (a)
r_{2500} $L_X - T_X$ $(0.1 < z < 0.35$, bolometric)	1.08 ± 0.08	2.49 ± 0.19	0.80 ± 0.06	Figure 4.5 (b)
r_{500} $L_X - T_X$ $(0.1 < z < 0.35)$	0.39 ± 0.07	2.08 ± 0.18	0.58 ± 0.06	Figure 4.5 (c)
r_{500} $L_X - T_X$ $(0.1 < z < 0.35$, bolometric)	1.54 ± 0.07	2.53 ± 0.18	0.54 ± 0.06	Figure 4.5 (d)
r_{2500} $T_X - L_X$ $(0.1 < z < 0.35)$	1.89 ± 0.03	0.26 ± 0.03	0.28 ± 0.02	Figure 4.6 (a)
r_{500} $T_X - L_X$ $(0.1 < z < 0.35)$	1.78 ± 0.03	0.32 ± 0.03	0.23 ± 0.02	Figure 4.6 (b)

Relations are of the form $\ln(y) = \alpha \ln(x/\text{pivot}) + \beta$. L_X is normalized by $E(z)$ and has units of 10^{44} ergs/s; T_X has units of keV. When the independent variable, $L_X/E(z)$ has pivot $0.3 \cdot 10^{44}$ and T_X has pivot 2.0 keV. $\sigma_{\rm intr}$ is the standard deviation of the intrinsic scatter in this relation. Uncertainties are listed as their 1σ values.. The scatter distributions for each of these relations are slightly asymmetric, with longer tails in the large-scatter direction.

search, we find that the best comparison for r_{2500} is Hicks et al. (2013), and for r_{500} is Maughan et al. (2012). The comparison with Hicks et al. (2013) is straightforwards in both method of analysis and cluster selection, and we find that our r_{2500} bolometric luminosities agree well with their listed L_X-T_X slope of 2.7 ± 0.5. See Figure 4.5 (b) for a visual comparison.

As we increase our aperture from r_{2500} to r_{500}, we find that the our bolometric L_X-T_X intercept increases to 1.54 ± 0.07, our slope steepens to 2.54 ± 0.18, and our $\sigma_{\rm intr}$ decreases to 0.55 ± 0.05. This differs significantly from Maughan et al. (2012), which lists a slope of 3.63 ± 0.27 for this relation using similar analysis methods. See Figure 4.5 (d) for a visual comparison.

Because the selection effect of L_X in our X-ray data is much stronger than that of T_X (see section 4.4), it is desirable to examine the reverse relation with L_X as the dependent variable. We derive a soft-band T_X-L_X relation within $0.1 < z < 0.35$

Figure 4.5: L_X-T_X Relations

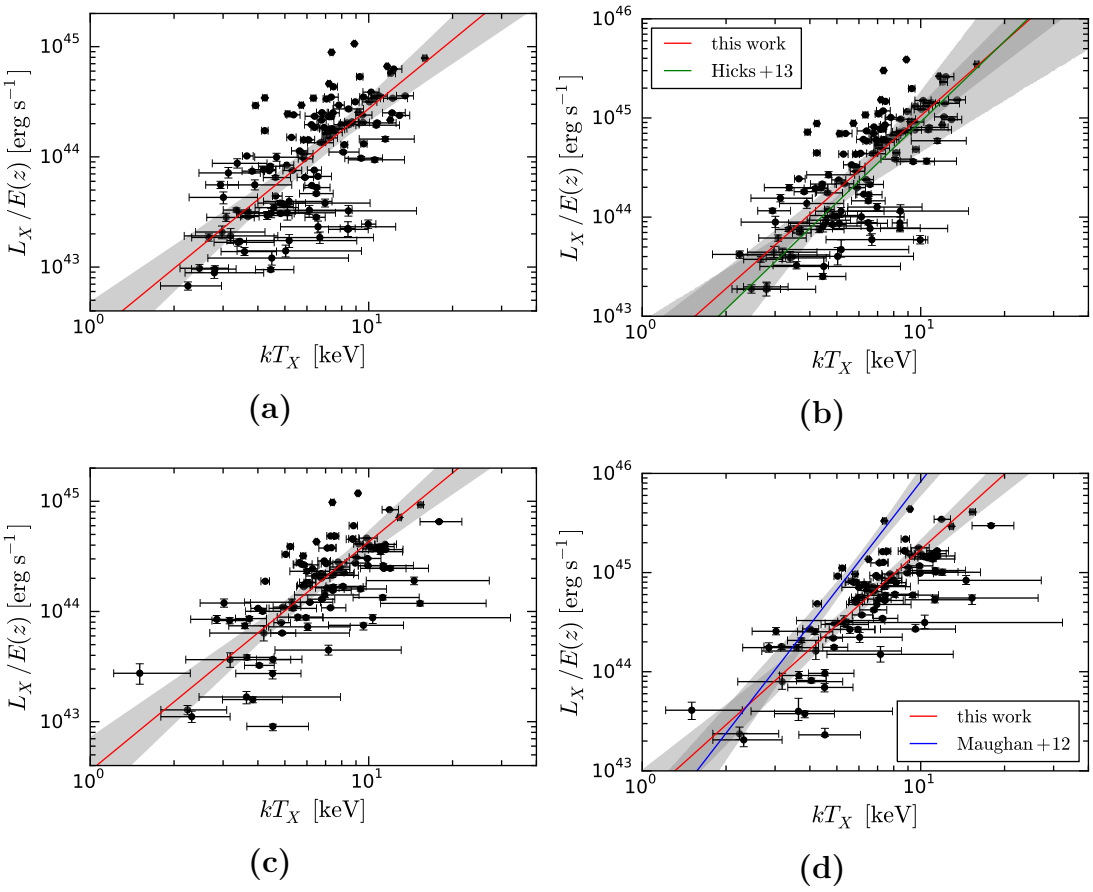

(a) r_{2500} soft-band L_X-T_X, $0.1 < z < 0.35$. (b) r_{2500} bolometric L_X-T_X, $0.1 < z < 0.35$. (c) r_{500} soft-band L_X-T_X, $0.1 < z < 0.35$. (d) r_{500} bolometric L_X-T_X, $0.1 < z < 0.35$. In each figure, the L_X and T_X obtained by *MATCha* are shown in black. The red line represents the best-fit given in Table 4.1. The surrounding gray area is the 2σ uncertainty in our fit. In figure (b), the green line represents the best-fit given in Hicks et al. (2013). In figure (d), the blue line represents the best-fit given in Maughan et al. (2012). In figures (b) and (d), we mirror Hicks et al. (2013)'s and Maughan et al. (2012)'s choice to use bolometric luminosities.

of

$$\ln\left(\frac{k_B T_X}{1.0\text{keV}}\right) = (0.26 \pm 0.03)\ln\left(\frac{L_X}{E(z)\cdot 10^{44}\text{ergs/s}}\right) + (1.89 \pm 0.03) \qquad (4.5)$$

with $\sigma_{\text{intr}} = 0.28 \pm 0.02$. At r_{500}, the intercept drops to 1.78 ± 0.03, the slope increases to 0.32 ± 0.03, and the scatter drops to 0.23 ± 0.02. These results are shown in Figure 4.6.

Figure 4.6: T_X-L_X Relations

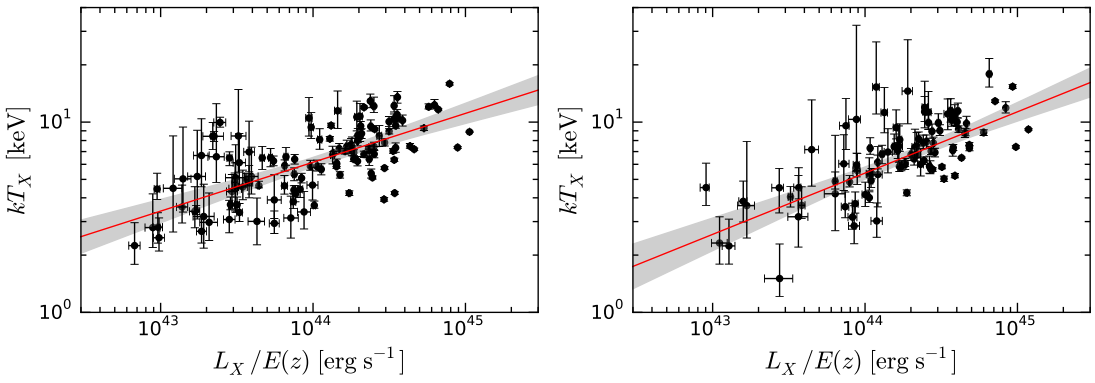

(a) **(b)**

(a) r_{2500} soft-band T_X-L_X, $0.1 < z < 0.35$. (b) r_{500} soft-band T_X-L_X, $0.1 < z < 0.35$. In each figure, the T_X and L_X obtained by *MATCha* are shown in black. The red line represents the best-fit given in Table 4.2. The surrounding gray area is the 2σ uncertainty in our fit.

4.3 Scaling Relation Outliers

As can be seen in Figures 4.1–4.4, there are a number of clusters that seem to have high richnesses for their X-ray properties. These clusters tend to be low-T_X clusters showing evidence of projection effects: *redMaPPer* has added correlated foreground and/or background halos to these clusters, increasing their richness significantly. For more information on projection effects in *redMaPPer*, see e.g.

Rozo et al. (2015b) and Costanzi et al. (2018).

An example of this is RM J004629.3+202804.8 (see Figure 4.7), which is actually a supercluster composed of three separate galaxy clusters. *redMaPPer* merges these separate galaxy clusters into one single large cluster with a very large richness. This is the striking low-L_X, high-richness outlier in Figure 4.4.

Figure 4.7: RM J004629.3+202804.8 Supercluster

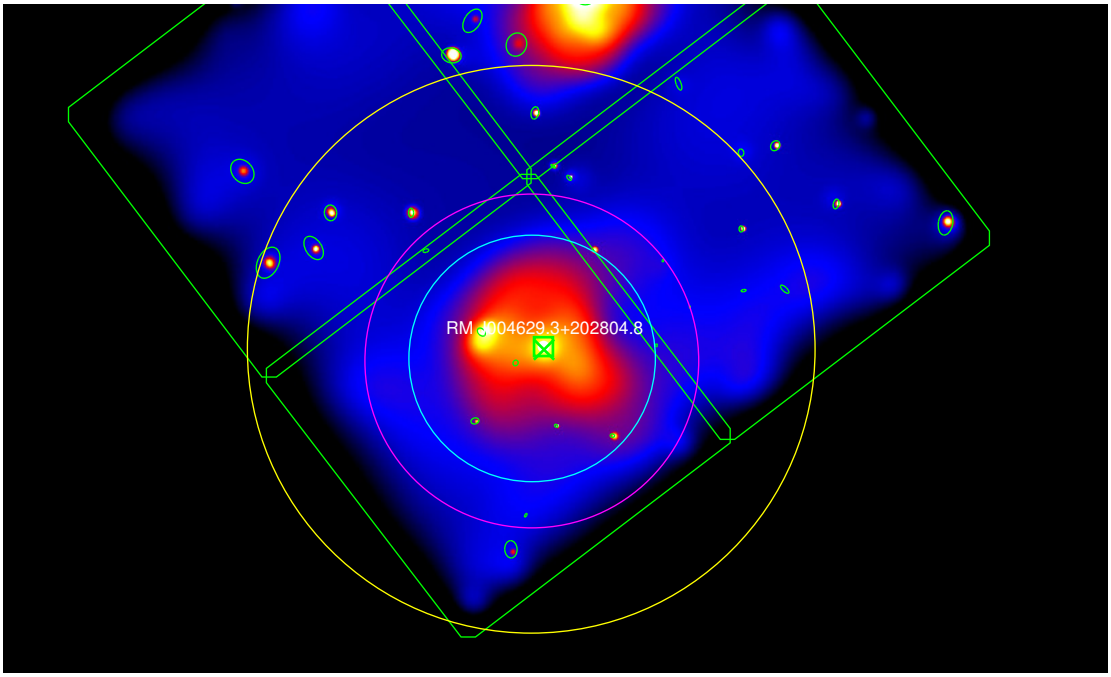

RM J004629.3+202804.8 (mem_match_id 15, $z = 0.10$), ObsID 11876, ACIS-I detector. This "galaxy cluster" is actually three separate halos which lie near to one another when projected along line-of-sight (the third halo is in a separate observation, to the south). *redMaPPer* incorrectly counts this as a single cluster with a very large richness of 123.4. Because this sort of error is intrinsic to the *redMaPPer* algorithm, we keep this cluster as-is for our analysis. As with every *Chandra* image in this thesis, this image obeys the coloring conventions described in the caption for Figure 3.1.

Another issue is mispercolation (discussed in section 3.7), in which *redMaPPer* incorrectly divides a single large halo into two or more separate "clusters". We handle these on a case-by-case basis, with a typical decision being to flag the

smaller "galaxy-cluster" as being masked by the larger, true galaxy cluster and thus discarded from our analysis. See section 3.6 for details on the process of flagging galaxy clusters for potential problems, and Figure 3.8 (c) in section 3.9 for a plot of the locations of mispercolated clusters within our r_{2500} T_X-λ data. Were these included, they would be outliers with high T_X/L_X and low λ, and would artificially flatten the slope and increase the scatter of the richness scaling relations.

Finally, there is the notable outlier in Figure 4.3 (a): RM J115807.3+554459.4 (mem_match_id 13419, $z = 0.50$). After careful checking of the *MATCha* X-ray analysis, we believe that *redMaPPer* has significantly overestimated the richness of this cluster. This is likely due to an issue in *redMaPPer*'s extrapolation of richness for high-z clusters (see chapter 2).

4.4 Effects of Selection

Due to the archival nature of our sample, our results may exhibit bias due to selection. Bigger, brighter clusters may have been more likely to be the object of *Chandra* observations than less-luminous clusters at the same redshift. Were this effect equivalent to a simple flux cut on our data, we would see the effects of classic Malmquist bias: we would observe a decreased slope and scatter in our L_X-λ relations when compared with unbiased data (Mantz et al., 2010). Indeed, we explore the effects of applying a flux cut to simulated *redMaPPer* data and find that removing low-flux clusters flattens the slope of our resulting L_X-λ relation. In truth our selection function is much more complicated than a flux cut. This is because observers will choose longer exposure times for dimmer clusters if those clusters are known prior to observation. Thus more sophisticated modeling is needed, and such modeling is well beyond the scope of this thesis.

There are a number of ways of probing the effects of our selection function on our fitted L_X-λ relation. When we include upper limits in L_X-λ, we see our slope increase. The scatter does not increase significantly. When we compare serendipitous and non-serendipitous clusters (see section 3.6), we see that the former have a lower scatter than the latter. Here the slope does not change significantly. This change in scatter may be due to the fact that serendipitous clusters primarily lie within the low richness regime, where our sample is less complete (see Figure 3.8 (d)). These aspects of our data make some intuitive sense: including upper limits helps take into account the fact that we are missing low-luminosity clusters, and serendipitous clusters should be less effected by observers' selection biases than clusters which were the targets of pointed observations.

We find that our T_X-λ relations are significantly less susceptible to these selection effects than our L_X-λ relations. We do not find any significant effect on our fitted r_{2500} T_X-λ slope from limiting our sample to serendipitous clusters nor from our simulated flux cut. Additionally, we have a complete sample of r_{2500} T_X values for *redMaPPer* clusters above $\lambda = 120$ and within $0.1 < z < 0.3$. This complete sample exhibits a larger scatter in r_{2500} T_X-λ than our full catalog in the same redshift range, at 0.37 ± 0.07 vs. our full catalog's $\sigma_{\rm intr}$ of 0.27 ± 0.02. This effect may be due to the presence in this sample of an unusually high fraction of clusters with projection problems (see section 4.3) when compared with our full sample. The complete sample's fitted slope has too large an uncertainty to draw conclusions there; its intercept is similarly uninstructive.

4.5 Centering

In order to understand the *redMaPPer* miscentering function, we compare the *redMaPPer* position with our X-ray centroids, which we calculate as described in

section 3.2 step 1 and measure within r_{2500}. We additionally compare *redMaPPer* positions with X-ray peak positions (see section 3.5).

Centroids and peaks have differing merits as measures of galaxy cluster centers in X-ray. Consider a merging cluster composed of two sub-halos of roughly the same size, each within r_{2500} (e.g. Figure 4.8 (a)), or a cluster which is a composed of a single "lumpy" halo (e.g. Figure 4.8 (b)). In these cases, the centroid will be located between subhalos, near the cluster's center of mass. The peak will be located on one of the subhalos, along with the *redMaPPer* center, which by definition is centered on a galaxy. Indeed, this similarity of definition implies that the *redMaPPer* center should more closely align with the X-ray peak than the X-ray centroid as a general trend, although as demonstrated by both the above clusters it also is possible that the *redMaPPer* center will not be on the same subhalo as the X-ray peak and will thus instead be nearer to the X-ray centroid.

For practical use, the "correct" choice of centering measure depends on the purpose for which you are using the centers. For example a weak lensing pipeline based on simulations would probably wish to choose a centering measure which aligns with the centers chosen by their simulated data, irrespective of whether that center is the center of mass, the densest point, or something else.

Comparisons of the *redMaPPer* position, the r_{2500} X-ray centroid, and the X-ray peak (after the sample cleaning discussed on section 3.6) are shown in Figure 4.9. We find that $68.3 \pm 6.5\%$ of *redMaPPer* central galaxies are within 0.1 R_λ of the peak and $65.1 \pm 6.7\%$ are within the same distance of the centroid. Here R_λ is the richness-scaling radius measure defined in Rykoff et al. (2012) and described in chapter 2.

In Figure 4.9 it is clear that although many clusters are well-centered, there is a long tail to the *redMaPPer* centering distribution. In examining the clusters

Figure 4.8: *redMaPPer* Miscentering Examples

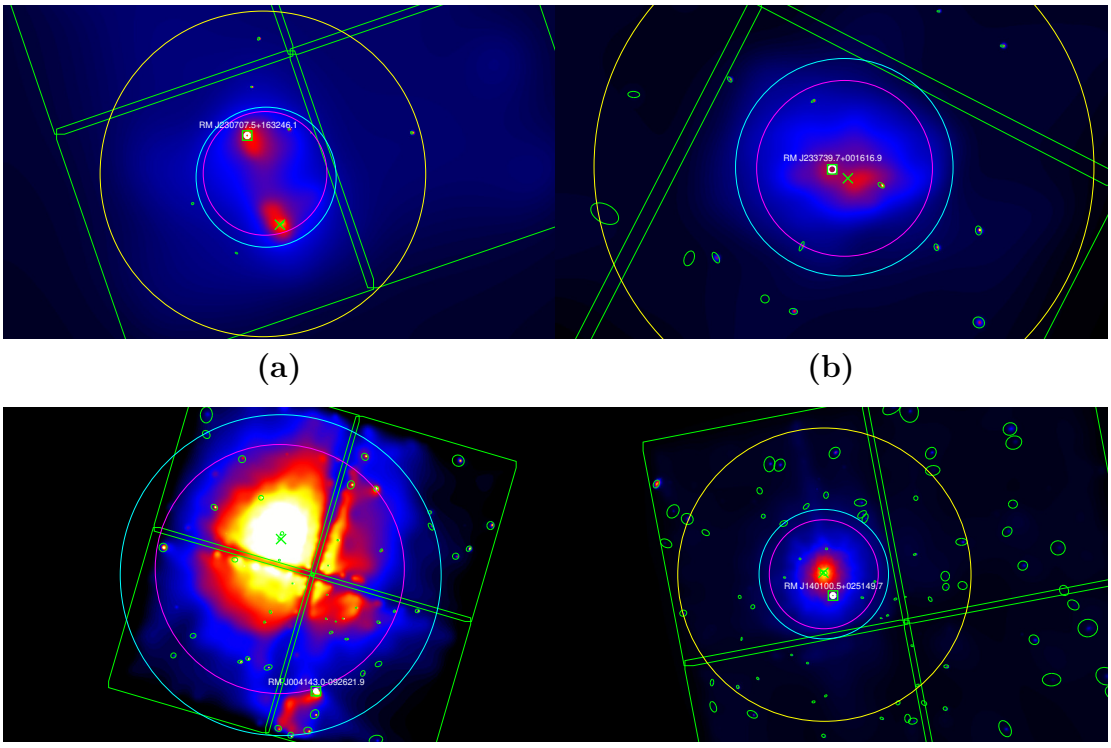

(a) RM J230707.5+163246.1 (mem_match_id 46, $z = 0.25$), ObsID 17157, ACIS-I detector. This cluster has two sub-halos of nearly the same size, so the centroid is located between the two sub-halos. However, the *redMaPPer* center is at the central galaxy of upper halo. The X-ray peak is on the lower halo, so in this case *redMaPPer*'s center agrees with neither X-ray centering measure. (b) RM J233739.7+001616.9 (mem_match_id 68, $z = 0.30$), ObsID 11728, ACIS-I detector. This cluster has been disturbed in such a way that the *redMaPPer* center does not agree well with the X-ray centroid or with the X-ray peak. (c) RM J004143.0−092621.9 (mem_match_id 145, $z = 0.07$), ObsID 16264, ACIS-I detector. In this example, *redMaPPer* chose to center on the small southern substructure (at $z = 0.07$) instead of the large structure which dominates the observation (at $z = 0.06$). (d) RM J140100.5+025149.7 (mem_match_id 43, $z = 0.26$), ObsID 6880, ACIS-I detector. Here, the central galaxy has an active galactic nucleus (marked by a green ellipse surrounding the X-ray peak). This causes the central galaxy to appear blue. As a result, *redMaPPer* ignores the true central galaxy and instead chooses an off-center galaxy as its most-likely central galaxy. As with every *Chandra* image in this thesis, these images obey the coloring conventions described in the caption for Figure 3.1.

Figure 4.9: *redMaPPer* Centering Distribution

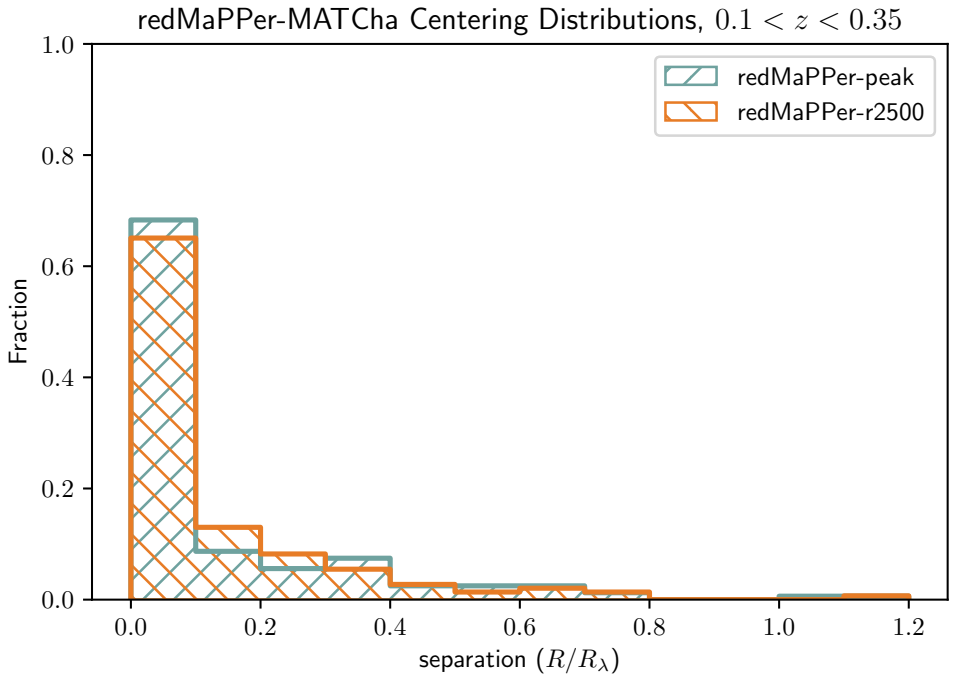

Centering distributions. The histogram labeled "*redMaPPer*-peak" shows the offset between the *redMaPPer* central galaxy and the X-ray peak. The histogram labeled "*redMaPPer*-r_{2500}" shows the offset between the *redMaPPer* central galaxy and the X-ray centroid within r_{2500}. Of the two X-ray centering measures, the peak somewhat better agrees with the *redMaPPer* definition of cluster center.

composing this tail, we identify the following major failure modes for *redMaPPer* centering.

1. *redMaPPer* picks a central galaxy in a small cluster substructure, instead of in the main substructure. See Figure 4.8 (c).

2. *redMaPPer* splits a single cluster into two separate clusters, or mis-assigns galaxies from one cluster to another nearby cluster. This can lead to choosing an incorrect center in the affected clusters and may cause *redMaPPer* to assign wildly incorrect cluster richnesses. We call this problem "mispercolation" and discuss it in section 3.7. Figures 3.4–3.5 examine the four cases of mispercolation that we observe in our data.

3. The central galaxy is too blue and is thus ignored by *redMaPPer*'s central galaxy selection algorithm. This leads *redMaPPer* to choose an off-center galaxy instead. This problem often occurs when the central galaxy features an active galactic nucleus or significant ongoing star formation. See e.g. Figure 4.8 (d).

4. *redMaPPer* misses the central galaxy due to masking caused by a bright star located along the line-of-sight, or due to data problems such as missing observations. See Rykoff et al. (2014) for more information.

For more information on *redMaPPer* centering, including data from *MATCha* and a comparison with X-ray centers from *XMM*, see Zhang et al. (in prep.).

Chapter 5

MATCha Analysis of the Dark Energy Survey Year 1 Results

We next run *MATCha* on DES Year 1 (Y1) data, iterating on the analysis of chapter 4. DES Y1 data were taken between August 31, 2013 and February 9, 2014. These data span 1839 deg^2 ($\approx {}^1/_{20}{}^{\text{th}}$ of the sky), and are taken in optical g, r, i, and z bands. This area is chosen to overlap SDSS Stripe 82 and the **S**outh **P**ole **T**elescope (**SPT**) Sunyaev-Zeldovich Survey. See Figure 5.1 for an visual representation of the footprint. The DES Y1 data are publicly available; see Abbott et al. (2018). These data are then processed with *redMaPPer* v. 6.4.17, and the resulting $\lambda > 20$ volume-limited catalog is analyzed with *MATCha*. Note that while similar, DES Y1 richnesses measured with *redMaPPer* v. 6.4.17 do not perfectly agree with the richnesses measured with chapter 4's *redMaPPer* v. 6.3.1. Zhang et al. (in prep.) derives $\lambda_{6.4.17} = (0.88 \pm 0.03)\lambda_{6.3.1} + (3.28 \pm 1.20)$. Some of this difference may be due to differences in input data set.

Our DES Y1 *MATCha* analysis examines 212 *redMaPPer* clusters which fall within archival *Chandra* observations. Of these 212 clusters, we successfully clean 205 clusters (as described in section 3.1). Of these 205 clusters, 100 are considered

Figure 5.1: DES Year 1 Footprint

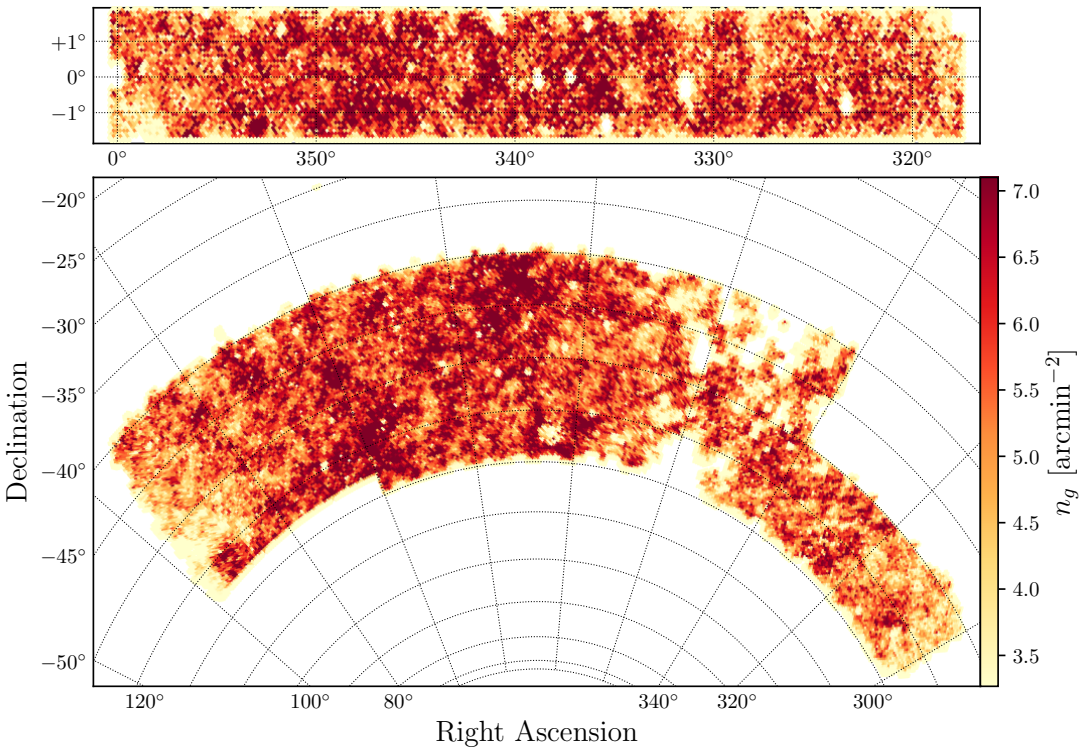

Surface density of galaxies within the DES Year 1 footprint. Top: The SDSS Stripe 82 overlap field. Bottom: The SPT Sunyaev-Zeldovich Survey overlap field. Plot taken from McClintock et al. (2018).

"detected", and 105 are considered "undetected". Our manual review (section 3.6) removes 19 of the 100 detected clusters. We find r_{2500} temperatures for 68 of the 81 remaining detected clusters. We find r_{2500} luminosities for each of these 68 clusters via the method described in section 3.2. Of the 68 clusters for which we find an r_{2500} luminosity and temperature, we find an r_{500} luminosity and temperature for 61 clusters. We successfully estimate r_{2500} luminosities via the method described in section 3.4 for all 13 valid detected clusters with no r_{2500} temperature. We place 3σ L_X upper limits on all 105 "undetected" clusters. We identify 14 of the 75 valid detected clusters as serendipitous (section 3.6), and fit r_{2500} temperatures to five of these.

In Zhang et al. (in prep.) and Farahi et al. (in prep.), techniques presented in chapter 4 are refined and applied to this DES Y1 *MATCha* data in order to study *redMaPPer* centering and T_X–λ scaling, respectively.

5.1 Centering

Miscentering by *redMaPPer* biases cluster masses from weak lensing, but with a miscentering model it is possible to correct for this effect (McClintock et al., 2018). Zhang et al. (in prep.) explores *redMaPPer* centering using both *MATCha* SDSS and DES Y1 data, taking the "true" center to be the r_{2500} X-ray peak measured by *MATCha*. *redMaPPer*'s centering is then modeled as a sum of two separate centering distributions: an exponential distribution for well-centered clusters, and a gamma distribution for miscentered clusters. The resulting fit for SDSS data is shown in Figure 5.2 overlaid on both SDSS and DES Y1 centering distributions. Zhang et al. (in prep.) finds that $\approx 70\%$ of *redMaPPer* clusters are well-centered in both SDSS and DES Y1, agreeing with chapter 4's SDSS well-centered fraction of $68.3 \pm 6.5\%$.

Figure 5.2: *redMaPPer* Centering Model

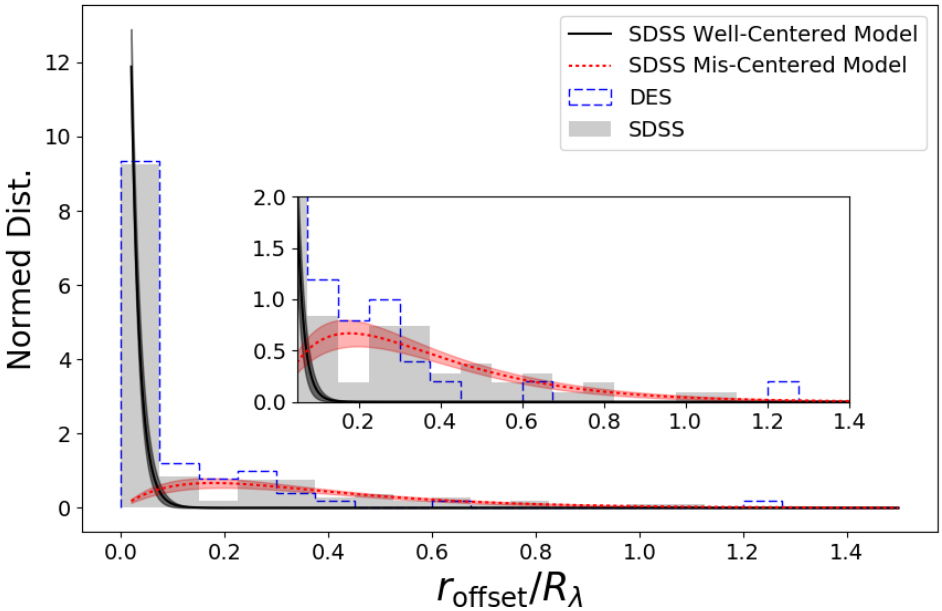

Two-component fit of SDSS centering, overlaid on both SDSS and DES Y1 centering distributions. The fit is comprised of an exponential distribution which models offsets for well-centered clusters, and a gamma distribution which models miscentered clusters. Plot taken from Zhang et al. (in prep.).

In addition to biasing cluster masses from weak lensing, miscentering by *redMaPPer* can bias computed cluster richnesses. Zhang et al. (in prep.) additionally investigates the effect on richness of calculating the richness at the X-ray peak instead of at the *redMaPPer* central galaxy. The shift in richness $\lambda_{redMaPPer}/\lambda_{\text{X-ray}}$ is modeled as Gaussian in $r_{\text{offset}}/r_\lambda$ with a width which increases with the arctangent of the miscentering. It is found that richnesses calculated at the *redMaPPer* center tend to be underestimated compared with richnesses calculated at the X-ray peak, and that this effect becomes stronger as the miscentering increases. This effect is shown in Figure 5.3.

5.2 Scaling Relations

Farahi et al. (in prep.) explores X-ray scaling relations with λ using *MATCha* DES Y1 data and data from the *XMM* pipeline described in Lloyd-Davies et al. (2011). Like chapter 4's SDSS analysis, this paper uses the method from Kelly (2007) to fit an r_{2500} T_X-λ relation.

The primary differences between the DES Y1 analysis in Farahi et al. (in prep.) and the SDSS analysis in chapter 4 are as follows. In Farahi et al. (in prep.), richnesses are calculated at the cluster's X-ray peak instead of at the original *redMaPPer* central galaxy, which helps to remove from the resulting scaling relations the effects of *redMaPPer* miscentering.

Farahi et al. (in prep.) determines an r_{2500} T_X-λ slope of 0.60 ± 0.09. This agrees (within 1σ) with the $0.1 < z < 0.35$ r_{2500} T_X-λ relation found in chapter 4, which has a slope of 0.52 ± 0.05. The derived σ_{intr} differs by 1.6σ, at 0.213 ± 0.029 vs. chapter 4's 0.27 ± 0.02 for $0.1 < z < 0.35$. See Figure 5.4 for a plot of Farahi et al. (in prep.)'s *Chandra* T_X-λ scaling relation, as well scaling relations for an *XMM*-based cluster sample and a combined cluster sample.

Figure 5.3: Miscentering Effects on *redMaPPer* Richness

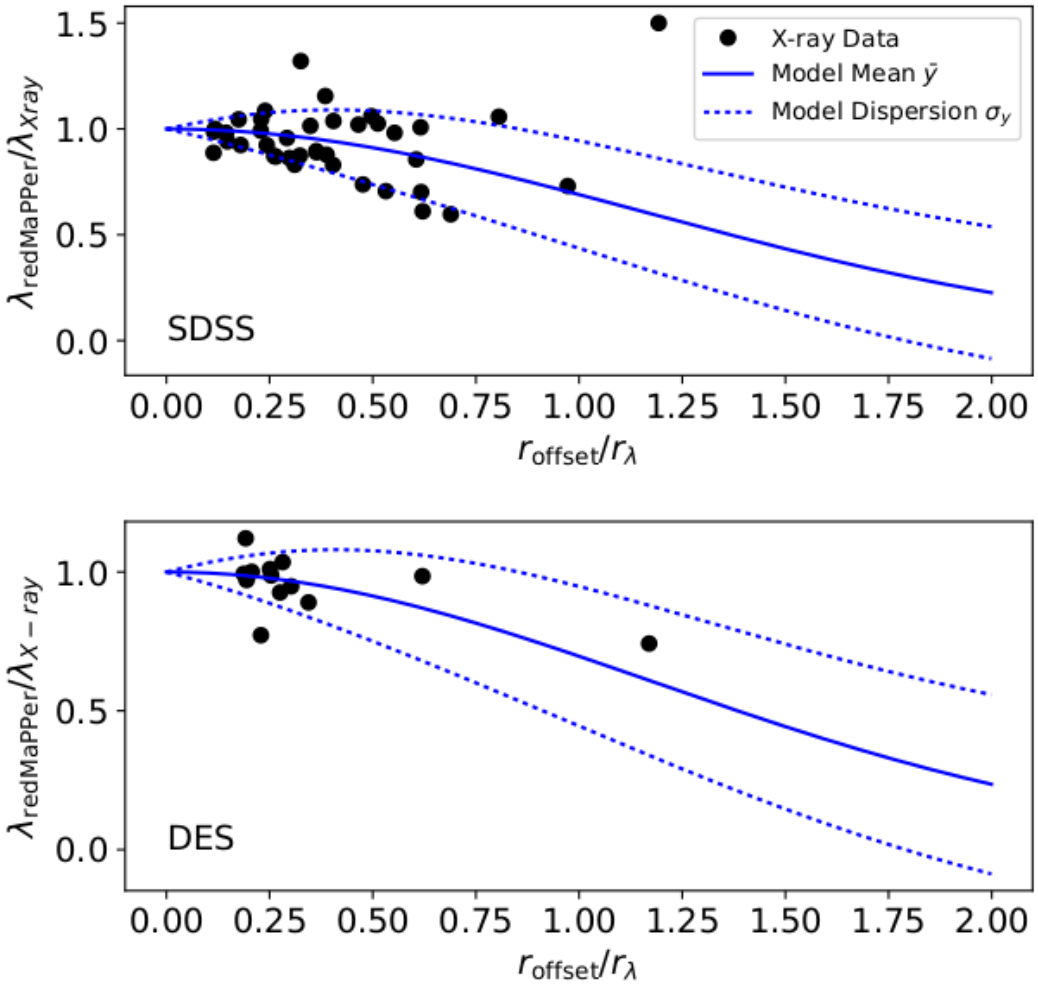

Effects of calculating the richness at the X-ray peak instead of at the *redMaPPer* central galaxy. The model mean is given by $y = \exp(-x^2/\alpha^2)$ and the model dispersion is given by $\sigma_y = \beta \arctan(\gamma x)$, where $y = \lambda_{redMaPPer}/\lambda_{\text{X-ray}}$, $x = r_{\text{offset}}/r_\lambda$, and α, β, and γ are model parameters. In general, centering at the *redMaPPer* central galaxy underestimates the richness; this effect increases with miscentering distance. Plot taken from Zhang et al. (in prep.).

Figure 5.4: DES Year 1 T_X-λ

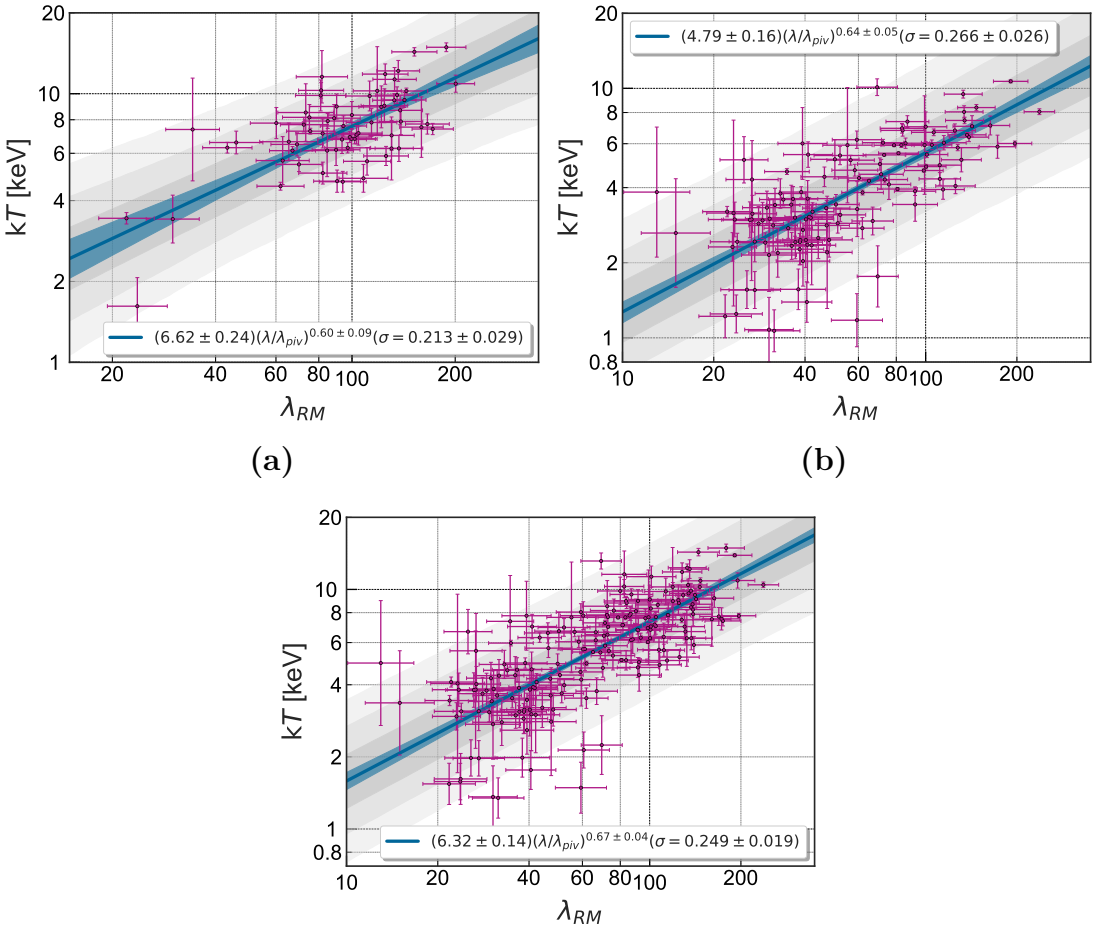

(a) T_X-λ, *Chandra* subsample. (b) T_X-λ, *XMM* subsample. (c) T_X-λ, combined *Chandra* + *XMM* sample. Here *XMM* temperatures have been adjusted using the relation found in Rykoff et al. (2016) to account for the offset between *XMM* and *Chandra* (see Schellenberger et al. (2015)). All plots taken from Farahi et al. (in prep.).

Finally, Farahi et al. (in prep.) combines the *MATCha* and *XMM* data with data from Mantz et al. (2016) and Farahi et al. (2018) to measure the intrinsic scatter in mass given a *redMaPPer* richness, obtaining a value of $\sigma_{\ln M|\ln\lambda} = 0.23^{+0.11}_{-0.09}$. This value is an important prior for DES cluster cosmology, allowing improved modeling of cluster masses from cluster richnesses.

Chapter 6

Further Applications of *MATCha*

In addition to the SDSS results outlined in chapter 4 and the DES Year 1 results outlined in chapter 5, *MATCha* is important as an upstream component of a number of astrophysics research applications. In this section, we briefly discuss *MATCha*'s influence on the calibration of *redMaPPer* on DES Science Verification (SV) data, Bufanda et al. (2017)'s use of *MATCha* in studying galaxy evolution, and the contributions of *MATCha*-driven centering data in the McClintock et al. (2018) and Costanzi et al. (in prep.) weak lensing and cosmology papers.

6.1 *redMaPPer* on DES Science Verification

The earliest published use of *MATCha* is in Rykoff et al. (2016). This paper examines a volume-limited $150\,\mathrm{deg}^2$ sample of galaxies from DES Science Verification data, containing 786 clusters. Of these 786 clusters, 61 fall within a *Chandra* observation, and *MATCha* marks 38 of them as "detected". Note that at the time of this analysis, *MATCha* considered anything with a signal-to-noise ratio of 3.0 to be detected; this cutoff was later raised to the 5.0 cited in section 3.2 when clusters with data within the 3.0–5.0 SNR range were found to be insufficient for

reliable X-ray analysis. *MATCha* fit r_{2500} temperatures and luminosities to 15 of these clusters. Our manual check of clusters removed one additional cluster, leaving a final sample of 14 r_{2500} T_X and L_X values.

By combining these data with *redMaPPer* clusters analyzed with the *XMM* pipeline from Lloyd-Davies et al. (2011) and with South Pole Telescope Sunyaev-Zeldovich data from Saro et al. (2015), Rykoff et al. (2016) examines the quality of *redMaPPer* (v. 6.3) centering and richness estimation. These were determined to be of quality equal to expectations from previous runs of *redMaPPer* on SDSS data, and the application of *redMaPPer* to DES data proceeded from there. The *MATCha* centering data from Rykoff et al. (2016) are additionally used in Melchior et al. (2017)'s estimate of the mass-richness relation from weak lensing.

6.2 The μ_* Optical Mass Observable

In addition to helping *redMaPPer* calibrate their measurement of the richness (λ) optical mass observable, *MATCha* is used in Palmese et al. (in prep.) to develop a new cluster mass observable called μ_*. μ_* is based on the sum of total stellar masses, estimated by combining a collection of stellar population synthesis models via Bayesian Model Averaging (see e.g. Hoeting et al. (1999)). Palmese et al. (in prep.) then compares the calculated μ_* values against T_X values found via *MATCha* and the Lloyd-Davies et al. (2011) *XMM* pipeline. Both X-ray pipelines were run on DES Y1 analysis as outlined in chapter 5. After fitting a T_X-μ_* mass proxy for each pipeline separately (see Figure 6.1), Palmese et al. (in prep.) finds a $\sigma_{\rm intr}$ of $0.138^{+0.015}_{-0.014}$ for *MATCha* T_X-μ_*. This compares favorably with *redMaPPer*'s Y1 $\sigma_{\rm intr}$ of 0.213 ± 0.029. This *MATCha* work thus helps show that Palmese et al. (in prep.)'s μ_* is a competitive optical cluster mass proxy.

Figure 6.1: T_X-μ_* Relation

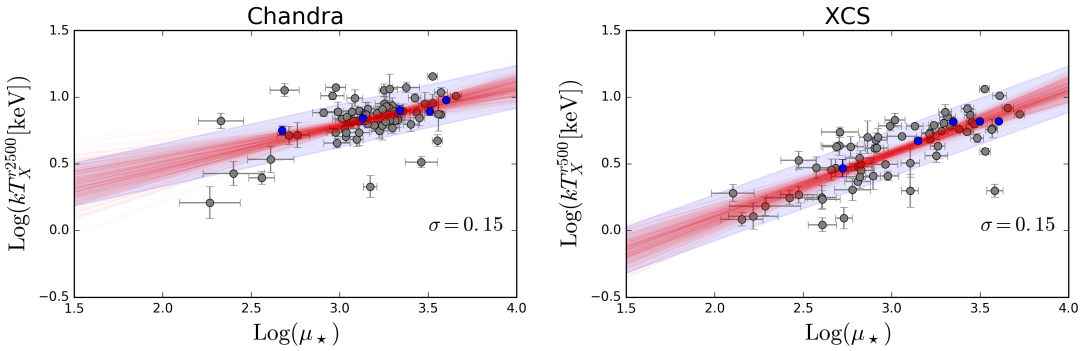

(a) **(b)**

(a) T_X-μ_* relation, using *MATCha*. (b) T_X-μ_* relation, using the *XMM* pipeline from Lloyd-Davies et al. (2011). Figures taken from Palmese et al. (in prep.).

6.3 Active Galactic Nuclei

Galaxies in clusters evolve differently than field galaxies, with notably lower rates of star formation at low redshifts. This is thought to be due to a lack of cold gas in low-redshift cluster galaxies. **A**ctive **G**alactic **N**uclei (**AGN**) are thought to "feed" on cold gas, so this same lack of cold gas should be reflected in a lower fraction of cluster member galaxies which host AGN in low-redshift cluster galaxies. AGN feedback may in turn affect star formation in their host galaxies. Thus the redshift evolution of this galaxy cluster "AGN fraction" may be used to study galaxy formation.

For most of the purposes of this thesis so far (i.e. Chapters 3–5), AGN have been a nuisance to be cut out of the data. As discussed in section 1.2, Active Galactic Nuclei (AGN) emit strongly in X-ray, and thus contaminate the spectra of intracluster media. But as the saying goes, "one person's trash is another person's treasure", and in Bufanda et al. (2017) we use the lists of AGN point sources produced by *MATCha* in order to study the above effects of galaxy environment

on galaxy evolution. In this paper we examine clusters appearing in *redMaPPer*'s DES Science Verification (SV) data (Rykoff et al., 2016), using *redMaPPer* v. 6.3. These data are followed up in 103 *Chandra* observations analyzed with *MATCha*. By matching AGN point sources from *MATCha* with cluster member galaxies from *redMaPPer* and then comparing the number of *redMaPPer* members with and without AGN, we estimate the AGN fraction of galaxy clusters. In order to control for cluster mass, clusters are separated into richness bins and the redshift evolution of each bin is studied separately.

We find that the AGN fraction in clusters increases with redshift (3.6σ), with a marked increase around $z = 0.7$; no significant correlation with cluster mass is found. This may be seen in Figure 6.2. These results agree well with previous work (e.g. Eastman et al., 2007; Martini et al., 2009, 2013).

6.4 Cluster Weak Lensing and Cosmology

The *MATCha*-driven two-component *redMaPPer* miscentering model from Zhang et al. (in prep.) (see section 5.1) provides critical priors for weak lensing studies. Here we discuss two such studies, McClintock et al. (2018) and Costanzi et al. (in prep.).

In McClintock et al. (2018), a volume-limited sample of 6,500 *redMaPPer* DES Y1 clusters with $\lambda > 20$ are split into four richness bins and three redshift bins (for twelve total bins). Weak lensing data for clusters in each of these twelve bins are stacked, their mass is measured, and these masses are compared to the *redMaPPer* richness, deriving a mass-richness relation of the form $M_{200m} = M_0(\lambda/40)^F((1+z)/1.35)^G$. McClintock et al. (2018) measures $M_0 = 3.081 \pm 0.075\,(\text{stat}) \pm 0.133\,(\text{sys}) \cdot 10^{14} M_\odot$, $F = 1.356 \pm 0.051\,(\text{stat}) \pm 0.008\,(\text{sys})$, and $G = -0.30 \pm 0.30\,(\text{stat}) \pm 0.06\,(\text{sys})$; this is considerably more precise than

Figure 6.2: Cluster AGN Fraction Evolution with Redshift

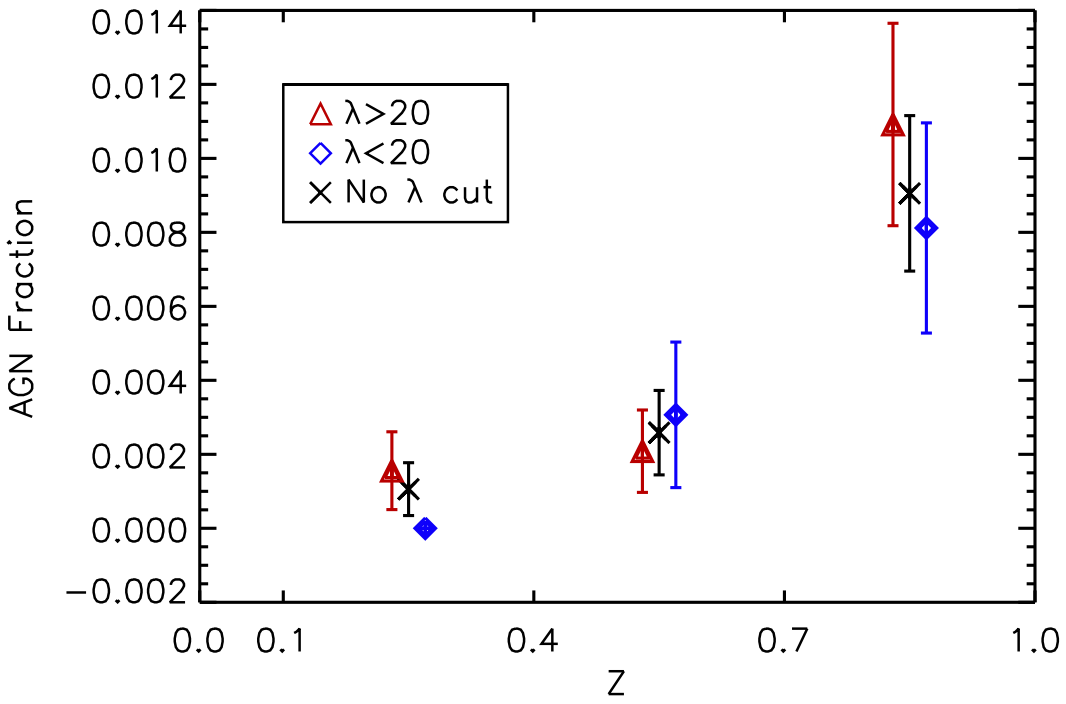

Cluster AGN fraction vs redshift, both separated by richness and combined. The fraction of AGN in clusters increases significantly with redshift. Plot taken from Bufanda et al. (2017).

previously published mass-richness relations.

In Costanzi et al. (in prep.), clusters from 10,000 deg^2 of *redMaPPer* (v. 5.10) SDSS data are combined with galaxy shear data from Reyes et al. (2012). In a blinded analysis, cosmological parameters and a richness-mass relation are simultaneously fit to these data. The results give new constraints on the cosmological density fluctuation amplitude σ_8 (see e.g. Eke et al., 1998; Henry, 2000; Borgani et al., 2001), the relative density of matter Ω_M, and the current value of the Hubble constant H_0.

In both McClintock et al. (2018) and Costanzi et al. (in prep.), uncertainty in *redMaPPer* centering is a critical prior. For the former, miscentering by *redMaPPer* biases weak lensing masses (Johnston et al., 2007); thus McClintock et al. (2018) uses Zhang et al. (in prep.)'s miscentering model to set the prior for the miscentering likelihood in their Bayesian model for their weak lensing profiles. For the latter, miscentering by *redMaPPer* affects calculated richnesses (see section 5.1) and thus the assignment of clusters into richness bins. To remedy this, Costanzi et al. (in prep.) uses Zhang et al. (in prep.)'s miscentering model to determine a systematic correction to apply to observed cluster counts and the corresponding covariance matrix. The use of the Zhang et al. (in prep.)'s *MATCha*-driven miscentering model in these two papers cements *MATCha*'s status as important upstream infrastructure in cosmological analyses which use stacked weak lensing.

Chapter 7

Summary and Future Work

In this thesis, I have outlined my work on and with the *MATCha* pipeline, a powerful tool for large-scale X-ray cluster analysis. I have used *MATCha* to measure L_X and T_X for hundreds of clusters in *redMaPPer* SDSS data, and studied their scaling with richness as well as with each other. I have also studied *redMaPPer* centering with this same dataset. In addition to its use in this SDSS analysis, *MATCha* has proven to be important upstream infrastructure for a number of projects. These projects include Zhang et al. (in prep.)'s study of *redMaPPer* centering in DES Y1, Farahi et al. (in prep.)'s study of X-ray mass proxy scaling with richness in DES Y1 data, Rykoff et al. (2016)'s calibration of *redMaPPer*, Palmese et al. (in prep.)'s calibration of μ_*, Bufanda et al. (2017)'s study of the AGN fraction in galaxy clusters, McClintock et al. (2018)'s study of the mass-richness relation, and Costanzi et al. (in prep.)'s measurement of cosmological parameters with clusters.

Throughout *MATCha*'s future, a number of small improvements are likely to be made to the pipeline in order to facilitate further cosmological studies. We briefly discuss a number of currently-planned upgrades to *MATCha* below and then outline *MATCha*'s planned future use.

7.1 Future upgrades to *MATCha*

As suggested in section 3.4, it is possible improve *MATCha*'s ability to find an L_X value when no T_X can be fit via an iterative algorithm. In this algorithm, an initial T_X is assumed, an L_X is calculated, an L_X-T_X relation is employed to estimate a new T_X, and the algorithm is iterated until convergence. At present, this algorithm is integrated into *MATCha* and is ready for testing. Lena Eiger (an undergraduate student) has performed most of the programming here with my guidance.

Another improvement would be to center our core-cropped r_{500} regions on the X-ray peak instead of the r_{500} centroid. This helps avoid problems when the centroid is offset from the cluster core, e.g. in the case shown in Figure 7.1. As with iterative L_X calculation, the algorithm for this has been implemented in *MATCha* by Lena Eiger (with the guidance of myself and Professor Tesla Jeltema), and is currently ready for testing.

MATCha has some minor usability improvements that could be made as well. The largest among these is that *MATCha* is designed to work with *redMaPPer* catalogs, but there is no fundamental reason for this restriction. Given the modular nature of *MATCha*, it should be relatively straightforward to generalize it to use data from any cluster catalog that includes a redshift estimate, with the input format of that cluster finder described in a configuration file. However, work here has not yet begun.

Additionally, discussion with the team behind the Lloyd-Davies et al. (2011) *XMM* pipeline has revealed that we do not calculate L_X upper limits in the same way. Thus collaborating with them and standardizing an algorithm for both pipelines would be useful in cross-pipeline papers such as Farahi et al. (in prep.).

Finally, an ultimate goal of the *MATCha* project is to release the source code

Figure 7.1: Motivation for *MATCha* Core-Cropping Improvement

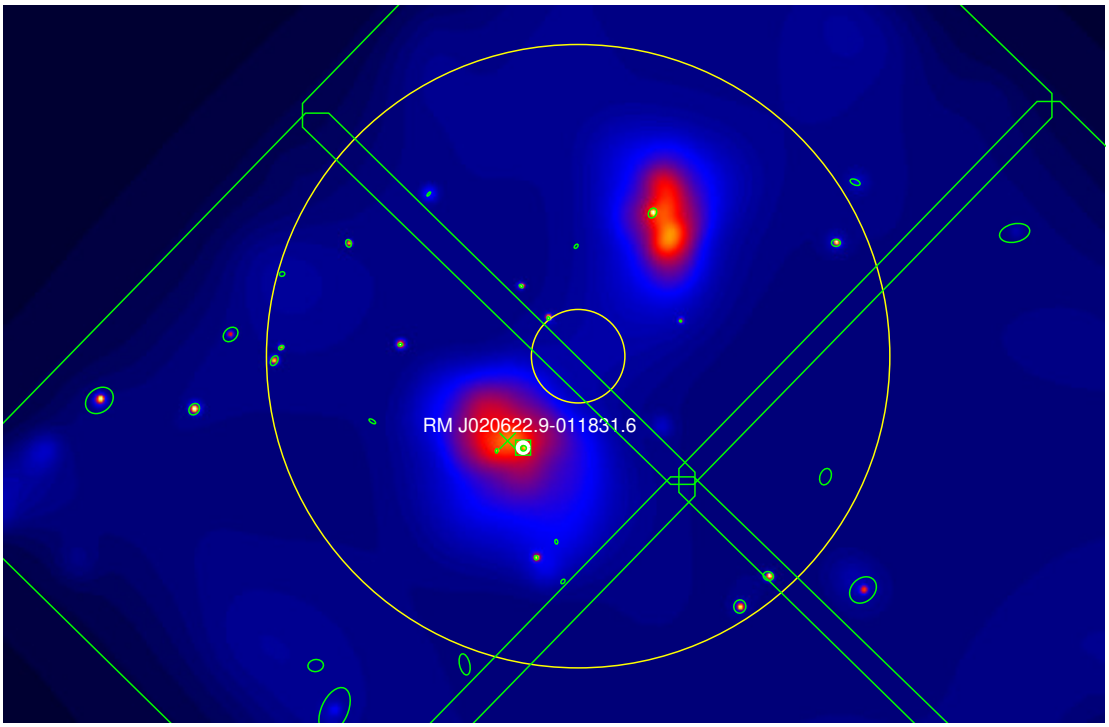

RM J020622.9−011831.6 (mem_match_id 1382, $z = 0.19$), ObsID 16229, ACIS-I detector. This is the cluster shown in Figure 3.6 (b). Here, the core-cropping by *MATCha* has not cut out a core, but has instead removed a low-cluster-emission region of space. Centering at the r_{500} X-ray peak would help fix this issue, although in this case perhaps a second core excision would be required as well. This image obeys the coloring conventions described in the caption for Figure 3.1, with the exception that the 500 kpc and r_{2500} radii are not shown, and r_{500} is shown as an annular region with the core cut out.

publicly. The project has been developed with git and is currently hosted in a private GitHub repository, so a public release would theoretically be as simple as switching the repository from "private" to "public". The main work that needs to be done before public release is an improvement of the installation process and the documentation.

Together, these upgrades should allow for more widespread and improved use of *MATCha* throughout the astrophysics community.

7.2 Further work with DES and LSST

MATCha is currently in use in the analysis of DES Year 3 data. This will likely lead to more analysis similar to that presented in Chapters 4–5, but with the much larger DES Year 3 data set. *MATCha* is also involved in validation of each iteration of *redMaPPer* (currently v. 6.4.22+1). *MATCha* has already found bugs in *redMaPPer* centering, so this validation is extremely valuable to the *redMaPPer* team.

In the coming years, *MATCha*'s use is planned to extend at least through the end of the Dark Energy Survey, with the last planned release being the analysis of DES Year 5 data. As the use of *redMaPPer* will likely extend into the **L**arge **S**ynoptic **S**ky **T**elescope (**LSST**), the use of *MATCha* likely will as well. Thus *MATCha* is likely to be useful in cosmological analyses for many years to come.

Bibliography

T. M. C. Abbott, F. B. Abdalla, S. Allam, A. Amara, J. Annis, J. Asorey, S. Avila, O. Ballester, M. Banerji, W. Barkhouse, L. Baruah, M. Baumer, K. Bechtol, M. R. Becker, A. Benoit-Lévy, G. M. Bernstein, E. Bertin, J. Blazek, S. Bocquet, D. Brooks, D. Brout, E. Buckley-Geer, D. L. Burke, V. Busti, R. Campisano, L. Cardiel-Sas, A. C arnero Rosell, M. Carrasco Kind, J. Carretero, F. J. Castander, R. Cawthon, C. Chang, C. Conselice, G. Costa, M. Crocce, C. E. Cunha, C. B. D'Andrea, L. N. da Costa, R. Das, G. Daues, T. M. Davis, C. Davis, J. De Vicente, D. L. DePoy, J. DeRose, S. Desai, H. T. Diehl, J. P. Dietrich, S. Dodelson, P. Doel, A. Drlica-Wagner, T. F. Eifler, A. E. Elliott, A. E. Evrard, A. Farahi, A. Fausti Neto, E. Fernandez, D. A. Finley, M. Fitzpatrick, B. Flaugher, R. J. Foley, P. Fosalba, D. N. Friedel, J. Frieman, J. García-Bellido, E. Gaz tanaga, D. W. Gerdes, T. Giannantonio, M. S. S. Gill, K. Glazebrook, D. A. Goldstein, M. Gower, D. Gruen, R. A. Gruendl, J. Gschwend, R. R. Gupta, G. Gutierrez, S. Hamilton, W. G. Hartley, S. R. Hinton, J. M. Hislop, D. Hollowood, K. Honscheid, B. Hoyle, D. Huterer, B. Jain, D. J. James, T. Jeltema, M. W. G. Johnson, M. D. Johnson, S. Juneau, T. Kacpr zak, S. Kent, G. Khullar, M. Klein, A. Kovacs, A. M. G. Koziol, E. Krause, A. Kremin, R. Kron, K. Kuehn, S. Kuhlmann, N. Kuropatkin, O. Lahav, J. Lasker, T. S. Li, R. T. Li, A. R. Liddle, M. Lima, H. Lin, P. López-Reyes, N. MacCrann, M. A. G. Maia, J. D. Maloney, M. Manera, M. March, J. Marriner, J. L. Marshall, P. Martini, T. McClintock, T. McKay, R. G. McMahon, P. Melchior, F. Menanteau, C. J. Miller, R. Miquel, J. J. Mohr, E. Morganson, J. Mould, E. Neilsen, R. C. Nichol, D. Nidever, R. Nikutta, F. Nogueira, B. Nord, P. Nugent, L. Nunes, R. L. C. Ogando, L. Old, K. Olsen, A. B. Pace, A. Palmese, F. Paz-Chinchón, H. V. Peiris, W. J. Percival, D. Petravick, A. A. Plazas, J. Poh, C. Pond, A. Por redon, A. Pujol, A. Refregier, K. Reil, P. M. Ricker, R. P. Rollins, A. K. Romer, A. Roodman, P. Rooney, A. J. Ross, E. S. Rykoff, M. Sako, E. Sanchez, M. L. Sanchez, B. Santiago, A. Saro, V. Scarpine, D. Scolnic, A. Scott, S. Serrano, I. Sevilla-Noarbe, E. Sheldon, N. Shipp, M. L. Silveira, R. C. Smith, J. A. Smith, M. Smith, M. Soares-Santos, F. Sobre ira, J. Song, A. Stebbins, E. Suchyta, M. Sullivan, M. E. C. Swanson, G. Tarle, J. Thaler, D. Thomas, R. C. Thomas, M. A. Troxel, D. L. Tucker, V. Vikram, A. K. Vivas, A. R. Wal ker, R. H. Wechsler, J. Weller, W. Wester, R. C. Wolf, H. Wu, B. Yanny, A. Zenteno, Y. Zhang,

and J. Zuntz. The Dark Energy Survey Data Release 1. *ArXiv e-prints*, January 2018. URL http://adsabs.harvard.edu/abs/2018arXiv180103181A.

S. W. Allen, R. W. Schmidt, A. C. Fabian, and H. Ebeling. Cosmological constraints from the local X-ray luminosity function of the most X-ray-luminous galaxy clusters. *MNRAS*, 342:287–298, June 2003. doi: 10.1046/j.1365-8711.2003.06550.x. URL http://adsabs.harvard.edu/abs/2003MNRAS.342..287A.

S. W. Allen, A. E. Evrard, and A. B. Mantz. Cosmological Parameters from Observations of Galaxy Clusters. *ARA&A*, 49:409–470, September 2011. doi: 10.1146/annurev-astro-081710-102514. URL http://adsabs.harvard.edu/abs/2011ARA%26A..49..409A.

E. Anders and N. Grevesse. Abundances of the elements - Meteoritic and solar. *GeoCoA*, 53:197–214, January 1989. doi: 10.1016/0016-7037(89)90286-X. URL http://adsabs.harvard.edu/abs/1989GeCoA..53..197A.

K. A. Arnaud. XSPEC: The First Ten Years. In G. H. Jacoby and J. Barnes, editors, *Astronomical Data Analysis Software and Systems V*, volume 101 of *Astronomical Society of the Pacific Conference Series*, page 17, 1996. URL http://adsabs.harvard.edu/abs/1996ASPC..101...17A.

M. Arnaud, E. Pointecouteau, and G. W. Pratt. The structural and scaling properties of nearby galaxy clusters. II. The M-T relation. *A&A*, 441:893–903, October 2005. doi: 10.1051/0004-6361:20052856. URL http://adsabs.harvard.edu/abs/2005A%26A...441..893A.

N. A. Bahcall. Clusters of galaxies. *ARA&A*, 15:505–540, 1977. doi: 10.1146/annurev.aa.15.090177.002445. URL http://adsabs.harvard.edu/abs/1977ARA%26A..15..505B.

N. A. Bahcall and R. M. Soneira. The spatial correlation function of rich clusters of galaxies. *ApJ*, 270:20–38, July 1983. doi: 10.1086/161094. URL http://adsabs.harvard.edu/abs/1983ApJ...270...20B.

E. F. Bell, C. Wolf, K. Meisenheimer, H.-W. Rix, A. Borch, S. Dye, M. Kleinheinrich, L. Wisotzki, and D. H. McIntosh. Nearly 5000 Distant Early-Type Galaxies in COMBO-17: A Red Sequence and Its Evolution since z˜1. *ApJ*, 608:752–767, June 2004. doi: 10.1086/420778. URL http://adsabs.harvard.edu/abs/2004ApJ...608..752B.

H. Böhringer and N. Werner. X-ray spectroscopy of galaxy clusters: studying astrophysical processes in the largest celestial laboratories. *A&A Rv*, 18:127–196, February 2010. doi: 10.1007/s00159-009-0023-3. URL http://adsabs.harvard.edu/abs/2010A%26ARv..18..127B.

Stefano Borgani, Piero Rosati, Paolo Tozzi, S. A. Stanford, Peter R. Eisenhardt, Chris Lidman, Bradford Holden, Roberto Della Ceca, Colin Norman, and Gordon Squires. Measuring Ω_m with the ROSAT Deep Cluster Survey. *ApJ*, 561:13–21, November 2001. doi: 10.1086/323214. URL https://ui.adsabs.harvard.edu/#abs/2001ApJ...561...13B.

E. Bufanda, D. Hollowood, T. E. Jeltema, E. S. Rykoff, E. Rozo, P. Martini, T. M. C. Abbott, F. B. Abdalla, S. Allam, M. Banerji, A. Benoit-Lévy, E. Bertin, D. Brooks, A. Carnero Rosell, M. Carrasco Kind, J. Carretero, C. E. Cunha, L. N. da Costa, S. Desai, H. T. Diehl, J. P. Dietrich, A. E. Evrard, A. Fausti Neto, B. Flaugher, J. Frieman, D. W. Gerdes, D. A. Goldstein, D. Gruen, R. A. Gruendl, G. Gutierrez, K. Honscheid, D. J. James, K. Kuehn, N. Kuropatkin, M. Lima, M. A. G. Maia, J. L. Marshall, P. Melchior, R. Miquel, J. J. Mohr, R. Ogando, A. A. Plazas, A. K. Romer, P. Rooney, E. Sanchez, B. Santiago, V. Scarpine, I. Sevilla-Noarbe, R. C. Smith, M. Soares-Santos, F. Sobreira, E. Suchyta, G. Tarle, D. Thomas, D. L. Tucker, A. R. Walker, and DES Collaboration. The evolution of active galactic nuclei in clusters of galaxies from the Dark Energy Survey. *MNRAS*, 465:2531–2539, March 2017. doi: 10.1093/mnras/stw2824. URL https://ui.adsabs.harvard.edu/#abs/2017MNRAS.465.2531B.

Kenneth W. Cavagnolo, Megan Donahue, G. Mark Voit, and Ming Sun. Intracluster Medium Entropy Profiles for a Chandra Archival Sample of Galaxy Clusters. *The Astrophysical Journal Supplement Series*, 182:12–32, May 2009. doi: 10.1088/0067-0049/182/1/12. URL https://ui.adsabs.harvard.edu/#abs/2009ApJS..182...12C.

Chandra X-ray Center. The Chandra Proposers' Observatory Guide, 2017. URL http://cxc.harvard.edu/proposer/POG/html/index.html.

Timothy Clifton, Pedro G. Ferreira, Antonio Padilla, and Constantinos Skordis. Modified gravity and cosmology. *PhR*, 513:1–189, March 2012. doi: 10.1016/j.physrep.2012.01.001. URL https://ui.adsabs.harvard.edu/#abs/2012PhR...513....1C.

M. Costanzi, E. Rozo, E. S. Rykoff, A. Farahi, T. Jeltema, A. E. Evrard, A. Mantz, D. Gruen, R. Mandelbaum, J. DeRose, T. McClintock, T. N. Varga, Y. Zhang, J. Weller, R. H. Wechsler, and M. Aguena. Modeling projection effects in optically-selected cluster catalogues. *ArXiv e-prints*, art. arXiv:1807.07072, July 2018. URL https://ui.adsabs.harvard.edu/#abs/2018arXiv180707072C.

M. Costanzi et al. Modeling Projection Effects in Optically-Selected Cluster Catalogues. in prep.

C. Cunha, D. Huterer, and J. A. Frieman. Constraining dark energy with clusters: Complementarity with other probes. *PRD*, 80(6):063532, September 2009. doi: 10.1103/PhysRevD.80.063532. URL `http://adsabs.harvard.edu/abs/2009PhRvD..80f3532C`.

Antonaldo Diaferio and Margaret J. Geller. Infall Regions of Galaxy Clusters. *ApJ*, 481:633–643, May 1997. doi: 10.1086/304075. URL `https://ui.adsabs.harvard.edu/#abs/1997ApJ...481..633D`.

J. M. Dickey and F. J. Lockman. H I in the Galaxy. *ARA&A*, 28:215–261, 1990. doi: 10.1146/annurev.aa.28.090190.001243. URL `http://adsabs.harvard.edu/abs/1990ARA%26A..28..215D`.

Jason Eastman, Paul Martini, Gregory Sivakoff, Daniel D. Kelson, John S. Mulchaey, and Kim-Vy Tran. First Measurement of a Rapid Increase in the AGN Fraction in High- Redshift Clusters of Galaxies. *ApJ*, 664:L9–L12, July 2007. doi: 10.1086/520577. URL `https://ui.adsabs.harvard.edu/#abs/2007ApJ...664L...9E`.

Vincent R. Eke, Shaun Cole, Carlos S. Frenk, and J. Patrick Henry. Measuring Omega_0 using cluster evolution. *MNRAS*, 298:1145–1158, August 1998. doi: 10.1046/j.1365-8711.1998.01713.x. URL `https://ui.adsabs.harvard.edu/#abs/1998MNRAS.298.1145E`.

A. Farahi, A. E. Evrard, I. McCarthy, D. J. Barnes, and S. T. Kay. Localized massive halo properties in BAHAMAS and MACSIS simulations: scalings, lognormality, and covariance. *MNRAS*, 478:2618–2632, August 2018. doi: 10.1093/mnras/sty1179. URL `http://adsabs.harvard.edu/abs/2018MNRAS.478.2618F`.

A. Farahi et al. X-ray Observables of redMaPPer Galaxy Clusters in Dark Energy Survey Year-1 Data, With Application in Mass–Richness Intrinsic Scatter. in prep.

J. A. Frieman, M. S. Turner, and D. Huterer. Dark energy and the accelerating universe. *Annual Review of Astronomy and Astrophysics*, 46:385–432, September 2008. doi: 10.1146/annurev.astro.46.060407.145243. URL `https://ui.adsabs.harvard.edu/#abs/2008ARA&A..46..385F`.

A. Fruscione, J. C. McDowell, G. E. Allen, N. S. Brickhouse, D. J. Burke, J. E. Davis, N. Durham, M. Elvis, E. C. Galle, D. E. Harris, D. P. Huenemoerder, J. C. Houck, B. Ishibashi, M. Karovska, F. Nicastro, M. S. Noble, M. A. Nowak, F. A. Primini, A. Siemiginowska, R. K. Smith, and M. Wise. CIAO: Chandra's data analysis system. In *Society of Photo-Optical Instrumentation Engineers (SPIE) Conference Series*, volume 6270 of *Proc. SPIE*, page 62701V, June 2006.

doi: 10.1117/12.671760. URL http://adsabs.harvard.edu/abs/2006SPIE.6270E..1VF.

S. M. Hansen, E. S. Sheldon, R. H. Wechsler, and B. P. Koester. The Galaxy Content of SDSS Clusters and Groups. *ApJ*, 699:1333–1353, July 2009. doi: 10.1088/0004-637X/699/2/1333. URL http://adsabs.harvard.edu/abs/2009ApJ...699.1333H.

J. Patrick Henry. Measuring Cosmological Parameters from the Evolution of Cluster X-Ray Temperatures. *ApJ*, 534:565–580, May 2000. doi: 10.1086/308783. URL https://ui.adsabs.harvard.edu/#abs/2000ApJ...534..565H.

A. K. Hicks, G. W. Pratt, M. Donahue, E. Ellingson, M. Gladders, H. Böhringer, H. K. C. Yee, R. Yan, J. H. Croston, and D. G. Gilbank. The X-ray properties of optically selected clusters of galaxies. *MNRAS*, 431:2542–2553, May 2013. doi: 10.1093/mnras/stt348. URL http://adsabs.harvard.edu/abs/2013MNRAS.431.2542H.

J. A. Hoeting, D. Madigan, A. E. Raftery, and C. T. Volinsky. Bayesian model averaging: a tutorial. *Statist. Sci.*, 14:382–417, 1999.

Devon L. Hollowood, Tesla Jeltema, Xinyi Chen, Arya Farahi, August Evrard, Spencer Everett, Eduardo Rozo, Eli Rykoff, Rebecca Bernstein, Alberto Bermeo, Lena Eiger, Paul Giles, Holger Israel, Renee Michel, Raziq Noorali, Kathy Romer, Philip Rooney, and Megan Splettstoesser. Chandra Follow-Up of the SDSS DR8 redMaPPer Catalog Using the MATCha Pipeline. *ArXiv e-prints*, art. arXiv:1808.06637, August 2018. URL https://ui.adsabs.harvard.edu/#abs/2018arXiv180806637H.

Dragan Huterer and Daniel L. Shafer. Dark energy two decades after: observables, probes, consistency tests. *Reports on Progress in Physics*, 81:016901, January 2018. doi: 10.1088/1361-6633/aa997e. URL https://ui.adsabs.harvard.edu/#abs/2018RPPh...81a6901H.

D. E. Johnston, E. S. Sheldon, R. H. Wechsler, E. Rozo, B. P. Koester, J. A. Frieman, T. A. McKay, A. E. Evrard, M. R. Becker, and J. Annis. Cross-correlation Weak Lensing of SDSS galaxy Clusters II: Cluster Density Profiles and the Mass–Richness Relation. *ArXiv e-prints*, September 2007. URL http://adsabs.harvard.edu/abs/2007arXiv0709.1159J.

A. Joyce, L. Lombriser, and F. Schmidt. Dark Energy Versus Modified Gravity. *Annual Review of Nuclear and Particle Science*, 66:95–122, October 2016. doi: 10.1146/annurev-nucl-102115-044553. URL http://adsabs.harvard.edu/abs/2016ARNPS..66...95J.

P. M. W. Kalberla, W. B. Burton, D. Hartmann, E. M. Arnal, E. Bajaja, R. Morras, and W. G. L. Poeppel. VizieR Online Data Catalog: Leiden/Argentine/Bonn (LAB) Survey of Galactic HI (Kalberla+ 2005). *VizieR Online Data Catalog*, 8076, July 2005. URL `http://adsabs.harvard.edu/abs/2005yCat.8076....0K`.

B. C. Kelly. Some Aspects of Measurement Error in Linear Regression of Astronomical Data. *ApJ*, 665:1489–1506, August 2007. doi: 10.1086/519947. URL `http://adsabs.harvard.edu/abs/2007ApJ...665.1489K`.

B. P. Koester, T. A. McKay, J. Annis, R. H. Wechsler, A. E. Evrard, E. Rozo, L. Bleem, E. S. Sheldon, and D. Johnston. MaxBCG: A Red-Sequence Galaxy Cluster Finder. *ApJ*, 660:221–238, May 2007. doi: 10.1086/512092. URL `http://adsabs.harvard.edu/abs/2007ApJ...660..221K`.

E. Komatsu, K. M. Smith, J. Dunkley, C. L. Bennett, B. Gold, G. Hinshaw, N. Jarosik, D. Larson, M. R. Nolta, L. Page, D. N. Spergel, M. Halpern, R. S. Hill, A. Kogut, M. Limon, S. S. Meyer, N. Odegard, G. S. Tucker, J. L. Weiland, E. Wollack, and E. L. Wright. Seven-year Wilkinson Microwave Anisotropy Probe (WMAP) Observations: Cosmological Interpretation. *ApJS*, 192:18, February 2011. doi: 10.1088/0067-0049/192/2/18. URL `http://adsabs.harvard.edu/abs/2011ApJS..192...18K`.

A. V. Kravtsov, A. Vikhlinin, and D. Nagai. A New Robust Low-Scatter X-Ray Mass Indicator for Clusters of Galaxies. *ApJ*, 650:128–136, October 2006. doi: 10.1086/506319. URL `http://adsabs.harvard.edu/abs/2006ApJ...650..128K`.

R. Laureijs, J. Amiaux, S. Arduini, J. . Augueres, J. Brinchmann, R. Cole, M. Cropper, C. Dabin, L. Duvet, A. Ealet, and et al. Euclid Definition Study Report. *ArXiv e-prints*, October 2011. URL `http://adsabs.harvard.edu/abs/2011arXiv1110.3193L`.

A. Leauthaud, A. Finoguenov, J.-P. Kneib, J. E. Taylor, R. Massey, J. Rhodes, O. Ilbert, K. Bundy, J. Tinker, M. R. George, P. Capak, A. M. Koekemoer, D. E. Johnston, Y.-Y. Zhang, N. Cappelluti, R. S. Ellis, M. Elvis, S. Giodini, C. Heymans, O. Le Fèvre, S. Lilly, H. J. McCracken, Y. Mellier, A. Réfrégier, M. Salvato, N. Scoville, G. Smoot, M. Tanaka, L. Van Waerbeke, and M. Wolk. A Weak Lensing Study of X-ray Groups in the Cosmos Survey: Form and Evolution of the Mass-Luminosity Relation. *ApJ*, 709:97–114, January 2010. doi: 10.1088/0004-637X/709/1/97. URL `http://adsabs.harvard.edu/abs/2010ApJ...709...97L`.

E. J. Lloyd-Davies, A. K. Romer, N. Mehrtens, M. Hosmer, M. Davidson, K. Sabirli, R. G. Mann, M. Hilton, A. R. Liddle, P. T. P. Viana, H. C. Camp-

bell, C. A. Collins, E. N. Dubois, P. Freeman, C. D. Harrison, B. Hoyle, S. T. Kay, E. Kuwertz, C. J. Miller, R. C. Nichol, M. Sahlén, S. A. Stanford, and J. P. Stott. The XMM Cluster Survey: X-ray analysis methodology. *MNRAS*, 418:14–53, November 2011. doi: 10.1111/j.1365-2966.2011.19117.x. URL http://adsabs.harvard.edu/abs/2011MNRAS.418...14L.

LSST Dark Energy Science Collaboration. Large Synoptic Survey Telescope: Dark Energy Science Collaboration. *ArXiv e-prints*, November 2012. URL http://adsabs.harvard.edu/abs/2012arXiv1211.0310L.

A. Mahdavi, H. Hoekstra, A. Babul, C. Bildfell, T. Jeltema, and J. P. Henry. Joint Analysis of Cluster Observations. II. Chandra/XMM-Newton X-Ray and Weak Lensing Scaling Relations for a Sample of 50 Rich Clusters of Galaxies. *ApJ*, 767:116, April 2013. doi: 10.1088/0004-637X/767/2/116. URL http://adsabs.harvard.edu/abs/2013ApJ...767..116M.

A. Mantz, S. W. Allen, H. Ebeling, D. Rapetti, and A. Drlica-Wagner. The observed growth of massive galaxy clusters - II. X-ray scaling relations. *MNRAS*, 406:1773–1795, August 2010. doi: 10.1111/j.1365-2966.2010.16993.x. URL https://ui.adsabs.harvard.edu/#abs/2010MNRAS.406.1773M.

A. B. Mantz, S. W. Allen, R. G. Morris, A. von der Linden, D. E. Applegate, P. L. Kelly, D. L. Burke, D. Donovan, and H. Ebeling. Weighing the giants- V. Galaxy cluster scaling relations. *MNRAS*, 463:3582–3603, December 2016. doi: 10.1093/mnras/stw2250. URL http://adsabs.harvard.edu/abs/2016MNRAS.463.3582M.

Paul Martini, Gregory R. Sivakoff, and John S. Mulchaey. The Evolution of Active Galactic Nuclei in Clusters of Galaxies to Redshift 1.3. *ApJ*, 701:66–85, August 2009. doi: 10.1088/0004-637X/701/1/66. URL https://ui.adsabs.harvard.edu/#abs/2009ApJ...701...66M.

Paul Martini, E. D. Miller, M. Brodwin, S. A. Stanford, Anthony H. Gonzalez, M. Bautz, R. C. Hickox, D. Stern, P. R. Eisenhardt, A. Galametz, D. Norman, B. T. Jannuzi, A. Dey, S. Murray, C. Jones, and M. J. I. Brown. The Cluster and Field Galaxy Active Galactic Nucleus Fraction at z = 1-1.5: Evidence for a Reversal of the Local Anticorrelation between Environment and AGN Fraction. *ApJ*, 768:1, May 2013. doi: 10.1088/0004-637X/768/1/1. URL https://ui.adsabs.harvard.edu/#abs/2013ApJ...768....1M.

B. J. Maughan, P. A. Giles, S. W. Randall, C. Jones, and W. R. Forman. Self-similar scaling and evolution in the galaxy cluster X-ray luminosity-temperature relation. *MNRAS*, 421:1583–1602, April 2012. doi: 10.1111/j.1365-2966.2012.20419.x. URL http://adsabs.harvard.edu/abs/2012MNRAS.421.1583M.

T. McClintock, T. N. Varga, D. Gruen, E. Rozo, E. S. Rykoff, T. Shin, P. Melchior, J. DeRose, S. Seitz, J. P. Dietrich, E. Sheldon, Y. Zhang, A. von der Linden, T. Jeltema, A. Mantz, A. K. Romer, S. Allen, M. R. Becker, A. Bermeo, S. Bhargava, M. Costanzi, S. Everett, A. Farahi, N. Hamaus, W. G. Hartley, D. L. Hollowood, B. Hoyle, H. Israel, P. Li, N. MacCrann, G. Morris, A. Palmese, A. A. Plazas, G. Pollina, M. M. Rau, M. Simet, M. Soares-Santos, M. A. Troxel, C. Vergara Cervantes, R. H. Wechsler, J. Zuntz, T. M. C. Abbott, F. B. Abdalla, S. Allam, J. Annis, S. Avila, S. L. Bridle, D. Brooks, D. L. Burke, A. Carnero Rosell, M. Carrasco Kind, J. Carretero, F. J. Castander, M. Crocce, C. E. Cunha, C. B. D'Andrea, L. N. da Costa, C. Davis, J. De Vicente, H. T. Diehl, P. Doel, A. Drlica-Wagner, A. E. Evrard, B. Flaugher, P. Fosalba, J. Frieman, J. García-Bellido, E. Gaztanaga, D. W. Gerdes, T. Giannantonio, R. A. Gruendl, G. Gutierrez, K. Honscheid, D. J. James, D. Kirk, E. Krause, K. Kuehn, O. Lahav, T. S. Li, M. Lima, M. March, J. L. Marshall, F. Menanteau, R. Miquel, J. J. Mohr, B. Nord, R. L. C. Ogando, A. Roodman, E. Sanchez, V. Scarpine, R. Schindler, I. Sevilla-Noarbe, M. Smith, R. C. Smith, F. Sobreira, E. Suchyta, M. E. C. Swanson, G. Tarle, D. L. Tucker, V. Vikram, A. R. Walker, and J. Weller. Dark Energy Survey Year 1 Results: Weak Lensing Mass Calibration of redMaPPer Galaxy Clusters. *ArXiv e-prints*, art. arXiv:1805.00039, April 2018. URL `https://ui.adsabs.harvard.edu/#abs/2018arXiv180500039M`.

P. Melchior, D. Gruen, T. McClintock, T. N. Varga, E. Sheldon, E. Rozo, A. Amara, M. R. Becker, B. A. Benson, A. Bermeo, S. L. Bridle, J. Clampitt, J. P. Dietrich, W. G. Hartley, D. Hollowood, B. Jain, M. Jarvis, T. Jeltema, T. Kacprzak, N. MacCrann, E. S. Rykoff, A. Saro, E. Suchyta, M. A. Troxel, J. Zuntz, C. Bonnett, A. A. Plazas, T. M. C. Abbott, F. B. Abdalla, J. Annis, A. Benoit-Lévy, G. M. Bernstein, E. Bertin, D. Brooks, E. Buckley-Geer, A. Carnero Rosell, M. Carrasco Kind, J. Carretero, C. E. Cunha, C. B. D'Andrea, L. N. da Costa, S. Desai, T. F. Eifler, B. Flaugher, P. Fosalba, J. García-Bellido, E. Gaztanaga, D. W. Gerdes, R. A. Gruendl, J. Gschwend, G. Gutierrez, K. Honscheid, D. J. James, D. Kirk, E. Krause, K. Kuehn, N. Kuropatkin, O. Lahav, M. Lima, M. A. G. Maia, M. March, P. Martini, F. Menanteau, C. J. Miller, R. Miquel, J. J. Mohr, R. C. Nichol, R. Ogando, A. K. Romer, E. Sanchez, V. Scarpine, I. Sevilla-Noarbe, R. C. Smith, M. Soares-Santos, F. Sobreira, M. E. C. Swanson, G. Tarle, D. Thomas, A. R. Walker, J. Weller, and Y. Zhang. Weak-lensing mass calibration of redMaPPer galaxy clusters in Dark Energy Survey Science Verification data. *MNRAS*, 469:4899–4920, August 2017. doi: 10.1093/mnras/stx1053. URL `http://adsabs.harvard.edu/abs/2017MNRAS.469.4899M`.

S. Miyazaki, Y. Komiyama, H. Nakaya, Y. Kamata, Y. Doi, T. Hamana, H. Karoji, H. Furusawa, S. Kawanomoto, T. Morokuma, Y. Ishizuka, K. Nariai, Y. Tanaka,

F. Uraguchi, Y. Utsumi, Y. Obuchi, Y. Okura, M. Oguri, T. Takata, D. Tomono, T. Kurakami, K. Namikawa, T. Usuda, H. Yamanoi, T. Terai, H. Uekiyo, Y. Yamada, M. Koike, H. Aihara, Y. Fujimori, S. Mineo, H. Miyatake, N. Yasuda, J. Nishizawa, T. Saito, M. Tanaka, T. Uchida, N. Katayama, S.-Y. Wang, H.-Y. Chen, R. Lupton, C. Loomis, S. Bickerton, P. Price, J. Gunn, H. Suzuki, Y. Miyazaki, M. Muramatsu, K. Yamamoto, M. Endo, Y. Ezaki, N. Itoh, Y. Miwa, H. Yokota, T. Matsuda, R. Ebinuma, and K. Takeshi. Hyper Suprime-Cam. In *Ground-based and Airborne Instrumentation for Astronomy IV*, volume 8446 of *Proc. SPIE*, page 84460Z, September 2012. doi: 10.1117/12.926844. URL `http://adsabs.harvard.edu/abs/2012SPIE.8446E..0ZM`.

J. Nevalainen, L. David, and M. Guainazzi. Cross-calibrating X-ray detectors with clusters of galaxies: an IACHEC study. *A&A*, 523:A22, November 2010. doi: 10.1051/0004-6361/201015176. URL `http://adsabs.harvard.edu/abs/2010A%26A...523A..22N`.

M. Oguri and M. Takada. Combining cluster observables and stacked weak lensing to probe dark energy: Self-calibration of systematic uncertainties. *PRD*, 83 (2):023008, January 2011. doi: 10.1103/PhysRevD.83.023008. URL `http://adsabs.harvard.edu/abs/2011PhRvD..83b3008O`.

P. Padovani, D. M. Alexander, R. J. Assef, B. De Marco, P. Giommi, R. C. Hickox, G. T. Richards, V. Smolčić, E. Hatziminaoglou, V. Mainieri, and M. Salvato. Active galactic nuclei: what's in a name? *A&A Rv*, 25:2, August 2017. doi: 10.1007/s00159-017-0102-9. URL `http://adsabs.harvard.edu/abs/2017A%26ARv..25....2P`.

A. Palmese, Annis J., J. C. Burgad, H. Lin, M. E. S. Pereira, M. Soares-Santos, B. Welch, A. Farahi, S. Bermeo, A. Bhargava, J. DeMastri, J. DeRose, D. Gruen, P. Giles, W. Hartley, D. L. Hollowood, B. Lahav, O. Leistedt, T. Jeltema, T. McClintock, P. Melchior, E. Romer, A. K. Rozo, E. S. Rykoff, T. N. Varga, R. H. Wechsler, Y. Zhang, et al. Stellar mass as a Galaxy Cluster Mass Proxy and Stellar-to-Halo Connection in the Dark Energy Survey redMaPPer Clusters. in prep.

S. Perlmutter, G. Aldering, G. Goldhaber, R. A. Knop, P. Nugent, P. G. Castro, S. Deustua, S. Fabbro, A. Goobar, D. E. Groom, I. M. Hook, A. G. Kim, M. Y. Kim, J. C. Lee, N. J. Nunes, R. Pain, C. R. Pennypacker, R. Quimby, C. Lidman, R. S. Ellis, M. Irwin, R. G. McMahon, P. Ruiz-Lapuente, N. Walton, B. Schaefer, B. J. Boyle, A. V. Filippenko, T. Matheson, A. S. Fruchter, N. Panagia, H. J. M. Newberg, W. J. Couch, and The Supernova Cosmology Project. Measurements of Ω and Λ from 42 High-Redshift Supernovae. *ApJ*, 517:565–586, June 1999. doi: 10.1086/307221. URL `https://ui.adsabs.harvard.edu/#abs/1999ApJ...517..565P`.

Planck Collaboration, P. A. R. Ade, N. Aghanim, M. Arnaud, M. Ashdown, J. Aumont, C. Baccigalupi, A. J. Banday, R. B. Barreiro, N. Bartolo, and et al. Planck 2015 results. XIV. Dark energy and modified gravity. *A&A*, 594:A14, September 2016. doi: 10.1051/0004-6361/201525814. URL `http://adsabs.harvard.edu/abs/2016A%26A...594A..14P`.

Planck Collaboration, N. Aghanim, Y. Akrami, M. Ashdown, J. Aumont, C. Baccigalupi, M. Ballardini, A. J. Banday, R. B. Barreiro, N. Bartolo, S. Basak, R. Battye, K. Benabed, J.-P. Bernard, M. Bersanelli, P. Bielewicz, J. J. Bock, J. R. Bond, J. Borrill, F. R. Bouchet, F. Boulanger, M. Bucher, C. Burigana, R. C. Butler, E. Calabrese, J.-F. Cardoso, J. Carron, A. Challinor, H. C. Chiang, J. Chluba, L. P. L. Colombo, C. Combet, D. Contreras, B. P. Crill, F. Cuttaia, P. de Bernardis, G. de Zotti, J. Delabrouille, J.-M. Delouis, E. Di Valentino, J. M. Diego, O. Doré, M. Douspis, A. Ducout, X. Dupac, S. Dusini, G. Efstathiou, F. Elsner, T. A. Enßlin, H. K. Eriksen, Y. Fantaye, M. Farhang, J. Fergusson, R. Fernandez-Cobos, F. Finelli, F. Forastieri, M. Frailis, E. Franceschi, A. Frolov, S. Galeotta, S. Galli, K. Ganga, R. T. Génova-Santos, M. Gerbino, T. Ghosh, J. González-Nuevo, K. M. Górski, S. Gratton, A. Gruppuso, J. E. Gudmundsson, J. Hamann, W. Handley, D. Herranz, E. Hivon, Z. Huang, A. H. Jaffe, W. C. Jones, A. Karakci, E. Keihänen, R. Keskitalo, K. Kiiveri, J. Kim, T. S. Kisner, L. Knox, N. Krachmalnicoff, M. Kunz, H. Kurki-Suonio, G. Lagache, J.-M. Lamarre, A. Lasenby, M. Lattanzi, C. R. Lawrence, M. Le Jeune, P. Lemos, J. Lesgourgues, F. Levrier, A. Lewis, M. Liguori, P. B. Lilje, M. Lilley, V. Lindholm, M. López-Caniego, P. M. Lubin, Y.-Z. Ma, J. F. Macías-Pérez, G. Maggio, D. Maino, N. Mandolesi, A. Mangilli, A. Marcos-Caballero, M. Maris, P. G. Martin, M. Martinelli, E. Martínez-González, S. Matarrese, N. Mauri, J. D. McEwen, P. R. Meinhold, A. Melchiorri, A. Mennella, M. Migliaccio, M. Millea, S. Mitra, M.-A. Miville-Deschênes, D. Molinari, L. Montier, G. Morgante, A. Moss, P. Natoli, H. U. Nørgaard-Nielsen, L. Pagano, D. Paoletti, B. Partridge, G. Patanchon, H. V. Peiris, F. Perrotta, V. Pettorino, F. Piacentini, L. Polastri, G. Polenta, J.-L. Puget, J. P. Rachen, M. Reinecke, M. Remazeilles, A. Renzi, G. Rocha, C. Rosset, G. Roudier, J. A. Rubiño-Martín, B. Ruiz-Granados, L. Salvati, M. Sandri, M. Savelainen, D. Scott, E. P. S. Shellard, C. Sirignano, G. Sirri, L. D. Spencer, R. Sunyaev, A.-S. Suur-Uski, J. A. Tauber, D. Tavagnacco, M. Tenti, L. Toffolatti, M. Tomasi, T. Trombetti, L. Valenziano, J. Valiviita, B. Van Tent, L. Vibert, P. Vielva, F. Villa, N. Vittorio, B. D. Wandelt, I. K. Wehus, M. White, S. D. M. White, A. Zacchei, and A. Zonca. Planck 2018 results. VI. Cosmological parameters. *ArXiv e-prints*, July 2018. URL `http://adsabs.harvard.edu/abs/2018arXiv180706209P`.

R. Reyes, R. Mandelbaum, J. E. Gunn, R. Nakajima, U. Seljak, and C. M. Hirata. Optical-to-virial velocity ratios of local disc galaxies from combined kinematics and galaxy-galaxy lensing. *MNRAS*, 425:2610–2640, October 2012.

doi: 10.1111/j.1365-2966.2012.21472.x. URL https://ui.adsabs.harvard.edu/#abs/2012MNRAS.425.2610R.

Adam G. Riess, Alexei V. Filippenko, Peter Challis, Alejandro Clocchiatti, Alan Diercks, Peter M. Garnavich, Ron L. Gilliland, Craig J. Hogan, Saurabh Jha, Robert P. Kirshner, B. Leibundgut, M. M. Phillips, David Reiss, Brian P. Schmidt, Robert A. Schommer, R. Chris Smith, J. Spyromilio, Christopher Stubbs, Nicholas B. Suntzeff, and John Tonry. Observational Evidence from Supernovae for an Accelerating Universe and a Cosmological Constant. *AJ*, 116: 1009–1038, September 1998. doi: 10.1086/300499. URL https://ui.adsabs.harvard.edu/#abs/1998AJ....116.1009R.

G. E. Romero, M. Boettcher, S. Markoff, and F. Tavecchio. Relativistic Jets in Active Galactic Nuclei and Microquasars. *SSRv*, 207:5–61, July 2017. doi: 10.1007/s11214-016-0328-2. URL http://adsabs.harvard.edu/abs/2017SSRv..207....5R.

E. Rozo and E. S. Rykoff. redMaPPer II: X-Ray and SZ Performance Benchmarks for the SDSS Catalog. *ApJ*, 783:80, March 2014. doi: 10.1088/0004-637X/783/2/80. URL http://adsabs.harvard.edu/abs/2014ApJ...783...80R.

E. Rozo, E. S. Rykoff, J. G. Bartlett, and J.-B. Melin. redMaPPer - III. A detailed comparison of the Planck 2013 and SDSS DR8 redMaPPer cluster catalogues. *MNRAS*, 450:592–605, June 2015a. doi: 10.1093/mnras/stv605. URL http://adsabs.harvard.edu/abs/2015MNRAS.450..592R.

E. Rozo, E. S. Rykoff, M. Becker, R. M. Reddick, and R. H. Wechsler. redMaPPer - IV. Photometric membership identification of red cluster galaxies with 1 per cent precision. *MNRAS*, 453:38–52, October 2015b. doi: 10.1093/mnras/stv1560. URL http://adsabs.harvard.edu/abs/2015MNRAS.453...38R.

Eduardo Rozo, Eli S. Rykoff, Benjamin P. Koester, Timothy McKay, Jiangang Hao, August Evrard, Risa H. Wechsler, Sarah Hansen, Erin Sheldon, David Johnston, Matthew Becker, James Annis, Lindsey Bleem, and Ryan Scranton. Improvement of the Richness Estimates of maxBCG Clusters. *ApJ*, 703:601–613, September 2009. doi: 10.1088/0004-637X/703/1/601. URL https://ui.adsabs.harvard.edu/#abs/2009ApJ...703..601R.

E. S. Rykoff, B. P. Koester, E. Rozo, J. Annis, A. E. Evrard, S. M. Hansen, J. Hao, D. E. Johnston, T. A. McKay, and R. H. Wechsler. Robust Optical Richness Estimation with Reduced Scatter. *ApJ*, 746:178, February 2012. doi: 10.1088/0004-637X/746/2/178. URL http://adsabs.harvard.edu/abs/2012ApJ...746..178R.

E. S. Rykoff, E. Rozo, M. T. Busha, C. E. Cunha, A. Finoguenov, A. Evrard, J. Hao, B. P. Koester, A. Leauthaud, B. Nord, M. Pierre, R. Reddick, T. Sadibekova, E. S. Sheldon, and R. H. Wechsler. redMaPPer. I. Algorithm and SDSS DR8 Catalog. *ApJ*, 785:104, April 2014. doi: 10.1088/0004-637X/785/2/104. URL `http://adsabs.harvard.edu/abs/2014ApJ...785..104R`.

E. S. Rykoff, E. Rozo, D. Hollowood, A. Bermeo-Hernandez, T. Jeltema, J. Mayers, A. K. Romer, P. Rooney, A. Saro, C. Vergara Cervantes, R. H. Wechsler, H. Wilcox, T. M. C. Abbott, F. B. Abdalla, S. Allam, J. Annis, A. Benoit-Lévy, G. M. Bernstein, E. Bertin, D. Brooks, D. L. Burke, D. Capozzi, A. Carnero Rosell, M. Carrasco Kind, F. J. Castander, M. Childress, C. A. Collins, C. E. Cunha, C. B. D'Andrea, L. N. da Costa, T. M. Davis, S. Desai, H. T. Diehl, J. P. Dietrich, P. Doel, A. E. Evrard, D. A. Finley, B. Flaugher, P. Fosalba, J. Frieman, K. Glazebrook, D. A. Goldstein, D. Gruen, R. A. Gruendl, G. Gutierrez, M. Hilton, K. Honscheid, B. Hoyle, D. J. James, S. T. Kay, K. Kuehn, N. Kuropatkin, O. Lahav, G. F. Lewis, C. Lidman, M. Lima, M. A. G. Maia, R. G. Mann, J. L. Marshall, P. Martini, P. Melchior, C. J. Miller, R. Miquel, J. J. Mohr, R. C. Nichol, B. Nord, R. Ogando, A. A. Plazas, K. Reil, M. Sahlén, E. Sanchez, B. Santiago, V. Scarpine, M. Schubnell, I. Sevilla-Noarbe, R. C. Smith, M. Soares-Santos, F. Sobreira, J. P. Stott, E. Suchyta, M. E. C. Swanson, G. Tarle, D. Thomas, D. Tucker, S. Uddin, P. T. P. Viana, V. Vikram, A. R. Walker, Y. Zhang, and DES Collaboration. The RedMaPPer Galaxy Cluster Catalog From DES Science Verification Data. *ApJS*, 224:1, May 2016. doi: 10.3847/0067-0049/224/1/1. URL `http://adsabs.harvard.edu/abs/2016ApJS..224....1R`.

E. Sánchez and DES Collaboration. The Dark Energy Survey. In *Journal of Physics Conference Series*, volume 259 of *Journal of Physics Conference Series*, page 012080, November 2010. doi: 10.1088/1742-6596/259/1/012080. URL `http://adsabs.harvard.edu/abs/2010JPhCS.259a2080S`.

A. Saro, S. Bocquet, E. Rozo, B. A. Benson, J. Mohr, E. S. Rykoff, M. Soares-Santos, L. Bleem, S. Dodelson, P. Melchior, F. Sobreira, V. Upadhyay, J. Weller, T. Abbott, F. B. Abdalla, S. Allam, R. Armstrong, M. Banerji, A. H. Bauer, M. Bayliss, A. Benoit-Lévy, G. M. Bernstein, E. Bertin, M. Brodwin, D. Brooks, E. Buckley-Geer, D. L. Burke, J. E. Carlstrom, R. Capasso, D. Capozzi, A. Carnero Rosell, M. Carrasco Kind, I. Chiu, R. Covarrubias, T. M. Crawford, M. Crocce, C. B. D'Andrea, L. N. da Costa, D. L. DePoy, S. Desai, T. de Haan, H. T. Diehl, J. P. Dietrich, P. Doel, C. E. Cunha, T. F. Eifler, A. E. Evrard, A. Fausti Neto, E. Fernandez, B. Flaugher, P. Fosalba, J. Frieman, C. Gangkofner, E. Gaztanaga, D. Gerdes, D. Gruen, R. A. Gruendl, N. Gupta, C. Hennig, W. L. Holzapfel, K. Honscheid, B. Jain, D. James, K. Kuehn, N. Kuropatkin, O. Lahav, T. S. Li, H. Lin, M. A. G. Maia, M. March,

J. L. Marshall, Paul Martini, M. McDonald, C. J. Miller, R. Miquel, B. Nord, R. Ogando, A. A. Plazas, C. L. Reichardt, A. K. Romer, A. Roodman, M. Sako, E. Sanchez, M. Schubnell, I. Sevilla, R. C. Smith, B. Stalder, A. A. Stark, V. Strazzullo, E. Suchyta, M. E. C. Swanson, G. Tarle, J. Thaler, D. Thomas, D. Tucker, V. Vikram, A. von der Linden, A. R. Walker, R. H. Wechsler, W. Wester, A. Zenteno, and K. E. Ziegler. Constraints on the richness-mass relation and the optical-SZE positional offset distribution for SZE-selected clusters. *MNRAS*, 454:2305–2319, December 2015. doi: 10.1093/mnras/stv2141. URL `https://ui.adsabs.harvard.edu/#abs/2015MNRAS.454.2305S`.

B. Sartoris, A. Biviano, C. Fedeli, J. G. Bartlett, S. Borgani, M. Costanzi, C. Giocoli, L. Moscardini, J. Weller, B. Ascaso, S. Bardelli, S. Maurogordato, and P. T. P. Viana. Next generation cosmology: constraints from the Euclid galaxy cluster survey. *MNRAS*, 459:1764–1780, June 2016. doi: 10.1093/mnras/stw630. URL `http://adsabs.harvard.edu/abs/2016MNRAS.459.1764S`.

G. Schellenberger, T. H. Reiprich, L. Lovisari, J. Nevalainen, and L. David. XMM-Newton and Chandra cross-calibration using HIFLUGCS galaxy clusters . Systematic temperature differences and cosmological impact. *A&A*, 575: A30, March 2015. doi: 10.1051/0004-6361/201424085. URL `http://adsabs.harvard.edu/abs/2015A%26A...575A..30S`.

M. Simet, T. McClintock, R. Mandelbaum, E. Rozo, E. Rykoff, E. Sheldon, and R. H. Wechsler. Weak lensing measurement of the mass-richness relation of SDSS redMaPPer clusters. *MNRAS*, 466:3103–3118, April 2017. doi: 10.1093/mnras/stw3250. URL `http://adsabs.harvard.edu/abs/2017MNRAS.466.3103S`.

S. Smith. The Mass of the Virgo Cluster. *ApJ*, 83:23, January 1936. doi: 10.1086/143697. URL `http://adsabs.harvard.edu/abs/1936ApJ....83...23S`.

The Dark Energy Survey Collaboration. The Dark Energy Survey. *ArXiv Astrophysics e-prints*, October 2005. URL `http://adsabs.harvard.edu/abs/2005astro.ph.10346T`.

A. Vikhlinin, A. V. Kravtsov, R. A. Burenin, H. Ebeling, W. R. Forman, A. Hornstrup, C. Jones, S. S. Murray, D. Nagai, H. Quintana, and A. Voevodkin. Chandra Cluster Cosmology Project III: Cosmological Parameter Constraints. *ApJ*, 692:1060–1074, February 2009. doi: 10.1088/0004-637X/692/2/1060. URL `https://ui.adsabs.harvard.edu/#abs/2009ApJ...692.1060V`.

G. M. Voit. Tracing cosmic evolution with clusters of galaxies. *Reviews of Modern Physics*, 77:207–258, April 2005. doi: 10.1103/RevModPhys.77.207. URL `http://adsabs.harvard.edu/abs/2005RvMP...77..207V`.

A. von der Linden, M. T. Allen, D. E. Applegate, P. L. Kelly, S. W. Allen, H. Ebeling, P. R. Burchat, D. L. Burke, D. Donovan, R. G. Morris, R. Blandford, T. Erben, and A. Mantz. Weighing the Giants - I. Weak-lensing masses for 51 massive galaxy clusters: project overview, data analysis methods and cluster images. *MNRAS*, 439:2–27, March 2014. doi: 10.1093/mnras/stt1945. URL `http://adsabs.harvard.edu/abs/2014MNRAS.439....2V`.

D. H. Weinberg, M. J. Mortonson, D. J. Eisenstein, C. Hirata, A. G. Riess, and E. Rozo. Observational probes of cosmic acceleration. *PhR*, 530:87–255, September 2013. doi: 10.1016/j.physrep.2013.05.001. URL `http://adsabs.harvard.edu/abs/2013PhR...530...87W`.

M. C. Weisskopf, H. D. Tananbaum, L. P. Van Speybroeck, and S. L. O'Dell. Chandra X-ray Observatory (CXO): overview. In J. E. Truemper and B. Aschenbach, editors, *X-Ray Optics, Instruments, and Missions III*, volume 4012 of *Proc. SPIE*, pages 2–16, July 2000. doi: 10.1117/12.391545. URL `http://adsabs.harvard.edu/abs/2000SPIE.4012....2W`.

H.-Y. Wu, E. Rozo, and R. H. Wechsler. Annealing a Follow-up Program: Improvement of the Dark Energy Figure of Merit for Optical Galaxy Cluster Surveys. *ApJ*, 713:1207–1218, April 2010. doi: 10.1088/0004-637X/713/2/1207. URL `http://adsabs.harvard.edu/abs/2010ApJ...713.1207W`.

Y. Zhang, C. Miller, T. McKay, P. Rooney, A. E. Evrard, A. K. Romer, R. Perfecto, J. Song, S. Desai, J. Mohr, H. Wilcox, A. Bermeo-Hernandez, T. Jeltema, D. Hollowood, D. Bacon, D. Capozzi, C. Collins, R. Das, D. Gerdes, C. Hennig, M. Hilton, B. Hoyle, S. Kay, A. Liddle, R. G. Mann, N. Mehrtens, R. C. Nichol, C. Papovich, M. Sahlén, M. Soares-Santos, J. Stott, P. T. Viana, T. Abbott, F. B. Abdalla, M. Banerji, A. H. Bauer, A. Benoit-Lévy, E. Bertin, D. Brooks, E. Buckley-Geer, D. L. Burke, A. Carnero Rosell, F. J. Castander, H. T. Diehl, P. Doel, C. E. Cunha, T. F. Eifler, A. Fausti Neto, E. Fernandez, B. Flaugher, P. Fosalba, J. Frieman, E. Gaztanaga, D. Gruen, R. A. Gruendl, K. Honscheid, D. James, K. Kuehn, N. Kuropatkin, O. Lahav, M. A. G. Maia, M. Makler, J. L. Marshall, P. Martini, R. Miquel, R. Ogando, A. A. Plazas, A. Roodman, E. S. Rykoff, M. Sako, E. Sanchez, V. Scarpine, M. Schubnell, I. Sevilla, R. C. Smith, F. Sobreira, E. Suchyta, M. E. C. Swanson, G. Tarle, J. Thaler, D. Tucker, V. Vikram, and L. N. da Costa. Galaxies in X-Ray Selected Clusters and Groups in Dark Energy Survey Data. I. Stellar Mass Growth of Bright Central Galaxies since z˜1.2. *ApJ*, 816:98, January 2016. doi: 10.3847/0004-637X/816/2/98. URL `http://adsabs.harvard.edu/abs/2016ApJ...816...98Z`.

Y. Zhang et al. Modeling The Distribution of Centering from the RedMaPPer Cluster Finding Algorithm and the Impact on Richness Estimation, in prep.

F. Zwicky. On the Masses of Nebulae and of Clusters of Nebulae. *ApJ*, 86:217, October 1937. doi: 10.1086/143864. URL https://ui.adsabs.harvard.edu/#abs/1937ApJ....86..217Z.